

Measurement of the spin structure function g_1^D of the deuteron and its moments at low Q^2

Krishna P. Adhikari, Sebastian E. Kuhn,
Alexander Deur, Lamiaa El Fassi, Hyekoo Kang, Sarah K. Phillips,
Marco Ripani, Karl Slifer, Raffaella De Vita, Gail E. Dodge,
Xiaochao Zheng

March 13, 2017

Contents

1	Introduction	4
1.1	Inclusive Electron Scattering	6
1.1.1	Kinematic Variables	7
1.1.2	Differential Cross Section and Structure Functions . . .	9
1.2	Moments of g_1 and Sum Rules	10
1.2.1	First moment Γ_1 of g_1	10
1.2.2	Generalized GDH Integral	12
1.2.3	Generalized Forward Spin Polarizability γ_0	14
2	EG4 run	16
2.1	New CC in the 6 th Sector	17
3	Data Analysis Procedure	23
3.1	Raw Data Processing - Calibration and Reconstruction	24
3.2	Helicity States	26
3.3	Electron Identification	26
3.3.1	Electromagnetic Calorimeter Cuts	28
3.3.2	Cerenkov Counter Cuts	37
3.3.3	Minimum/Maximum Momentum cuts	43
3.3.4	Vertex-Z cuts	44
3.3.5	Fiducial Cuts	46
3.4	Data Quality and Stability Checks	53
3.5	Kinematic Corrections	56
3.5.1	Incoming Energy Loss Correction	56
3.5.2	Tracking Corrections	57
3.5.3	Momentum Correction	64
3.5.4	Outgoing Ionization Loss Correction	68
3.6	Cerenkov Counter (CC) Efficiency	69

3.6.1	Procedure	71
3.7	Pion Contamination Corrections	76
3.7.1	Method	76
3.8	e^+e^- -Pair Symmetric Contamination Corrections	78
3.9	Study of NH ₃ Contamination of EG4 ND ₃ Target	80
3.9.1	Procedure	80
3.9.2	Event Selection	81
3.9.3	Extracting the Contamination	83
3.9.4	Results and Conclusion	84
4	Monte Carlo Simulations and Extraction of g_1 and $A_1 F_1$	86
4.1	Simulation and Approach to Analysis	86
4.1.1	Outline of the method	89
4.2	Radiative Corrections	91
4.3	“Standard” simulation	91
4.3.1	RCSLACPOL	92
4.3.2	Event Generator	92
4.3.3	GSIM - CLAS Detector Simulation	94
4.3.4	GSIM POST PROCESSOR (GPP)	95
4.3.5	Finding the width of the real CLAS data elastic peak. .	98
4.4	Comparison of Data and Simulation	100
4.5	Method to Extract g_1 and $A_1 F_1$	111
4.5.1	‘Variation’ of the standard simulation	111
5	Systematic Uncertainties	116
5.1	Evaluation of Experimental Systematics	117
5.2	Model uncertainties	119
5.3	Combining uncertainties	121
5.3.1	Combining uncertainties from the two beam energies .	121
5.3.2	Combining uncertainties from the ten sources	122
5.3.3	Combining data from the two beam energies	122
6	Results	134
6.1	Extracted g_1 and $A_1 F_1$	134
6.2	Moments of Deuteron Spin Structure functions	143
6.2.1	First moment of g_1 (Γ_1)	145
6.2.2	The extended GDH integral \bar{I}_{TT}	147
6.2.3	The Generalized Forward Spin Polarizability γ_0	149

7 Conclusions	152
A FFREAD cards used by GSIM	161

¹ Chapter 1

² Introduction

³
⁴ A large amount of data on the spin dependent structure of the nucleon has
⁵ been accumulated since the late 1970s from both fixed target and colliding
⁶ beam experiments with polarized photons, (anti)electrons, and muons as well
⁷ as protons on a variety of polarized targets from hydrogen through 3He .

⁸ In a simple non-relativistic model one would expect the quarks to carry
⁹ the entire spin of the nucleon, but one of the first experiments carried out
¹⁰ at SLAC, in a limited kinematic region, seemed to confirm the predictions
¹¹ of the Naive Parton Model (NPM) - one of the early more realistic theo-
¹² ries - which predicted that 60% of the nucleon spin is carried by the quarks
¹³ [1]. However, a subsequent, more precise measurement over a larger kinematic
¹⁴ region performed by the EMC experiment at CERN reported, contrary to
¹⁵ the NPM predictions, that only $12 \pm 17\%$ of the spin is carried by the quarks
¹⁶ [2]. This discovery of the so-called “spin crisis” sparked a large interest in
¹⁷ measuring the spin content of the nucleon, giving birth to several experiments
¹⁸ (completed, underway and proposed) around the globe. The theoretical de-
¹⁹ velopments of Quantum Chromodynamics (QCD) - the quantum field theory
²⁰ that describes the nuclear interaction between the quarks and gluons - have
²¹ clarified our picture of the nucleon spin structure in great details. With the
²² discovery of a unique QCD property known as “asymptotic freedom”, quarks
²³ are known to be essentially free at high energies (typically several GeV) al-
²⁴ lowing perturbative QCD (PQCD) calculations of testable predictions for
²⁵ processes involving high energy or high momentum transfers [3]. Verifying
²⁶ Bjorken sum rule [4], which relates results from inclusive, polarized deep in-
²⁷ elastic scattering (DIS) to the axial coupling constant g_A of neutron beta

28 decay, is a precise test of QCD in its spin sector. The DIS results have ver-
29 ified the Bjorken sum rule at the level of 10% accuracy and has shown that
30 only about $30 \pm 10\%$ of the nucleon spin is carried by the quarks; the rest
31 of the spin must reside either in gluons or orbital angular momentum of its
32 constituents. Experiments to measure the gluon contribution are underway
33 at Brookhaven National Laboratory (BNL) and CERN.

34 Probing nucleon structure on the other end of the energy scale (i.e. prob-
35 ing with low momentum transfers) provides information about long distance
36 structure, which is also associated with static properties of the nucleon. In
37 this low energy regime, however, QCD calculations with the established per-
38 turbative methods become difficult or even impossible because the strong
39 coupling (α_s) becomes large. Thus perturbative expansions do not converge.
40 In this energy regime, the partons become very strongly coupled to the point
41 of being confined into hadrons which now emerge as the effective degrees of
42 freedom for the interaction. Therefore, other methods must be relied on to
43 make predictions in these non-perturbative energy scales. For example, effec-
44 tive theories such as chiral perturbation theory (χ PT) are used. There is also
45 an intermediate region where neither of these approaches (PQCD or χ PT)
46 is expected to work. In this region, it is expected that lattice QCD methods
47 will provide testable predictions in the near future. There are also some phe-
48 nomenological models aimed at describing the entire kinematic range. The
49 description of the low energy regime in terms of these theories and models
50 is challenging and theories used here still face difficulties (see below). There
51 are several predictions (for both nucleons as well as some light nuclei such as
52 the deuteron and Helium-3) from these low energy theories and models on
53 various observables which can be tested experimentally. Therefore, having
54 high precision data at the lowest possible momentum transfer is necessary to
55 test these predictions. In addition, new results will also help constrain future
56 calculations and provide input for detailed corrections to higher energy data.

57 With that perspective and motivation, the “EG4” experiment (E06-017)
58 for a precision double polarization measurement at low momentum transfer
59 using both proton and deuteron targets and the Hall B CLAS detector was
60 performed at Jefferson Lab. In addition to the usefulness of the measured
61 deuteron data for testing theoretical predictions calculated for the deuteron
62 itself, the data are also necessary for extracting neutron data in combination
63 with similar data from the proton target. An experiment with the similar
64 goal of probing the neutron at low momentum transfers but using ^3He was
65 performed in Hall A [5]. However, to be able to control nuclear medium

66 effects, neutron information must be extracted from both 3He and 2D . The
67 data on the deuteron (and eventually on the neutron) will not only be useful
68 to test the theoretical predictions at low but non-zero momentum transfers
69 but they can also be extrapolated to the real photon limit, thus testing some
70 long standing predictions such as the Gerasimov-Drell-Hearn (GDH) sum
71 rule [6, 7] derived from general principles. The analysis of the deuteron data
72 is the subject of this note.

73 In the future, we will extract information from the deuteron and proton
74 data from the EG4 experiment to provide a self-consistent determination of
75 the Bjorken sum, helping us to understand the transition from the partonic to
76 hadronic descriptions of the strong interaction. The data will also be useful in
77 studying the validity of quark-hadron duality in the spin sector, thus helping
78 further to understand the transition from the partonic to hadronic pictures.

79 **1.1 Inclusive Electron Scattering**

80 High energy particle scattering processes provide very powerful microscopes
81 to examine objects such as nuclei and nucleons. Scattering of leptons (most
82 commonly electrons) is one of the most extensively used processes. For ex-
83 ample, the scattering of high energy leptons off nucleons has played a key role
84 in determining the partonic structure of the nucleons. Following are some of
85 the advantages of lepton (and in particular electron) scattering:

- 86 • Leptons interact through the electroweak interaction which is very well
87 understood.
- 88 • The interaction is relatively weak, thus allowing the use of perturbative
89 QED.
- 90 • In electron scattering, one can, moreover, control and vary the po-
91 larization of the virtual photon (exchanged during the interaction) by
92 changing the electron kinematics. This allows the separation of the
93 charge and current interaction. Data from the scattering of polarized
94 electrons by polarized targets allows one to examine the target's strong-
95 interaction spin structure.
- 96 • A great advantage of electrons is that they can be copiously produced
97 in the laboratory relatively easily and at low costs, and since they are

98 charged, they can readily be accelerated and detected. (It is not as
99 easy and cheap to produce and handle the other lepton types.

100 In this section, we discuss the process of inclusive electron scattering (in
101 which only the scattered electron is detected ignoring the rest of the com-
102 ponents of the final state after the interaction). In doing so, the relevant
103 kinematic variables and related physical quantities to be measured or calcu-
104 lated from the process will be introduced and some of their relations with
105 one another will be deduced and discussed.

106 1.1.1 Kinematic Variables

107 A lepton scattering process, in which an incoming lepton represented by $l(p)$
108 of four momentum $p = p^\mu = (E, \vec{k})$ scatters off a target $N(P)$ which is usually
109 a nucleon or a nucleus at rest and with four momentum $P = P^\mu = (M, \vec{0})$,
110 can simply be represented by

$$l(p) + N(P) \rightarrow l(p') + X(P') \quad (1.1)$$

111 where $l(p')$ and $X(P')$ represent the scattered lepton and the rest of the
112 final state (which can have any number of particles) with four momenta
113 $p'^\mu = (E', \vec{k}')$ and $P'^\mu = (E_X, \vec{k}_X)$ respectively. The scattering angle which is
114 the angle between the incident and outgoing path/direction of the electron
115 is denoted by θ . The final (hadronic) state denoted by x is not measured,
116 with only the scattered electron detected and measured by the detector(s).
117 In the first order (Born) approximation of the process, a virtual photon is
118 exchanged (as depicted in Fig (1.1)) whose four momentum is equal to the
119 difference between that of the incident and the scattered electron and is given
120 by $(p - p')^\mu = (\nu, \vec{q})$, where $\nu = (P \cdot q)/M$ and \vec{q} represent the energy and
121 3-momentum transferred by the incident electron to the target $N(P)$.

122 The kinematics of the scattering process, for a given beam energy E , can
123 be completely described in terms of two of the following Lorentz invariant

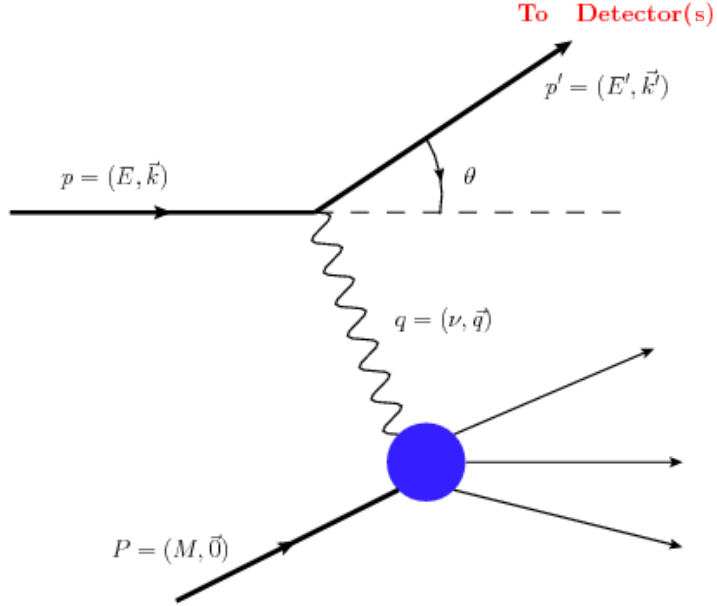


Figure 1.1: Lowest order (Born approximation) Feynmann diagram representing the process of inclusive lepton scattering

¹²⁴ variables.

$$\nu = E - E' \quad (1.2)$$

$$Q^2 = -q^2 \simeq 4EE' \sin^2 \frac{\theta}{2} \quad (1.3)$$

$$W = \sqrt{(P+q)^2} = \sqrt{M^2 + 2M\nu - Q^2} \quad (1.4)$$

$$x = \frac{Q^2}{2P \cdot q} = \frac{Q^2}{2M\nu} \quad (1.5)$$

$$y = \frac{q \cdot P}{p \cdot P} = \frac{\nu}{E} \quad (1.6)$$

¹²⁵ where $Q^2 = -q^2$ is the negative of the squared four-momentum transferred
¹²⁶ (with electron mass neglected in the expression for Q^2), which defines the
¹²⁷ resolution of the electron probe; W is the invariant mass of the unmeasured
¹²⁸ final state (x); x is known as the Bjorken scaling variable, which is also
¹²⁹ interpreted as the momentum fraction carried by the struck quark (parton)
¹³⁰ in the infinite momentum frame; M is the nucleon mass ≈ 0.939 GeV, and
¹³¹ lastly, y is the fraction of the energy that is lost by the lepton during the

¹³² process.

¹³³ ¹³⁴ 1.1.2 Differential Cross Section and Structure Functions

¹³⁵ The differential cross section for the process of inclusive (polarized) elec-
¹³⁶ tron scattering on (polarized) targets can be expressed, in the Born ap-
¹³⁷ proximation, in terms of four dimensionless structure functions $F_1(x, Q^2)$,
¹³⁸ $F_2(x, Q^2)$, $g_1(x, Q^2)$, and $g_2(x, Q^2)$, effectively parameterizing the internal
¹³⁹ hadronic structure information into four response functions. For example,
¹⁴⁰ in the case of the anti-parallel or parallel beam and target polarizations,
¹⁴¹ the spin-dependent (polarized) inclusive cross sections can be expressed as
¹⁴² follows:

$$\frac{d^2\sigma}{d\Omega dE'} = \left(\frac{d\sigma}{d\Omega} \right)_{Point} \left[\frac{2}{M} F_1(x, Q^2) \tan^2 \frac{\theta}{2} + \frac{1}{\nu} F_2(x, Q^2) \pm 2 \tan^2 \frac{\theta}{2} \left[(E + E' \cos \theta) \frac{M^2}{\nu} g_1(Q^2, \nu) - \gamma^2 M^2 g_2(Q^2, \nu) \right] \right]^{(1.7)}$$

¹⁴³ where “+” refers to anti-parallel beam helicity and target polarization,
¹⁴⁴ while “-” refers to the parallel case. And the Point cross section (for the
¹⁴⁵ lepton scattering from a Dirac particle - a spin-1/2 point particle of charge
¹⁴⁶ +e) given by

$$\left(\frac{d\sigma}{d\Omega} \right)_{Point} = \frac{\alpha^2 \cos^2 \frac{\theta}{2}}{4E^2 \sin^4 \frac{\theta}{2}} \frac{E'}{E} \quad (1.8)$$

¹⁴⁷ with $\frac{E'}{E}$ being the recoil factor.

¹⁴⁸ These kind of relationships allow the measurement of structure functions
¹⁴⁹ by measuring cross-sections corresponding to different combinations of beam
¹⁵⁰ and target polarizations. For example, one can extract the first two structure
¹⁵¹ functions F_1 and F_2 from the unpolarized scattering experiments, whereas,
¹⁵² the spin structure functions g_1 and g_2 can be measured in experiments with
¹⁵³ polarized electron beam and polarized targets and by measuring the cross
¹⁵⁴ section difference between the anti-parallel and parallel beam-target polar-
¹⁵⁵ izations.

¹⁵⁶ **1.2 Moments of g_1 and Sum Rules**

¹⁵⁷ Moments of structure functions are their integrals (over the complete x range)
¹⁵⁸ weighted by various powers of the variable x. The n^{th} moment of g_1 , for
¹⁵⁹ example, is given by

$$\Gamma_n(Q^2) = \int_0^1 g_1(x, Q^2) x^{(n-1)} dx \quad (1.9)$$

¹⁶⁰ The moments allow the studies of the (Q^2 dependence of) fundamental
¹⁶¹ properties of nucleon structure. For example, the first moment of xF_1 of a
¹⁶² nucleon gives the total momentum or mass fraction carried by quarks and the
¹⁶³ first moment of g_1 gives the fraction of the nucleon spin contributed by the
¹⁶⁴ quark helicities. These integrals get their particular significance from the fact
¹⁶⁵ that they can be predicted from rigorous theoretical methods, such as in the
¹⁶⁶ sum rules derived from general assumptions or from the method of Operator
¹⁶⁷ Product Expansion, lattice QCD calculations and χ PT calculations¹. Their
¹⁶⁸ importance can be highlighted from the fact that it was the experimental
¹⁶⁹ tests of the sum rules involving the first moments of nucleon that led to the
¹⁷⁰ discovery of the original “spin crisis” and provided a significant test of QCD
¹⁷¹ in the spin sector [8].

¹⁷² In this section, three integrals are considered which have been calculated
¹⁷³ from the EG4 data on the deuteron - the first moment of g_1 (Γ_1), the gen-
¹⁷⁴ eralized GDH integral (\bar{I}_{TT}), and the generalized forward spin polarizability
¹⁷⁵ (γ_0).

¹⁷⁶ **1.2.1 First moment Γ_1 of g_1**

¹⁷⁷ The first moment of g_1 is the integral of g_1 over the complete range of the
¹⁷⁸ Bjorken scaling variable x.

$$\Gamma_1(Q^2) = \int_0^1 g_1(x, Q^2) dx \quad (1.10)$$

¹In contrast, the same is not true about the structure functions because presently their complete description based on QCD first principles has not been possible yet (especially in the low to intermediate momentum transfer regions due to the strong coupling property of QCD).

179 This moment gives, in the quark-parton model, the fraction of the nu-
180 cleon spin contributed by the quark helicities and enters directly into two
181 historically important sum rules - Ellis-Jaffe sum rule and Bjorken sum rule.
182 Measurements of the moment on the proton by the European Muon Collabo-
183 ration (EMC) in 1988 showed that the Ellis-Jaffe sum rule is violated, which
184 meant that the long held belief that all the proton spin is carried by quarks
185 is not true, thus, sparking the well known “spin crisis”. On the other hand,
186 measurements from SLAC, CERN, Fermilab, DESY, and more recently, from
187 JLab, have confirmed the Bjorken sum rule (which relates the difference of
188 the first moments of the proton and the neutron to the fundamental axial
189 coupling constant (g_A) of neutron beta decay) at the level of 10% accuracy,
190 thus helping establish the QCD as the correct theory of the strong interac-
191 tions. The moment also enters into the virtual photon extension of another
192 famous sum rule - the GDH sum rule (see below).

193 In addition, the moment is studied on its own right because it provides
194 a powerful tool to test the validity of various theories and models in which
195 it is calculable. In the past, it has been measured on proton, deuteron and
196 neutron (${}^3\text{He}$) at SLAC, CERN and DESY in the DIS region in order to
197 understand the quark spin contribution as well as to test the validity of
198 the Bjorken sum rule and hence QCD as a result [8]. Recently, it has also
199 been measured at JLab from DIS down to a fairly low Q^2 region. In the
200 intermediate and low momentum transfers, some phenomenological model
201 predictions are available, whereas in the very low Q^2 region, several chiral
202 perturbation theory (χPT) calculations are available.

203 **1.2.2 Generalized GDH Integral**

204 **GDH Sum Rule**

205 The Gerasimov-Drell-Hearn (GDH) sum rule [6, 7] relates the energy weighted
206 sum of a particle's photo-absorption cross sections to its anomalous magnetic
207 moment κ . For a target of arbitrary spin S , the sum rule is:

$$\int_{\nu_{th}}^{\infty} \frac{\sigma_P(\nu) - \sigma_A(\nu)}{\nu} = -4\pi^2 \alpha S \left(\frac{\kappa}{M}\right)^2 \quad (1.11)$$

208 where σ_P and σ_A are the photoabsorption cross sections with photon helicity
209 parallel and anti-parallel to the target spin respectively. M and κ represent
210 the target mass and anomalous magnetic moment respectively and S rep-
211 resents the target spin. The integration extends from the onset ν_{th} of the
212 inelastic region ² through the entire kinematic range and is weighted by the
213 inverse of the photon energy ν .

214 The sum rule for the proton has been measured (at various places such as
215 Mainz, Bonn, BNL and others) and verified to within 10% [9–12] and some
216 deuteron results exist from Mainz and Bonn, but there is very little or no
217 data available on neutron and other targets;

218 **Implications of the sum rule** The sum rule relates the static property
219 κ of a particle's ground state with the sum of the dynamic properties of
220 all the excited states. One deeper significance of this sum rule is that if a
221 particle has a non-zero anomalous magnetic moment, then it must have some
222 internal structure, and, therefore, a finite size, in order to have the excited
223 states (a point-like particle cannot have excited states). Because of the same
224 reason, the discovery of nucleon anomalous magnetic moments provided one
225 of the first strong indications that the nucleons had some intrinsic internal
226 structure.

227 In addition to the benefit of that implication, the sum rule and its exten-
228 sion to $Q^2 > 0$ provides an important testing ground for various theoretical
229 predictions based on QCD and its effective theories/models.

²The pion photo-production threshold given by $\nu_{th} = m_\pi(1 + m_\pi/2M) \approx 150\text{MeV}$ marks the onset of the inelastic region for the nucleons, but for nuclei, the summation starts from the first nuclear excitation level

230 **Generalization of the GDH Sum (Rule)**

231 In order to investigate the “spin crisis” of the 1980’s, Anselmino *et al.* [13]
 232 proposed that the real photon ($Q^2=0$) GDH integral could be extended to
 233 electroproduction cross sections (finite Q^2) and that the experimental deter-
 234 mination of the extended integral would shed light on the transition from
 235 the perturbative to non-perturbative QCD. The idea was to use the virtual
 236 photoabsorption cross sections in place of the real photoabsorption cross sec-
 237 tions and proceed in exactly the same way as when deriving the real photon
 238 GDH sum rule. This extension depends somewhat on the choice of the vir-
 239 tual photon flux and on how the spin structure function g_2 is considered [14].
 240 In one extension the virtual photon flux given by $K = \nu$ is chosen and the
 241 real photoabsorption cross section difference in Eq. 1.11 are replaced by
 242 the corresponding virtual photoabsorption cross section difference $2\sigma_{TT}$. As
 243 a result, we get the following extended GDH integral (considering only the
 244 inelastic contribution starting from the pion production threshold) [8]

$$\bar{I}_{TT} = \frac{2M^2}{Q^2} \int_0^{x_0(Q^2)} dx [g_1(x, Q^2) - \frac{4M^2 x^2}{Q^2} g_2(x, Q^2)] \quad (1.12)$$

245 where $x_0(Q^2) = Q^2/(Q^2 + m_\pi(2M + m_\pi))$ is the pion production threshold
 246 that defines the onset of the inelastic region.

247 The integral can also be expressed in terms of the first moment of the
 248 product $A_1 F_1$ as follows:

$$\bar{I}_{TT} = \frac{2M^2}{Q^2} \int_0^{x_0(Q^2)} dx A_1(x, Q^2) F_1(x, Q^2) \quad (1.13)$$

249 where A_1 is the virtual photon asymmetry as given by:

$$A_1(x, Q^2) = \frac{\sigma_{\frac{1}{2}}^T - \sigma_{\frac{3}{2}}^T}{\sigma_{\frac{1}{2}}^T + \sigma_{\frac{3}{2}}^T} = \frac{g_1(x, Q^2) - \gamma^2 g_2(x, Q^2)}{F_1(x, Q^2)} \quad (1.14)$$

$$(1.15)$$

250 **1.2.3 Generalized Forward Spin Polarizability γ_0**

251 Polarizabilities are fundamental observables (quantities) that characterize the
 252 structure of composite objects such as nucleons or deuteron. They reflect the
 253 response to external perturbations such as external electromagnetic fields.
 254 Like the GDH sum, they are also integrals over the excitation spectrum of
 255 the target and their derivations rely on the same basic assumptions. At
 256 the real photon point, for example, the electric and magnetic polarizabilities
 257 α and β represent the target's response to external electric and magnetic
 258 fields respectively. The generalized polarizabilities represent the extensions
 259 of these quantities to the case of virtual photon Compton scattering. Because
 260 the integrals defining the polarizabilities involve weighting by some powers
 261 of $1/\nu$ or x , they converge faster than the first moments and thus are more
 262 easily determined from low energy measurements. In other words, they have
 263 reduced dependence on the extrapolations to the unmeasured regions at large
 264 ν , and higher sensitivity to the low energy behavior of the cross sections
 265 (particularly the threshold behavior), thus providing better testing grounds
 266 for theoretical predictions such as from χ PT and phenomenological models
 267 [14].

268 The GDH sum rule comes from the first term of the low energy expansion
 269 of the forward Compton amplitude [15]. Likewise, we get another sum rule
 270 from the second, i.e., the next-to-leading term (which is in the third power
 271 of ν). The second coefficient of the expansion is known as the forward spin
 272 polarizability γ_0 and by comparing the coefficients of the ν^2 terms on both
 273 sides (coming from the dispersion relations on the left side and from the low
 274 energy expansion on the right side) gives us the following expression for the
 275 polarizability [16]:

$$\gamma_0 = -\frac{1}{4\pi^2} \int_{thr}^{\infty} \frac{\sigma_{\frac{1}{2}} - \sigma_{\frac{3}{2}}}{\nu^3} d\nu \quad (1.16)$$

276 Now, by considering the case of forward scattering of a virtual photon and
 277 using the same general approach as for getting the generalized GDH sum rule,
 278 the $\mathcal{O}(\nu^3)$ (NLO) term in the low energy expansion of VVCS (doubly virtual
 279 Compton scattering) amplitude $g_{TT}(x, Q^2)$ gives the following generalization
 280 of the forward spin polarizability [17] [8]:

$$\begin{aligned}\gamma_0(Q^2) \equiv \gamma_{TT}(Q^2) &= \frac{16\alpha M^2}{Q^6} \int_0^{x_0} \left[g_1(x, Q^2) - \frac{4M^2 x^2}{Q^2} g_2(x, Q^2) \right] x^2 dx \\ &= \frac{16\alpha M^2}{Q^6} \int_0^{x_0} A_1(x, Q^2) F_1(x, Q^2) x^2 dx\end{aligned}\quad (1.18)$$

281 where $\alpha = \frac{e^2}{4\pi}$ is the fine structure constant. At large Q^2 , the g_2 dependent
 282 term in the integrand becomes negligible and γ_0 reduces to the third moment
 283 of g_1 [17].

284 In exactly the same manner, from the $\mathcal{O}(\nu^2)$ term of the low energy
 285 expansion of the VVCS amplitude $g_{LT}(x, Q^2)$ one gets another polarizability
 286 - the generalized longitudinal-transverse polarizability as follows:

$$\delta_0(Q^2) \equiv \delta_{LT}(Q^2) = \frac{16\alpha M^2}{Q^6} \int_0^{x_0} [g_1(x, Q^2) + g_2(x, Q^2)] x^2 dx \quad (1.19)$$

287 This latter polarizability is not considered here because we did not measure
 288 the transverse target configuration.

289 Because the generalized polarizabilities can be expressed with the mo-
 290 ments of the structure functions, it is possible to measure them using mea-
 291 surements of the structure functions. As stated earlier, because of the weight-
 292 ing by some powers of ν or x , these integrals converges more rapidly in energy
 293 than the GDH integral and therefore can more easily be determined by low
 294 beam energy measurements. These integrals are valuable because they shed
 295 light on the long distance (soft), non-perturbative aspects of the target struc-
 296 ture. The integrals are possible to be calculated using effective or approxi-
 297 mate theories such as χ PT and lattice methods. Thus the measurements of
 298 these quantities provide benchmark tests of such theories.

299 The first measurement of γ_0 for a proton target at the real photon point
 300 was done by the GDH experiment at Mainz [16]. Recently the JLab EG1b
 301 experiment has provided some finite Q^2 results for both deuteron as well as
 302 nucleon targets [18].

³⁰³ **Chapter 2**

³⁰⁴ **EG4 run**

³⁰⁵ The deuteron target part of the EG4 experiment ran for about a month
³⁰⁶ in 2006, mostly with longitudinally polarized frozen $^{15}\text{ND}_3$ as the target. In
³⁰⁷ between these deuteron runs, some small amount of data was also collected on
³⁰⁸ carbon-12 and empty cell targets, which are important in various auxiliary
³⁰⁹ studies during the data analysis (such as their use in estimating nuclear
³¹⁰ background while developing momentum corrections, estimating the length
³¹¹ of the target material or estimating unpolarized background). A total of 113
³¹² data runs (from run ID 51896 to 52040) were collected for the lower beam
³¹³ energy (1.3 GeV) and 221 runs (from 51593 to 51867) for the 2.0 GeV case
³¹⁴ (with each run consisting of about 3.0×10^7 event triggers) [19]. Each run
³¹⁵ took about 2 hours and collected about 2 GB of data in raw format and
³¹⁶ saved as about 20-30 BOS files (see next section). With the combination of
³¹⁷ low beam energies and low scattering angles, low momentum transfers can
³¹⁸ be measured down to about 0.02 GeV² within the kinematic coverage of the
³¹⁹ resonance region ($1.08 < W < 2.0$ GeV.)

³²⁰ In addition to the use of low beam energies and low θ measurements, in
³²¹ order to maximize the statistics in the low momentum transfers, following
³²² measures were taken that were unique to the experiment:

- ³²³ • Use of the electron outbending torus field configuration to enhance the
³²⁴ low angle acceptance (so that more of very forward going electrons
³²⁵ would be bent towards and detected by the CLAS detector).
- ³²⁶ • Use of a a newly built Cerenkov Counter (CC) in the 6th sector¹ (see
³²⁷ Figs. 2.3 and 2.4) that was designed to optimize electron detection

¹For reasons of limited resources, only one new CC was built and the 6th sector alone

328 in the outbending torus configuration. This led to a better and more
329 uniform detection efficiency would be better and more uniform than
330 with the existing counters² which were optimized for electron inbending
331 configuration.

- 332 • To further enhance the low angle coverage, the polarized target was
333 placed in a more retracted position along the beam line i.e. at about
334 -101.0 cm upstream of the CLAS center.

335 Other than that the CLAS detector was used in the standard configura-
336 tion like in any other polarized target experiments using CLAS.

337 **2.1 New CC in the 6th Sector**

338 The Cherenkov Counters (CC) serve the dual function of triggering on elec-
339 trons and separating electrons from pions (or identifying charged particles).
340 These detectors use the light emitted by Cherenkov radiation (emission of
341 light when the charged particle travels faster than light in that medium) to
342 measure the particle velocity (or rather $\beta = v/c$). The knowledge of β com-
343 bined with the particle momentum (from the tracking detectors) determines
344 the particle's mass, thus giving us information on the particle identification.
345 The index of refraction (n) is carefully optimized for the particle masses and
346 momentum range of the experiments in question. Threshold counters record
347 all light produced, thus providing a signal whenever β is above the threshold
348 $\beta_t = 1/n$. In the standard configuration, CLAS uses one Cherenkov threshold
349 detector in each of the six sectors in the forward region from 8° to 45°.

350 A new gas threshold cherenkov counter (designed and built by INFN -
351 Genova, Italy) was installed in the sixth sector. This new CC detector (see
352 Fig. 2.3 for its CAD rendition) is specifically optimized for the out-bending
353 field configuration, which is necessary to reach the desired low momentum
354 transfer (measurements down to 6 degrees). The detector uses the same ra-
355 diator gas (C_4F_{10} - perfluorobutane) and the same gas flow control system as

was used to detect the scattered electrons

²The standard CLAS Cherenkov detectors were designed such that their optics, geometry, module position and mirror orientation were optimized for low rate high Q^2 experiments that mostly use(d) electron in-bending torus fields. The design was a compromise between the desired kinematic coverage and the complexities of the CLAS detector system including the effect of the torus field.

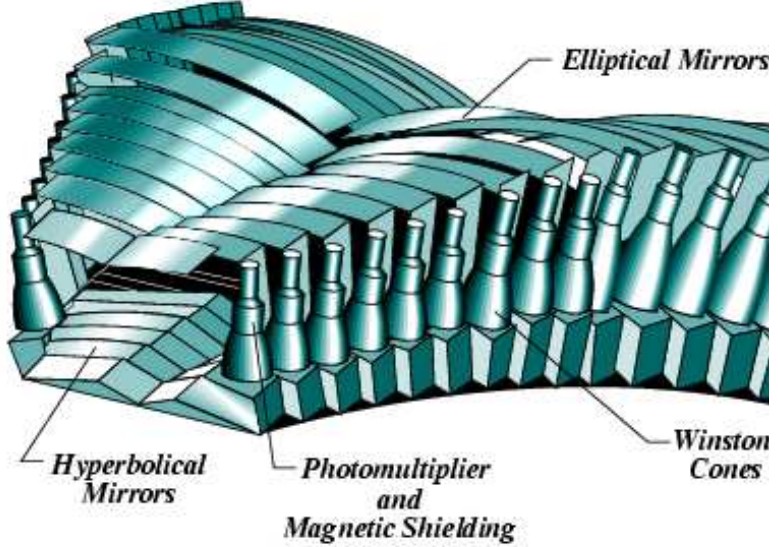


Figure 2.1: The computer rendered image of the Standard CLAS Cherenkov Counter

356 the standard one, but it uses a different design. In the new CC, the number
 357 of CC-modules is now 11 instead of the 18 in the standard ones. In order
 358 to maximize the light collection, a single reflection design (see Fig. 2.4(b))
 359 using spherical mirrors is used (the standard CC used double relections from
 360 elliptical and hyperbolic mirrors). The geometry, the size, the mirror size,
 361 position, and orientation, the dimensions as well as the assembly of the mod-

ules were optimized for the experiment and the performance study was done using a complete GEANT simulation [16]. Additionally, for the purpose of efficiency and performance studies (see Sec. 3.6), a few special trigger data runs were taken during the experiment. These special runs had the trigger that mainly involved EC-signals (and no CC-signal at all) to decide whether the detected particle was a good scattered electron candidate.

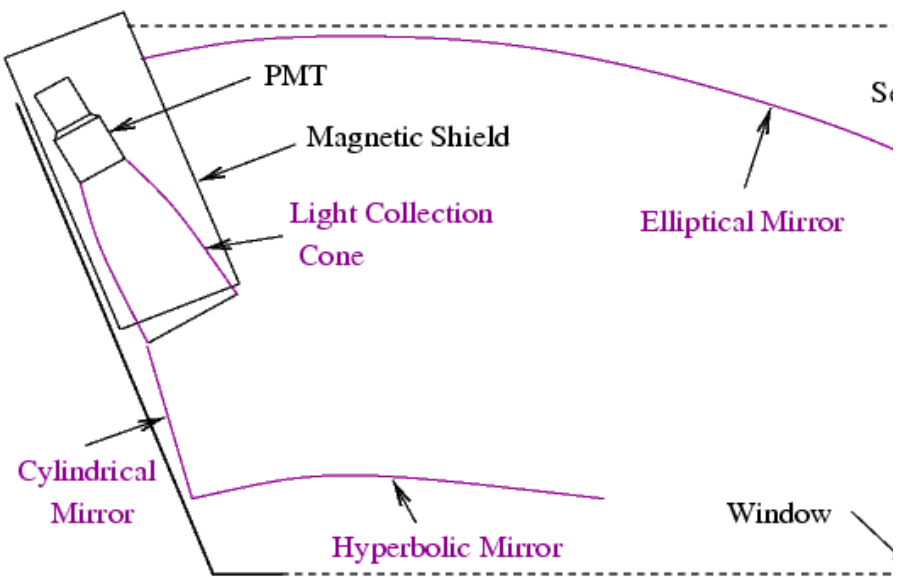


Figure 2.2: The schematic diagram of a CLAS Cherenkov Counter (CC) module showing mirrors, PMTs and the light reflections.

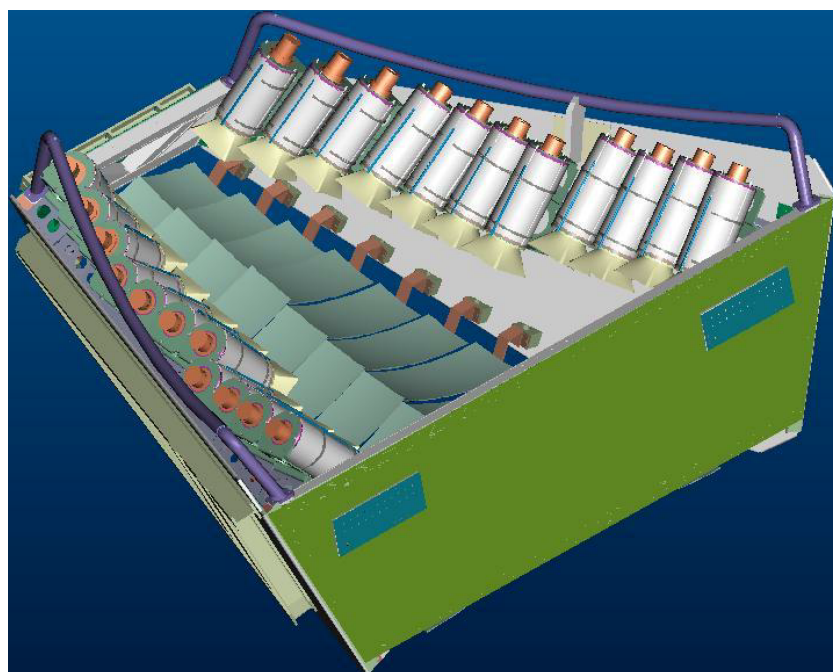


Figure 2.3: The new Cherenkov counter (courtesy of INFN, Genova)

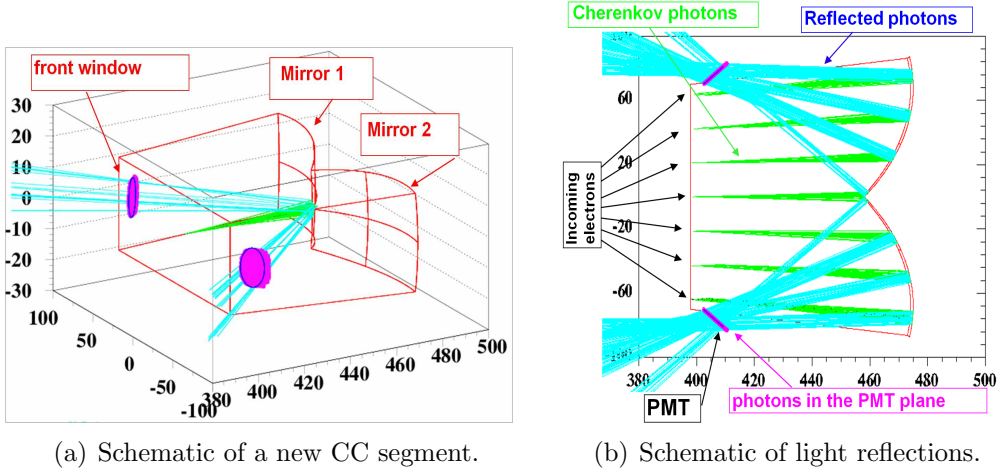


Figure 2.4: Schematic of a new CC segment showing the arrangements of the mirrors, PMTs and the light reflections (courtesy of INFN, Genova).

³⁶⁸ **Chapter 3**

³⁶⁹ **Data Analysis Procedure**

³⁷⁰ The goal of this data analysis is to extract the spin structure function g_1 for
³⁷¹ the deuteron and evaluate its moments. Since the product $A_1 F_1$, which is
³⁷² proportional to σ_{TT} , directly enters sum rules for the real photon point, which
³⁷³ leads to the generalized GDH integral (\bar{I}_{TT}) and the generalized forward spin
³⁷⁴ polarizability (γ_0) being expressed in terms of the first and third moments of
³⁷⁵ the product $A_1 F_1$, we decided also to extract the product $A_1 F_1$ using exactly
³⁷⁶ the same procedure as for g_1 .

³⁷⁷ The extraction of both g_1 and $A_1 F_1$ depend directly on the measurement
³⁷⁸ of the following polarized cross-section difference:

$$\Delta\sigma_{\parallel} = \frac{d^2\sigma^{\downarrow\uparrow}}{d\Omega dE'} - \frac{d^2\sigma^{\uparrow\uparrow}}{d\Omega dE'} = \frac{1}{N_t} \cdot \left[\frac{N^+}{N_{e^-}^+} - \frac{N^-}{N_{e^-}^-} \right] \cdot \frac{1}{P_b P_t} \cdot \frac{1}{\Delta\Omega} \cdot \frac{1}{\eta_{detector}} \quad (3.1)$$

³⁷⁹ where,

- ³⁸⁰ • N_t = Number density of deuteron nuclei in the target
- ³⁸¹ • $N^{+/-}$: Number of scattered electrons (off deuteron only) for each helicity state (+/-).
- ³⁸³ • $N_{e^-}^{+/-}$: Number of incident electrons for +/- helicity states
- ³⁸⁴ • $P_b P_t$ = Product of the beam and target polarizations
- ³⁸⁵ • $\Delta\Omega = \sin\theta \cdot \Delta\theta \cdot \Delta\phi$: The solid angle for the given kinematic bin. This term includes the “detector acceptance”.

387 • $\eta_{detector}$ accounts for the detector efficiencies

388 The data analysis to extract the physics quantities involves accurately
389 measuring each of these quantities, either separately or in some combined
390 form. To do so, the data must be properly reconstructed, calibrated and
391 corrected to build all the scattering events during the experiment. Since
392 the reconstructed events include a wide range of physical processes in ad-
393 dition to the electron-deuteron scattering process that we are interested in,
394 proper event selection cuts must be applied. In this chapter, all these steps
395 from the data reconstruction and calibration through the extraction of g_1 are
396 described.

397

398 **3.1 Raw Data Processing - Calibration and** 399 **Reconstruction**

400 The raw data recorded by the CLAS DAQ system, which consists of ADC
401 and TDC values registered by various detector components as well as the
402 beam related information such as beam helicity and Faraday Cup readings,
403 are organized into banks (with each bank carrying data belonging to a par-
404 ticular detector component or some part of it) and saved in special format
405 (BOS) files. These raw data are next processed with a standard CLAS soft-
406 ware package called RECSIS, which analyzes and combines the matching bits
407 and pieces of the raw information to reconstruct particles and events that
408 produced them. Such reconstruction produces output data that consist of
409 event and particle IDs, particle positions and energies and momenta (in the
410 lab frame CLAS coordinate system), and also some static particle properties
411 such as charge and mass. The reconstruction program uses geometric pa-
412 rameters and calibration constants (from the CLAS Calibration Database)
413 for the detector in order to properly process and transform the raw data into
414 the reconstructed tracks.

415 The first part of the data processing is the detector calibration. In this
416 phase, a small sample (about 10%) of raw data (uniformly selected over the
417 entire run period to ensure time stability verification) is chosen and the en-
418 ergy and time calibration constants are adjusted to give the correct behavior
419 while constantly monitoring related variables. This is done separately for
420 each run period to consider the different running conditions, the possibility

421 of unwanted changes in hardware that may have occurred, as well as drift
422 of detector response over time. This process of adjusting the calibration
423 constants and reconstructing the data is repeated until a desired level of ac-
424 curacy is reached. Once that level is reached, the calibration constants are
425 “frozen” and the final reconstruction is done. The resulting output is saved
426 in especial formats¹. These saved data provided the starting point for our
427 higher level data analysis as described in this dissertation.

428 The iterative work of data reconstruction and detector calibration, which
429 was a very computing intensive and time consuming, was done by R. De
430 Vita - one of the EG4 collaborators from INFN, Genova, with good expertise
431 on CLAS data reconstruction - soon after the data collection was completed
432 (from 2006-2007). The data from this “Pass1” reconstruction was first an-
433 alyzed as part of the Ph. D. dissertations by three graduate students, but
434 during these analyses, a few anomalies² in reconstruction were observed which
435 were later tracked down to a mixing up of codes from two EG4 sub-packages
436 for the reconstruction software. After the mix-up was sorted out, a new pass
437 (Pass2) of reconstruction was performed by L. El Fassi (still using the same
438 calibration constants as used by the Pass1 reconstruction). The data from
439 this latest pass of reconstruction was used for the analysis reported in this
440 note

¹Two especial data formats - BOS and ntuple (h10) - were used

²The anomalies observed in the pass1 analysis were the discretized reconstruction of vertex and wrong reconstruction of track positions in DC1.

441 **3.2 Helicity States**

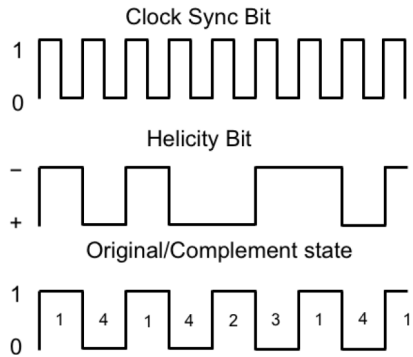


Figure 3.1: Different data signals sent from the injector that monitor the helicity states of beam electrons. (Fig. courtesy of N. Guler [20]).

442 As we saw from Eq. 3.1, the physics extraction depends on measurements of
443 the number of events in the two (+/-) electron helicity states. The CEBAF
444 accelerator provides the polarized electrons in closely and equally spaced
445 bunches. These bunches are further grouped into “buckets” according to
446 their helicity states, which are alternated pseudo-randomly at the injector
447 with a frequency of 30 Hz. The information on the helicity state of each of
448 the buckets and the total integrated charge contained in it is injected into the
449 DAQ data stream immediately after the helicity flip. Using a combination of
450 different types of sequence control signals sent from the injector (see Fig. 3.1),
451 it is possible to determine which helicity state a particular event belonged
452 to, which then can be used to label the helicity state of the event in the data
453 stream, together with the total beam charge of the state.

454 **3.3 Electron Identification**

455 In CLAS electron-scattering experiments, the scattered electron defines the
456 timing of each event. In addition, in inclusive measurements, the scattered

457 electron is the only particle to be detected and measured. So, it is particu-
458 larly important to make sure that electrons are well measured and properly
459 identified and are not contaminated with misidentified particles such as neg-
460 ative pions (π^-) or lost by being misidentified.

461 The process of identifying the primary scattered electrons starts by first
462 rejecting all those particle candidates which are not the first entries (i.e., the
463 trigger particles) in the event bank. The remaining sample of the candidates
464 is refined further by rejecting those with positive charges. Then, the sample
465 is further refined by applying a set of cuts that are listed and described below.
466 An electron candidate is considered good if it passes all of these cuts.

467 1. Good Electron Cuts

- 468 (a) **Cut on particle charge:** $q=-1$
- 469 (b) **Detector status cuts:**
 - 470 i. **DC status:** $dc>0$; $dc_part>0$
 - 471 ii. **SC status:** $sc>0$; $sc_part>0$
 - 472 iii. **EC status:** $ec>0$; $ec_part>0$
 - 473 iv. **CC status:** $cc>0$; $cc_part>0$
(For simulated data, all of the above except those on CC
474 variables are used.)
- 476 (c) **Electromagnetic Calorimeter Cuts** (see Sec. 3.3.1)
- 477 (d) **Osipenko cuts** Cuts on CC angle θ , ϕ and time matching be-
478 tween CC and other detectors. (see Sec. 3.3.2)
- 479 (e) **Cut on minimum number of photoelectrons** (see Sec. 3.3.2)

480 2. Good Event Cuts

- 481 (a) **Cut on minimum number of particles detected and recon-
482 structed in the event:** $gpart>0$
- 483 (b) **Minimum/maximum momentum cuts** (see Sec. 3.3.3)
- 484 (c) **Sector cut** $dc_sect = 6$; $cc_sect = 6$ (to select electrons from the
485 sector where the low momentum Cherenkov detector was installed)
- 486 (d) **Scattering vertex-z cuts** (see Sec. 3.3.4)
- 487 (e) **Fiducial cuts** (see Sec. 3.3.5)

488 This data analysis relied on comparing the experimental data with a
489 Monte-Carlo simulated data set that was as realistic as practically possible.
490 Thus, we also have to analyze the simulated data in the same way as the
491 experimental data. In the ideal situation, all cuts would be the same for
492 both experimental and simulated data. However, we could not make our
493 simulation match perfectly with our experimental data. Therefore, some of
494 the data selection cuts are defined separately for the two cases and sometimes
495 separately even for different Q^2 bins (to make sure we have the same fractions
496 of events in corresponding kinematic bins for both type of data).

497 **3.3.1 Electromagnetic Calorimeter Cuts**

498 The EC cuts consist of two different cuts applied together. One of these
499 is on the sampling fraction i.e. the fraction of the energy deposited in the
500 calorimeter, and the other is on the energy fraction deposited in the inner
501 part of the calorimeter.

502 **Cuts on EC sampling fraction**

503 While moving through the EC, charged pions are minimum ionizing particles
504 in the momentum range detectable by CLAS. On the other hand, each elec-
505 tron deposits its total energy E_{tot} in the EC³ by producing electromagnetic
506 showers. Therefore, the sampling fraction E_{tot}/p should be independent of
507 the momentum for electrons (in reality there is a slight dependence).

³Because some of the deposited energy is in the lead part of the EC rather than the scintillator, only a fraction of the electron energy is detected in the EC.

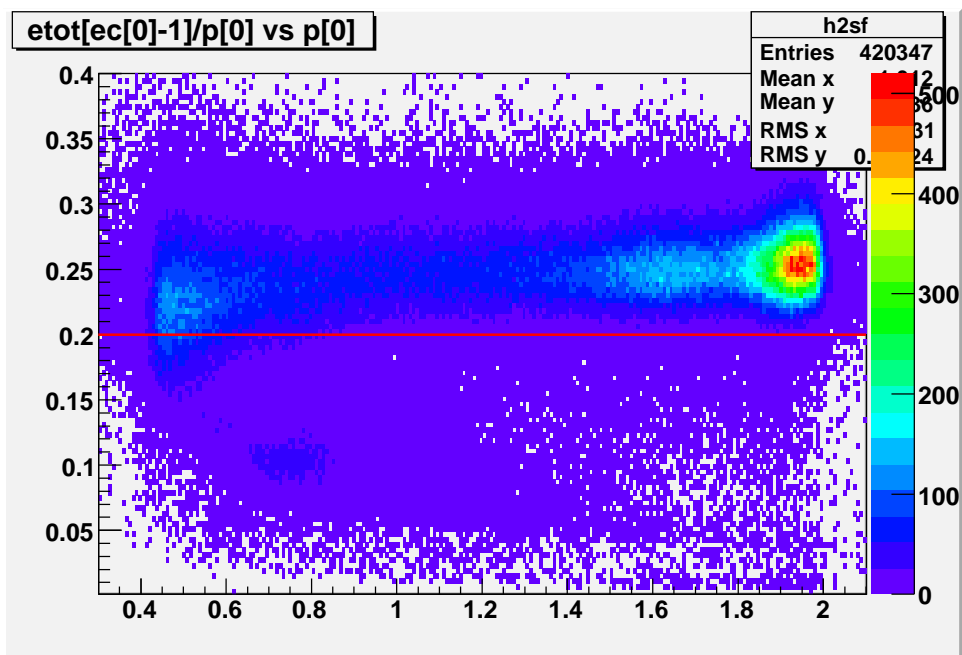


Figure 3.2: An example of the cut on the EC sampling fraction (2.0 GeV data). The plots shows the distribution of the sampling fraction (in Y-axis) plotted against the particle momentum (in X-axis). The brighter stripe above about 0.2 in the energy fraction are due to the electrons whereas those below are the pions.

508 For the EC in CLAS, the electron sampling fraction ($etot/p$) is about 0.25
509 and pions give signals that are mostly below 0.2 (see Fig. 3.2 or others that
510 follow). Therefore, a lower cut of $etot/p > 0.2$ is usually chosen to reject
511 most of the pions without significantly losing good electrons. However, in
512 our low beam energy experiment, few pions are produced and the electron
513 peaks are cleaner in lower kinematic bins as can be seen in the low Q^2 bins
514 of Fig. 3.3. Therefore, a Q^2 bin dependent cut of $etot/p > (\mu - 3\sigma)$ was
515 chosen, where μ and σ are the Gaussian fit parameters representing the mean
516 and standard deviation of the distribution in the corresponding Q^2 bin. The
517 choice of 3σ was decided by looking at the sampling fraction distributions in
518 each of the Q^2 bins and making sure that no pion signal was observed in any
519 of the bins.

520 On simulated data also, a corresponding 3σ cut was applied by first re-
521 peating the exact same procedure to get the corresponding values of μ and
522 σ from the simulated data. Using same- σ cuts in corresponding Q^2 bins of
523 both experimental and simulated data ensures that we had the same fraction
524 of data in corresponding bins from both experimental and simulated sides.

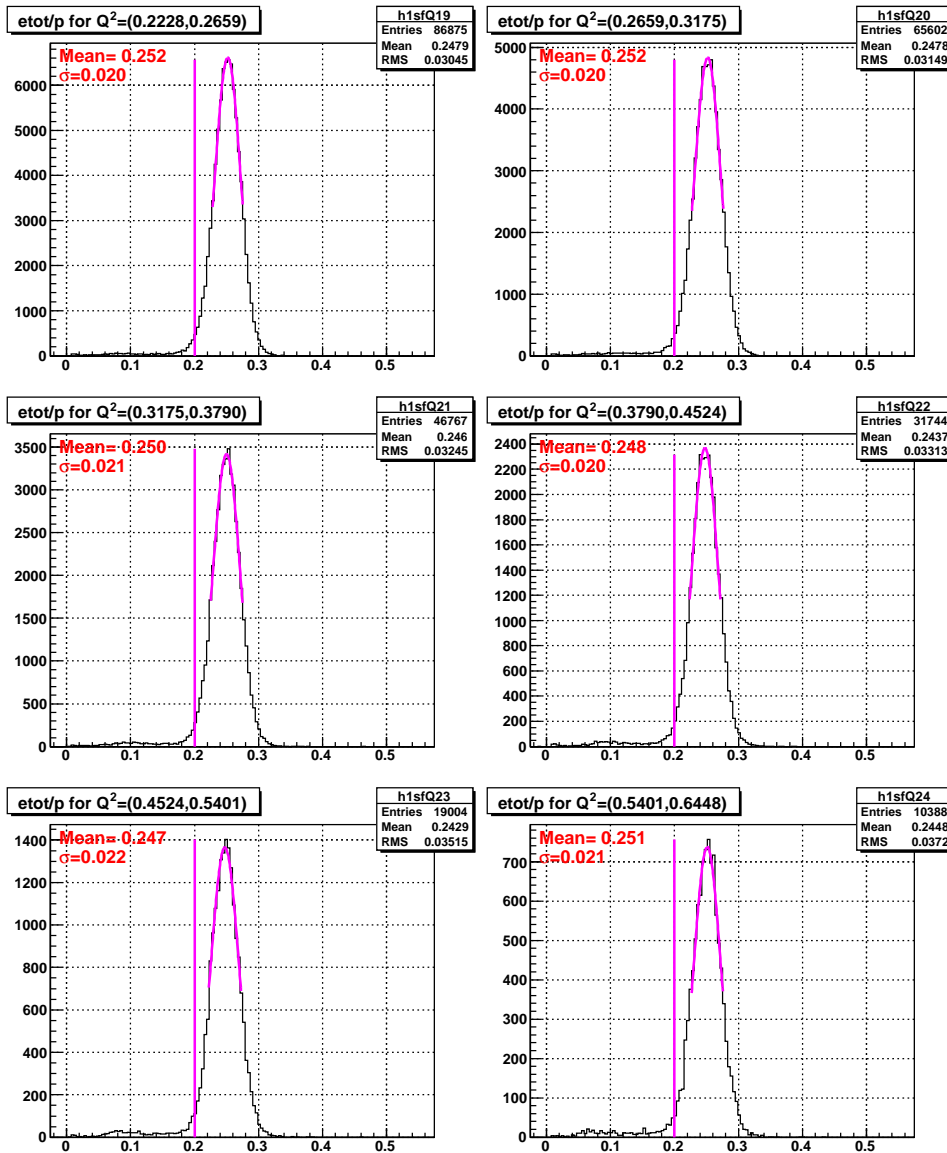


Figure 3.3: The Q^2 dependent cuts on the EC sampling fraction for 2.0 GeV experimental data. Events below the red lines are rejected.

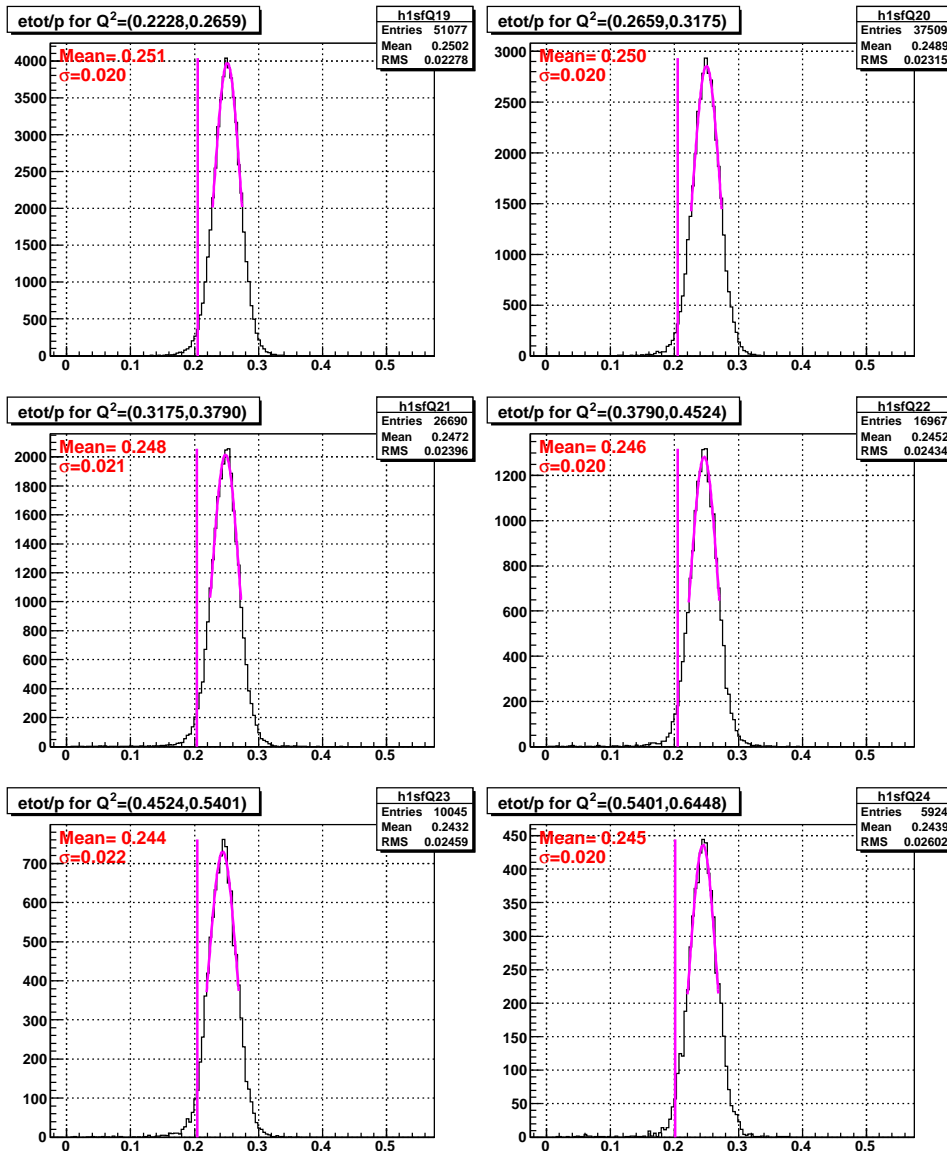


Figure 3.4: The Q^2 dependent cuts on the EC sampling fraction for 2.0 GeV simulation data. Events below the red lines are rejected.

525 **Cuts on E_{in}**

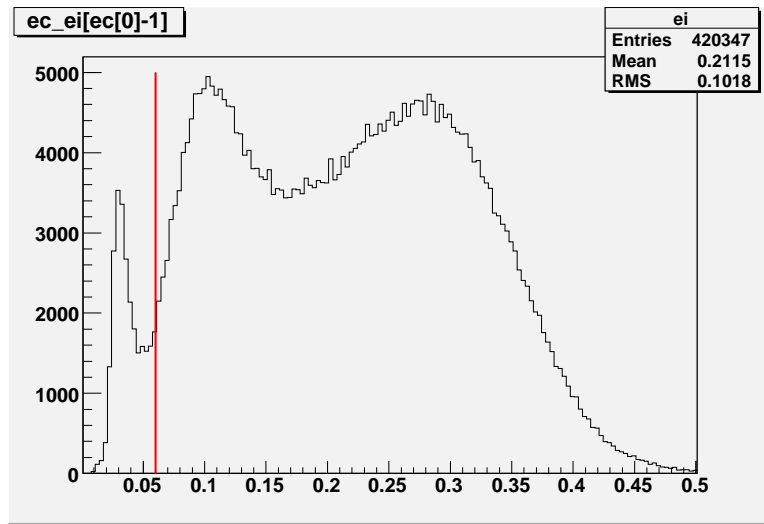


Figure 3.5: Energy deposited (GeV) in the inner EC and the cut (red line) used to reject pions (seen as a peak at about 0.03 GeV) from a sample of electron candidates of 2.0 GeV data.

526 Pions, which do not shower and are minimum ionizing particles in the
527 momentum range detected in CLAS, deposit only a small amount of energy
528 in the inner part of the EC, independent of their momentum. When E_{in} is

529 histogrammed, the small pion signal peak at about 0.03 clearly stands out
530 from the large electron sample, with little overlap in between. So, a universal
531 cut of $E_{in}=0.05$ on both data and simulation (as shown by figures 3.5, 3.6
532 and 3.7) safely rejects most of the pions from the electron candidate sample.

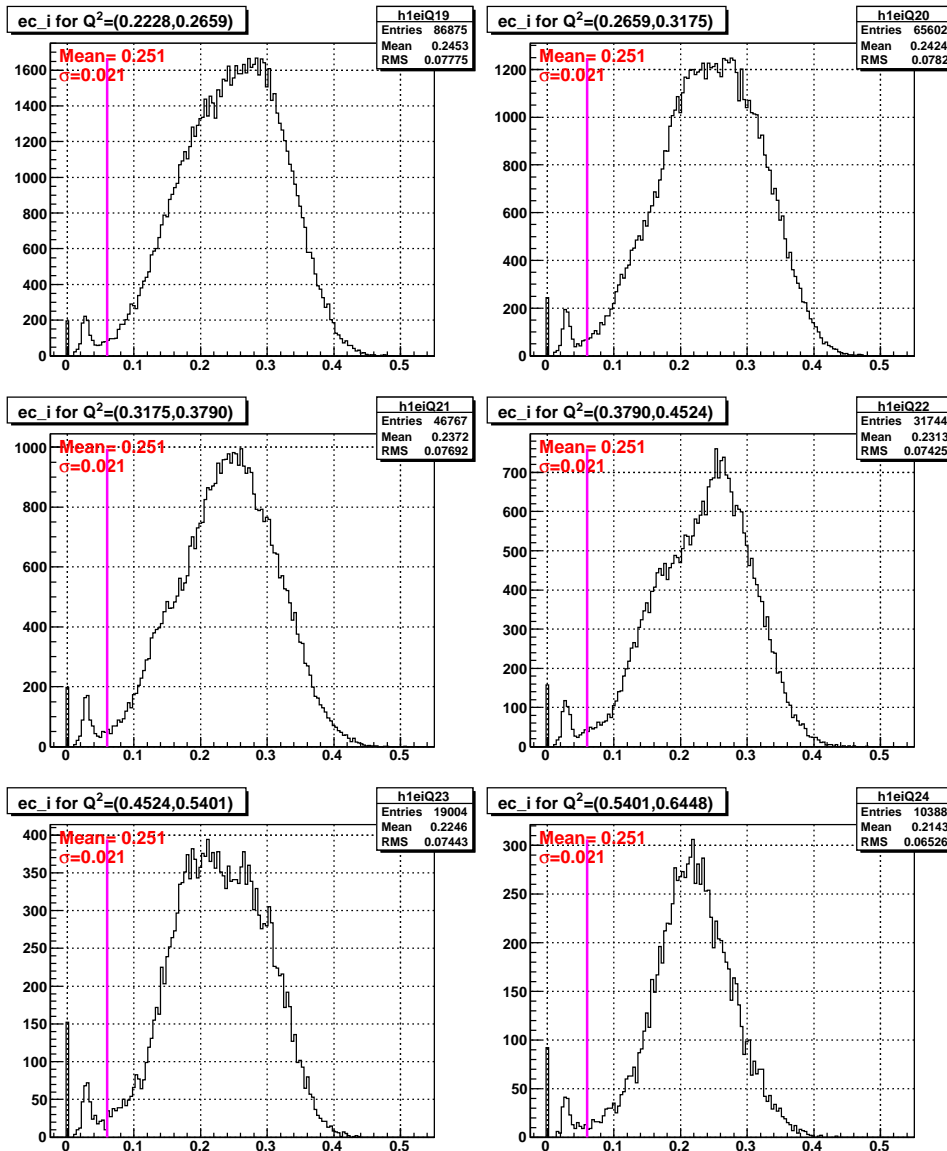


Figure 3.6: The EC-inner cut on a sample of 2.0 GeV experimental data in various Q^2 bins.

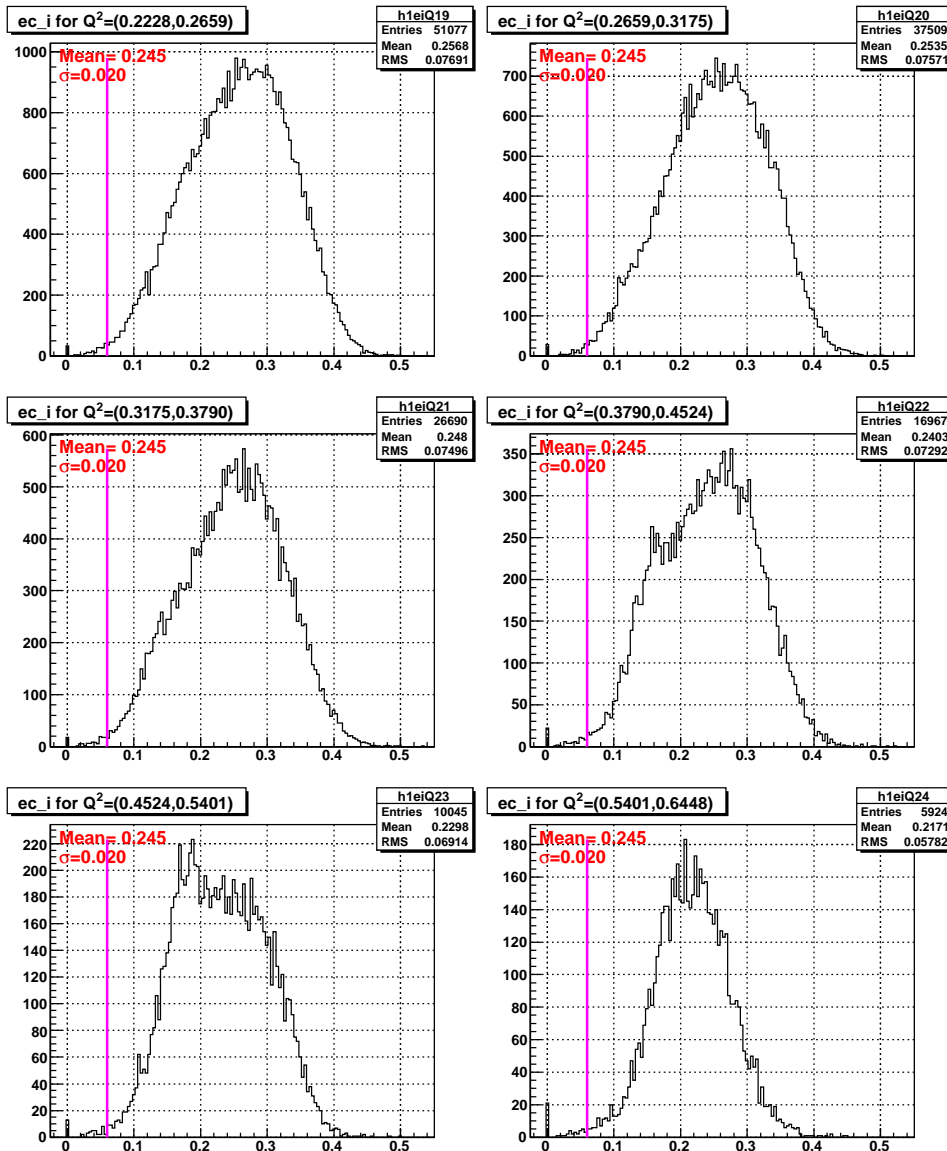


Figure 3.7: The EC-inner cut on a sample of 2.0 GeV simulation data in various Q^2 bins.

533 **3.3.2 Cerenkov Counter Cuts**

534 **Osipenko (CC Geometry and Time Matching) Cuts**

535 As discussed in Sec. 2 the new EG4-dedicated CC consists of 11 modules
536 each consisting of a pair of mirrors and PMTs. The segments are placed
537 along the CLAS polar angle covering 15 to 45 degrees, i.e., the segments are
538 at different polar angular positions. During normal operation, the PMTs of
539 these segments may produce thermal noise that is equivalent to that produced
540 by one photo-electron passing through it. As a result, when a noise pulse in
541 the CC and a pion track measured by DC coincides within the trigger window
542 of the CLAS detector, the track gets registered as an electron candidate by
543 the event reconstruction program, thus contributing to the contamination of
544 electron candidates with the misidentified pion tracks. In fact, this turns out
545 to be the biggest source of pion contamination. In order to minimize such
546 contamination and help better identify electrons from pions, CC geometric
547 and time-matching cuts are applied.

548 This category of cuts for this experiment is mostly based on a similar
549 analysis done for another CLAS experiment by M. Osipenko [21, 22].

550 The first requirement in the CC-matching is for the electron candidate
551 track (as reconstructed by DC) to have a corresponding signal in CC. In ad-
552 dition, the track needs to meet several matching conditions to be acceptable
553 as described in the next sections.

554 **CC θ Matching** As said above, the CC segments are at different average
555 polar angle positions (between 15 and 45 degrees), so in principle, one can
556 expect a one-to-one correspondence between the polar angle of the track (as
557 measured at the vertex) and the CC-segment. However, the torus magnetic
558 field bends the particles towards or away from the beamline, so it's more
559 convenient to use the CC projected polar angle θ_{proj} rather than the vertex
560 angle θ , where θ_{proj} is defined as the polar angle of the position vector defined
561 by the point of intersection of the track with the plane at which the CC
562 PMTs reside as reflected by the CC mirrors (another projected angle ϕ_{proj}
563 is the azimuthal angle of the same vector). These projected angles can be
564 uniquely calculated for each track based on the DC signals of the track as
565 well as the CC geometry information. To simplify the later analysis process,
566 these projected angles for each track were calculated during the final data
567 reconstruction process and then saved in the output files just like all the other

568 information for the events and particles. Finally, for the actual electrons
 569 a one-to-one correspondence between θ_{proj} and the segment number can be
 570 established, which discriminates against background noise and the accidental
 571 pions (or any other negative charge candidates). For each segment, the θ_{proj}
 572 distribution (see Fig. 3.8) is fitted with a gaussian to determine its mean (μ)
 573 and width (σ) and then saved for future use in cuts. These fit parameters
 574 are then used during the data analysis to define these CC- θ -matching cuts.
 575 The events that have $\mu - 3\sigma < \theta_{proj} < \mu + 3\sigma$ pass this cut, and the others
 576 are rejected as not genuinely being electrons.

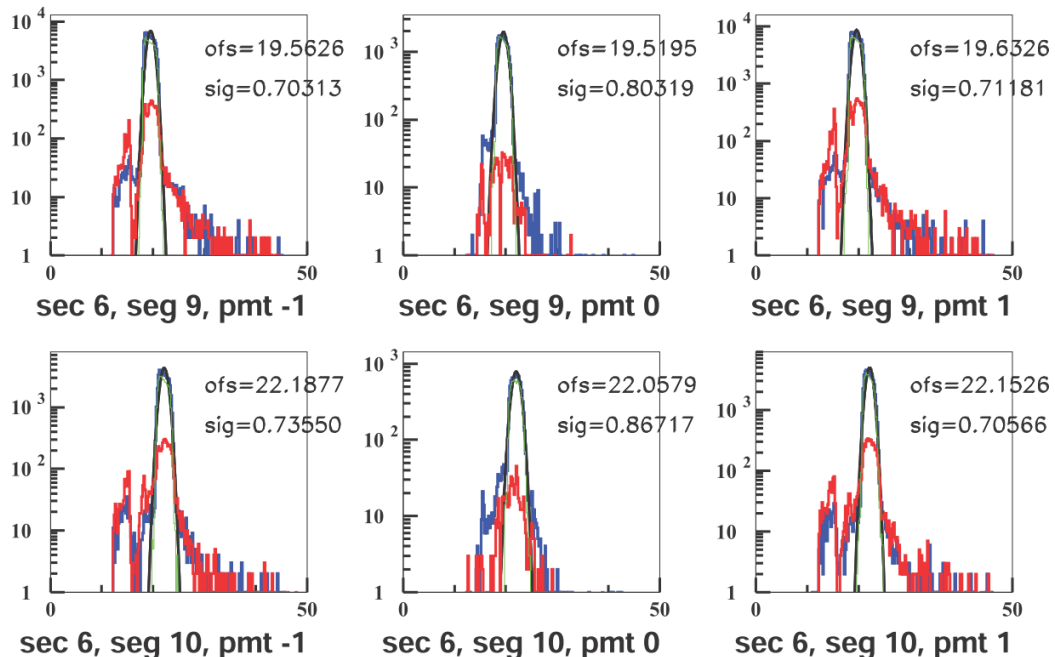


Figure 3.8: The θ_{proj} distributions in two (9th and 10th) of the CC-segments (figures used from [22]). Here, the first, second and third columns correspond to events that fired the left, both and the right PMTs respectively. The blue lines are for good electron candidates that pass the EC cuts as well as $Nphe > 2.5$. The red ones are for those that pass the EC cuts but with $Nphe < 2.5$ (thus likely pions), and the green lines (not visible due to being nearly identical to the blue ones) are for those which pass both EC cuts and all Osipenko cuts. The Gaussian fits which are used to define the θ matching cuts are shown in black ("ofs" and "sig" in the panel refer to μ and σ , respectively). If the candidate falls outside $\pm 3\sigma$ limits given by the fit, θ_{proj} is taken as not matching with the corresponding segment and, therefore, the event is rejected.

577 **CC ϕ Matching** One can also have a one to one correspondence between
578 the other CC-projected angle ϕ_{proj} and the left or right PMT in the corre-
579 sponding CC-segment, because when the track is on the right side of the CC,
580 the right PMT should fire and vice versa. However, there are some excep-
581 tional cases of events which fire both PMTs. That happens when ϕ_{proj} of the
582 track is less than 4 degrees (when measured relative to the sector mid-plane),
583 in which case the Cerenkov light hits both PMTs but with less efficiency (be-
584 cause the Cherenkov photons are shared between the two). Fig. 3.9 shows
585 for two of the segments the ϕ_{proj} distributions and the Gaussian fits that are
586 used to define these cuts.

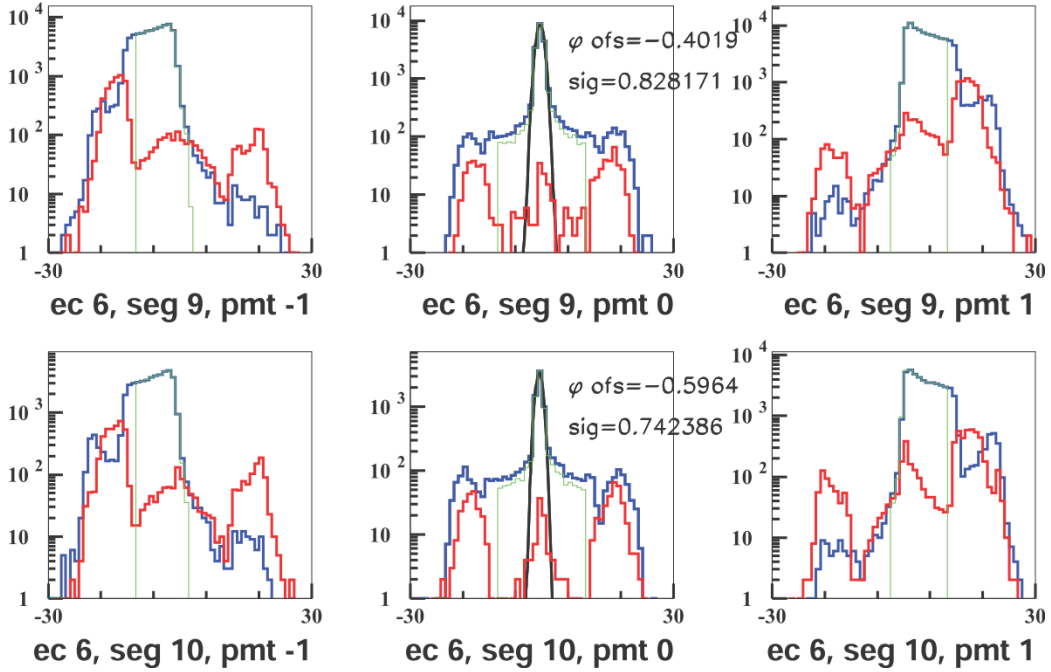


Figure 3.9: The ϕ_{proj} distributions in two (9^{th} and 10^{th}) of the CC-segments (figure used from [22]). Here, the first, second and third columns correspond to events that fired the left, both and the right PMTs respectively. The blue lines are for good electron candidates that pass the EC cuts as well as $Nphe > 2.5$. The red ones are for those that pass the EC cuts but with $Nphe < 2.5$ (thus likely pions), and the green are for those which pass both EC cuts and all Osipenko cuts. The Gaussian fits to the distributions that fired both left and right PMTs are shown in black ("ofs" and "sig" in the panel refer to μ and σ , respectively). If the candidate falls outside 3σ on the positive (negative) side but the left (right) PMT is fired, we take it as having left-right inconsistency and, therefore, the event is rejected. In other words, if $\theta < \mu - 3\sigma$ but $PMT = 1$, or if $\theta > \mu + 3\sigma$ but $PMT = -1$, the event is rejected.

587 **CC Time Matching** The difference ΔT between the track time recorded
 588 on a CC segment and the corresponding time recorded on the TOF (or SC),
 589 corrected for the path length from the CC to the TOF, is used to define one of
 590 the time-matching cuts $\Delta t_{SC-CC} > -6.0\text{ns}$ which was chosen to reduce pion
 591 contamination without losing too many electron candidates (see Fig 3.10).
 592 Likewise, the time between CC and EC is also used to define another cut
 593 $\Delta t_{EC-CC} > -6.0\text{ns}$ (see Fig 3.11) to further reduce the pion contamination.

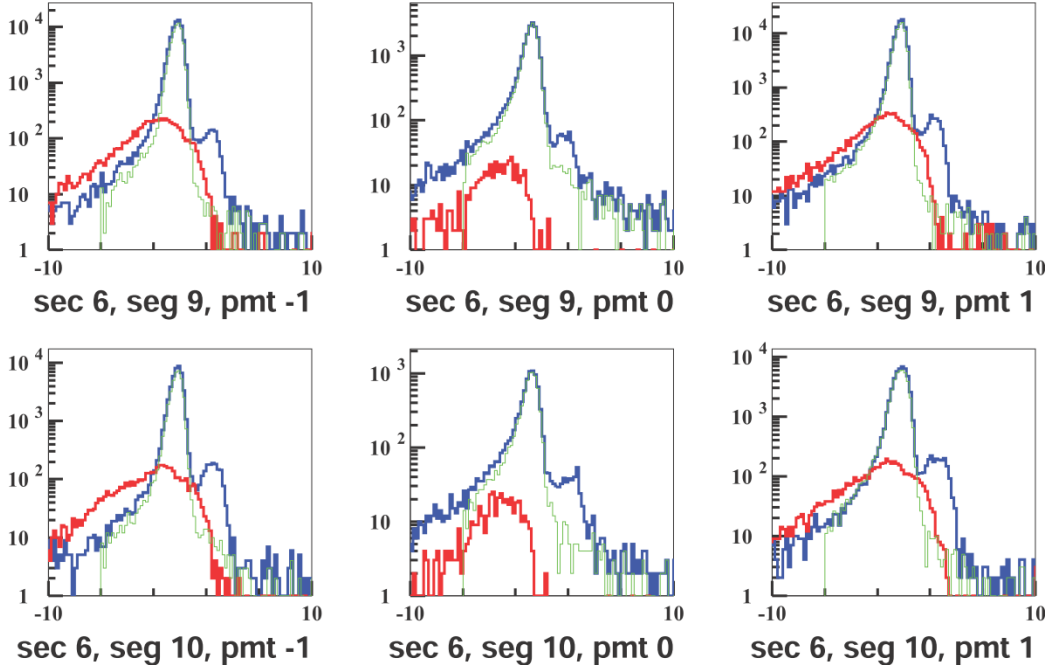


Figure 3.10: The Δt_{SC-CC} distributions for two of the CC-segments (figure used from [22]). Here, the first, second and third columns correspond to events that fired the left, both and the right PMTs respectively. The blue lines are for good electron candidates that pass the EC cuts as well as $Nphe > 2.5$. The red ones are for those that pass the EC cuts but with $Nphe < 2.5$ (thus likely pions), and the green are for those which pass both EC cuts and all Osipenko cuts. The $\Delta t_{SC-CC} > -6.0\text{ns}$ cut was chosen to reduce pion contamination without losing too many electron candidates. (The small peaks at about +3 ns are due to particles hitting PMTs directly.)

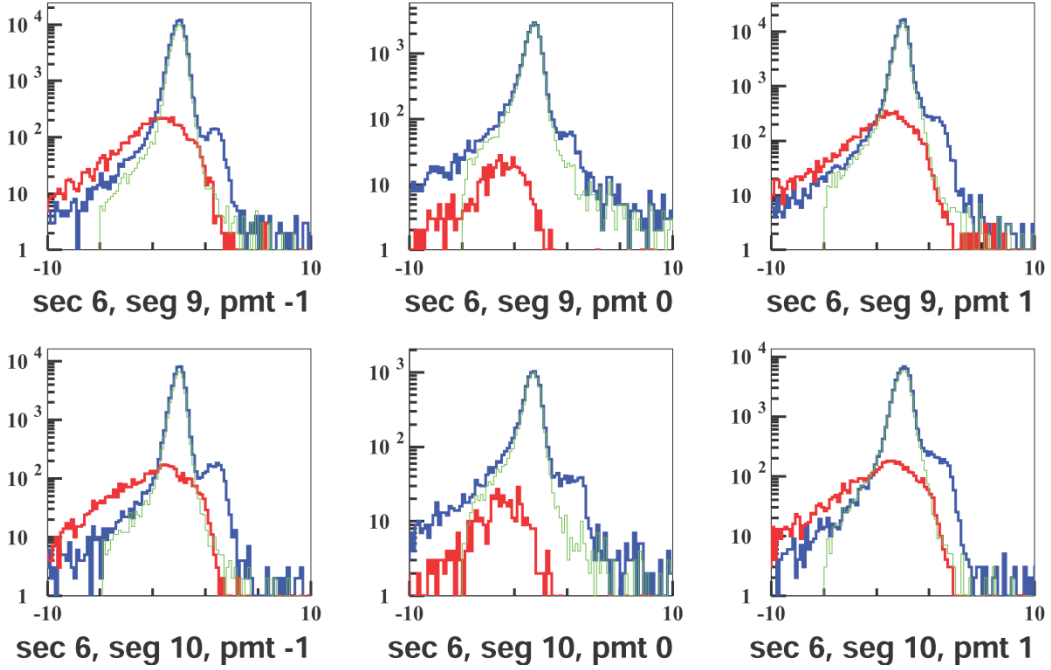


Figure 3.11: The Δt_{EC-CC} distributions for two of the CC-segments (figure used from [22]). Here, the first, second and third columns correspond to events that fired the left, both and the right PMTs respectively. The **blue** lines are for good electron candidates that pass the EC cuts as well as $Nphe > 2.5$. The **red** ones are for those that pass the EC cuts but with $Nphe < 2.5$ (thus likely pions), and the **green** are for those which pass both EC cuts and all Osipenko cuts. The $\Delta t_{EC-CC} > -6.0\text{ns}$ cut was chosen to reduce pion contamination without losing too many electron candidates. (The small peaks at about +3 ns are due to particles hitting PMTs directly.)

594 Cut on Minimum Number of Photoelectrons

595 The “nphe” variable in the data ntuple which represents the ADC signal from
 596 the CC converted to “number of photoelectrons” and multiplied by 10 is also
 597 used to discriminate electrons from pions and the background. The number
 598 of photoelectrons produced in CC by an electron is typically between 5 and 25
 599 or between 50 and 250 in the units of nphe, where the electronic background
 600 and negative pions produce signals equivalent to one photo-electron (or 10 in
 601 nphe units) and so a cut is determined somewhere between these two regions
 602 based on the shapes and sizes of the electron and pion peaks. In our case,

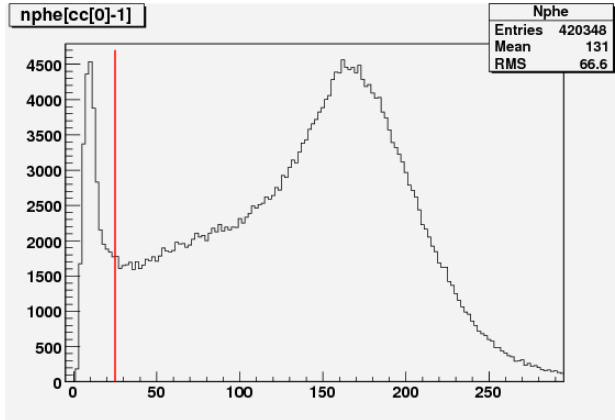


Figure 3.12: The cut (the red straight line at 25) on the number of photoelectrons produced in CC times 10 (from 2.0 GeV data). The signals below the red line are mostly pions and noise and above the line are mostly electrons.

603 we chose to have the cut $Nphe > 25$ as depicted by the straight line in Fig.
 604 3.12.

605 3.3.3 Minimum/Maximum Momentum cuts

606 A study [23] of the inclusive cross section at various beam energies in CLAS
 607 developed a parametrization of the low momentum cut p_{min} as a function of
 608 the calorimeter low trigger threshold (in milli-Volts)

$$p_{min} \text{ (MeV)} = 214 + 2.47 \times EC_{threshold} \text{ (mV)} \quad (3.2)$$

609 The low threshold for EC-total energy for EG4 was 65 mV [24], so, the
 610 minimum momentum cut was determined to be at: $p_{min} = 0.37 \approx 0.4 \text{ GeV}$.
 611 In addition, another minimum cut of $p_{min} = 0.2 * E_{beam}$ was added, so the
 612 actual minimum cut amounted to the larger of those two. Likewise, the
 613 momentum cannot be more than that of the beam energy (in natural units),
 614 therefore, the upper cut on the momentum is: $p_{max} = E_{beam}$.

615 Fig. 3.13 shows the momentum distribution of the electron candidates
 616 for the 2 GeV data and the minimum and maximum cuts.

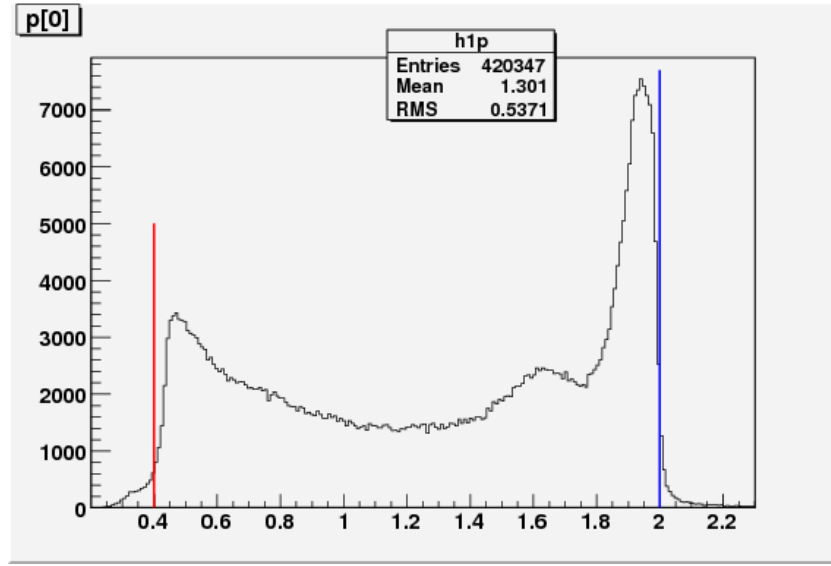


Figure 3.13: The maximum and minimum momentum cuts (on 2.0 GeV ND₃ data).

617 3.3.4 Vertex-Z cuts

618 In the EG4 experiment, the ND₃ polarized target was of 1 cm long and was
619 placed at ($x = 0$, $y = 0$, $z = -100.93$ cm) in the CLAS coordinate system.
620 Since the beam electrons have to go through a few foils before reaching the
621 target as well as the detector, we want to reject electron tracks with vertices
622 outside the target volume. For this purpose, use a cut on the reconstructed
623 vertex co-ordinate “ v_z ”. However the vertex resolution demands reasonably
624 wide “ v_z ” cuts so as not to lose too many good events. That is why the
625 distribution of “ v_z ” was studied and based on the position and width of
626 the distribution as well as our knowledge of the location of various foils and
627 target materials, the cuts on “ v_z ” were decided. It was seen (see Figs. 3.14
628 and 3.15) that the resolutions get worse and the distributions get wider as
629 we go to lower Q^2 values, so again Q^2 dependent cuts were chosen for both
630 data and simulation with the cuts tightening as Q^2 increases.

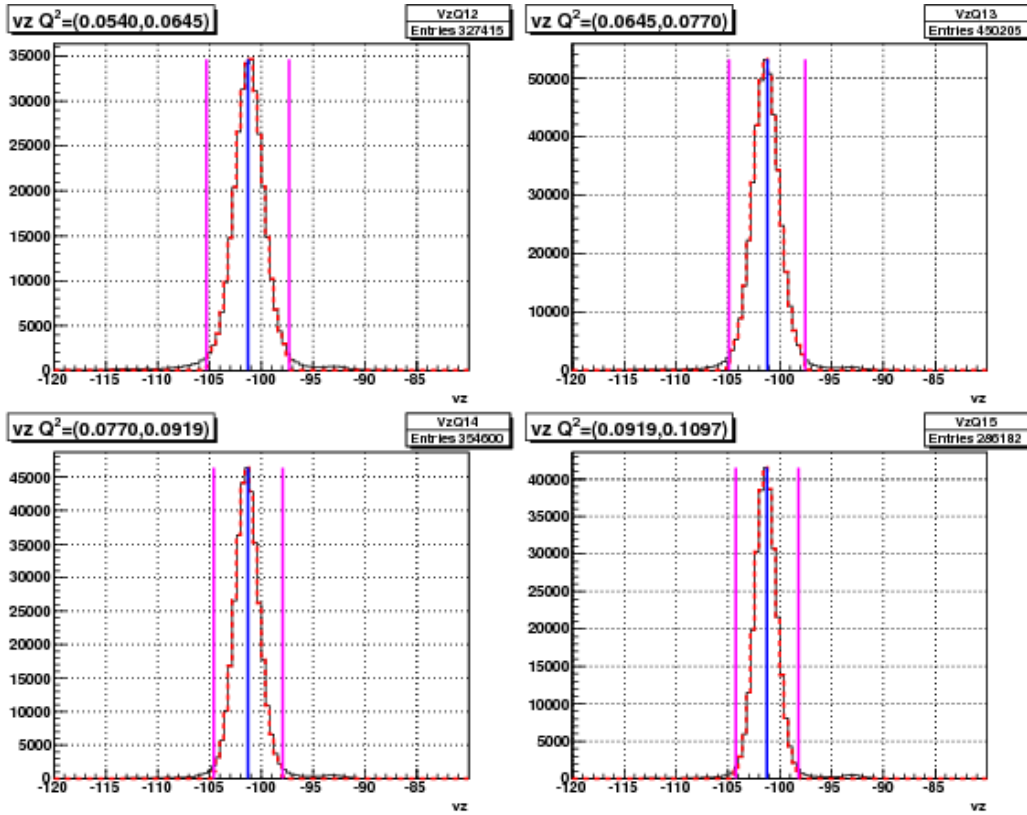


Figure 3.14: 2.0 GeV data showing the Q^2 dependent v_z -cuts (the magenta lines on the left and right of the peaks) in some of the Q^2 bins. The continuous black line represents events before applying all the other event selection cuts (except on v_z) and the thicker dotted red line are the events after the cuts. The blue lines are the centers of the distributions, from which the cuts are 3 times σ away on each side, where σ is the standard deviation for the distribution in the given Q^2 bin (both the central value and the σ are determined during the cut development studies).

As in the case of EC variables, the reconstructed “ v_z ” distribution in the simulation does not come out quite the same as in the experimental data . To have the same fraction of events in the corresponding Q^2 bins as in the experimental data, a separate set of cuts (determined based on the distributions of both types of data) had to be used for simulation. For this purpose, the Gaussian fit parameters μ and σ (representing the mean and standard deviation) for all the Q^2 bins were tabulated separately for both

638 data and simulation and separate sets of $\pm 3\sigma$ cuts were determined for all
 639 bins. For example, if μ_q and σ_q were the two Gaussian fit parameters for the
 640 q^{th} Q^2 bin of either data or simulation, then the lower and upper cuts for
 641 “ v_z ” for that data set in the given Q^2 bin would be $\mu_q - 3\sigma_q$ and $\mu_q + 3\sigma_q$
 642 respectively (as shown by the magenta vertical lines in Figs. 3.14 and 3.15).

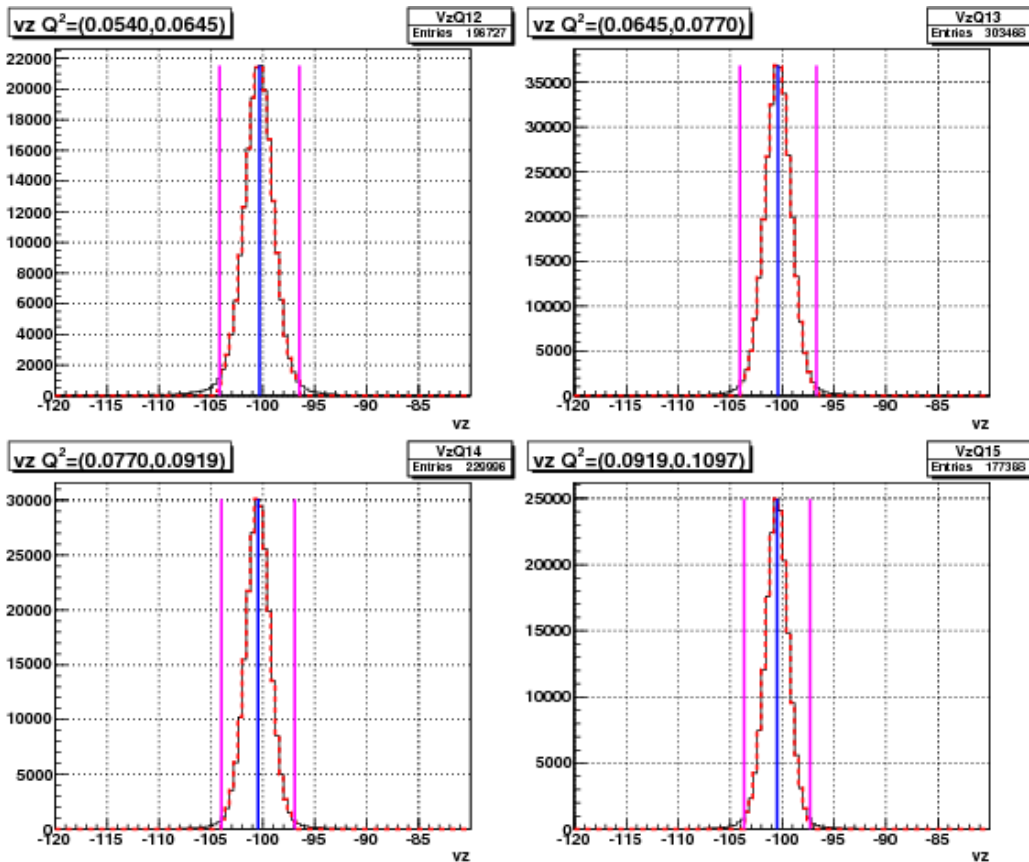


Figure 3.15: Q^2 dependent v_z -cuts on simulation data (similar to Fig. 3.14).

643 3.3.5 Fiducial Cuts

644 Similar to the cuts discussed so far, we also had to match the region of good
 645 efficiency of the physical detector with the corresponding region from the
 646 simulation. For the experimental and simulation data to be comparable,
 647 they must have the same detector acceptance. Two event variables polar

648 angle (θ_{vtx}) measured at the vertex and the azimuthal angle ϕ_{DC1} measured
 649 at the drift chamber layer 1 are chosen to define the good efficiency regions of
 650 the detector. The reason for the choice of the variable θ_{vtx} should be obvious
 651 because it is directly related with the kinematic variables Q^2 and W used in
 652 the analysis. However, due to the momentum dependent rotational effect of
 653 the magnetic field on the reconstructed azimuthal angle (ϕ_{vtx}) at the vertex,
 654 the angle ϕ_{DC1} is preferred over ϕ_{vtx} to define the fiducial region because
 655 that allows the easy selection (rejection) of the events which passed through
 656 and got detected by the more (less) reliable central (marginal) regions of
 657 the Cerenkov Counters. After a careful and extensive study of the event
 658 distributions on both data and simulation, we arrived at four sets of fiducial
 659 cuts in terms of the variables θ_{vtx} , ϕ_{DC1} and the torus current normalized
 660 inverse momentum i.e., $I_{torus}/(2250p)$.

661 The first set (see Fig. 3.16) of fiducial cuts were determined by comparing
 662 regular and EC-only data (which were taken using triggers that didn't
 663 involve CC) and selecting cuts such that regions with relatively darker spots
 664 (reflecting very low CC-efficiency) were rejected.

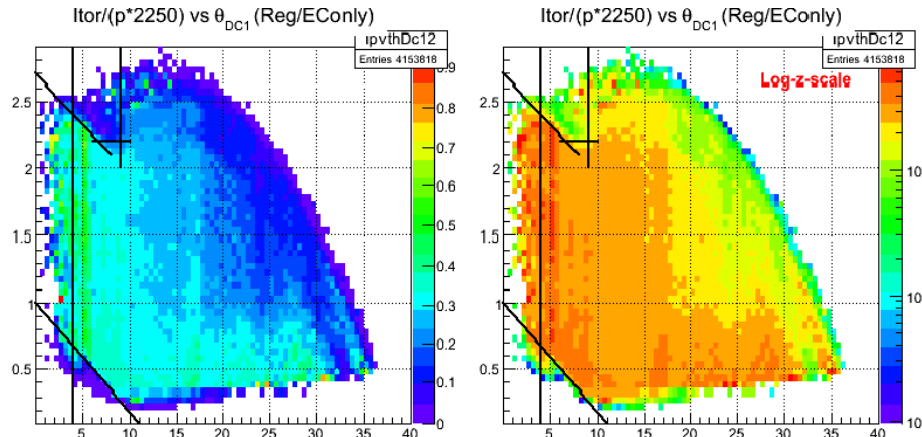


Figure 3.16: Fiducial cuts determined by comparing the distributions of regular and EC-only **experimental data** as a function of $I_{torus}/(2250p)$ and θ_{DC1} . Here in the top panels, we see distributions of ratios of the regular and EC-only data respectively in linear and log scales in the color axis respectively. Inefficient regions of the CC are excluded using the indicated cuts.

665 The second set of cuts came from a similar comparison between the regu-
 666 lar and EC-only data in the $I_{torus}/(2250p)$ vs θ_{vtx} (instead of θ_{DC1}) space (see

667 Fig. 3.17) .

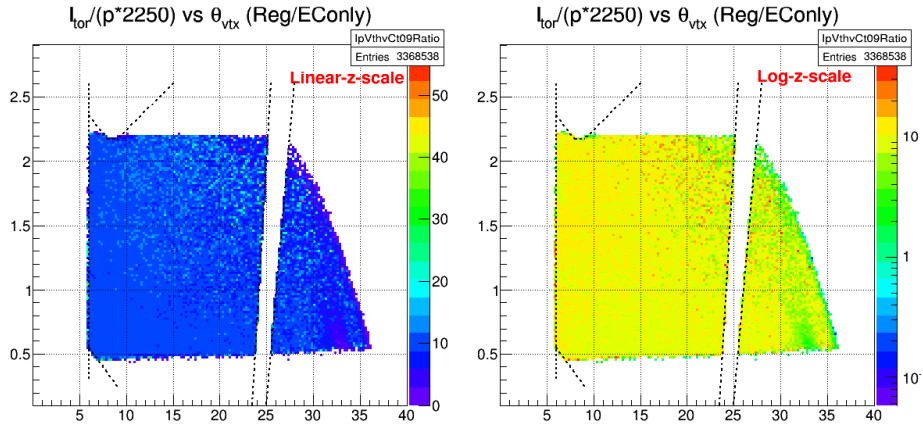


Figure 3.17: Fiducial cuts determined by comparing the distributions of regular and EC-only **experimental data** as a function of $I_{torus}/(2250p)$ and vertex angle θ_{vtx} . Here, the vertical cut near $\theta_{vtx}=25$ degrees is to avoid the region of low efficiency possibly due to dead wires in DC.

668 The third set of cuts came from a comparison between the experimental
669 and the corresponding simulated data as shown in the Fig. 3.18. as indicated
670 by various straight lines in the two plots.

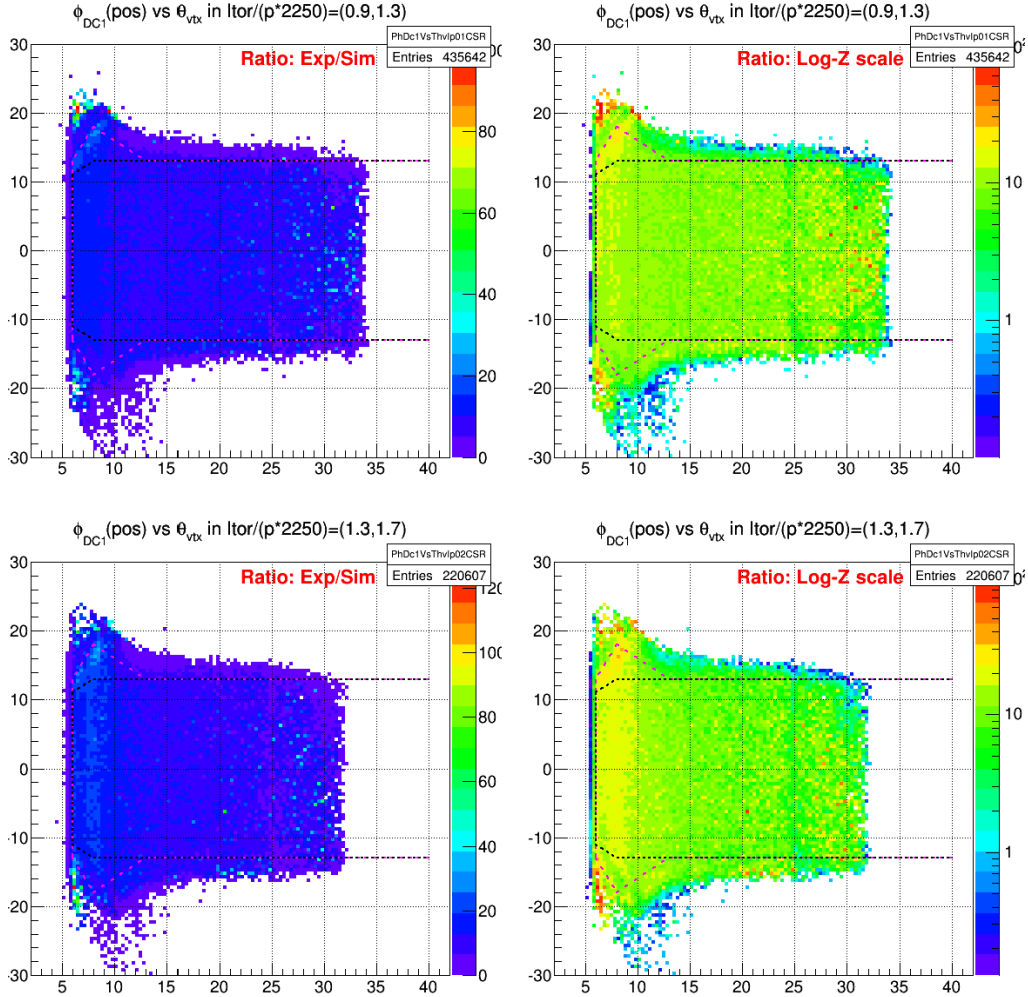


Figure 3.18: Distribution (in two of six bins of $I_{torus}/(2250p)$) of ratios of **experimental** and **simulated** data (for 2.0 GeV) (both in linear and log-z scales) as a function of vertex angle θ_{vtx} and azimuthal angle ϕ_{DC1} as measured by the track position at the first drift chamber layer (angles in degrees). The dotted lines indicate the fiducial cuts for accepting good electrons.

671 Lastly, further sets of cuts were developed based on the distribution of
 672 the average number of photo electrons (nphe) as recorded by the Cerenkov
 673 Counter (CC) (see Fig. 3.21).

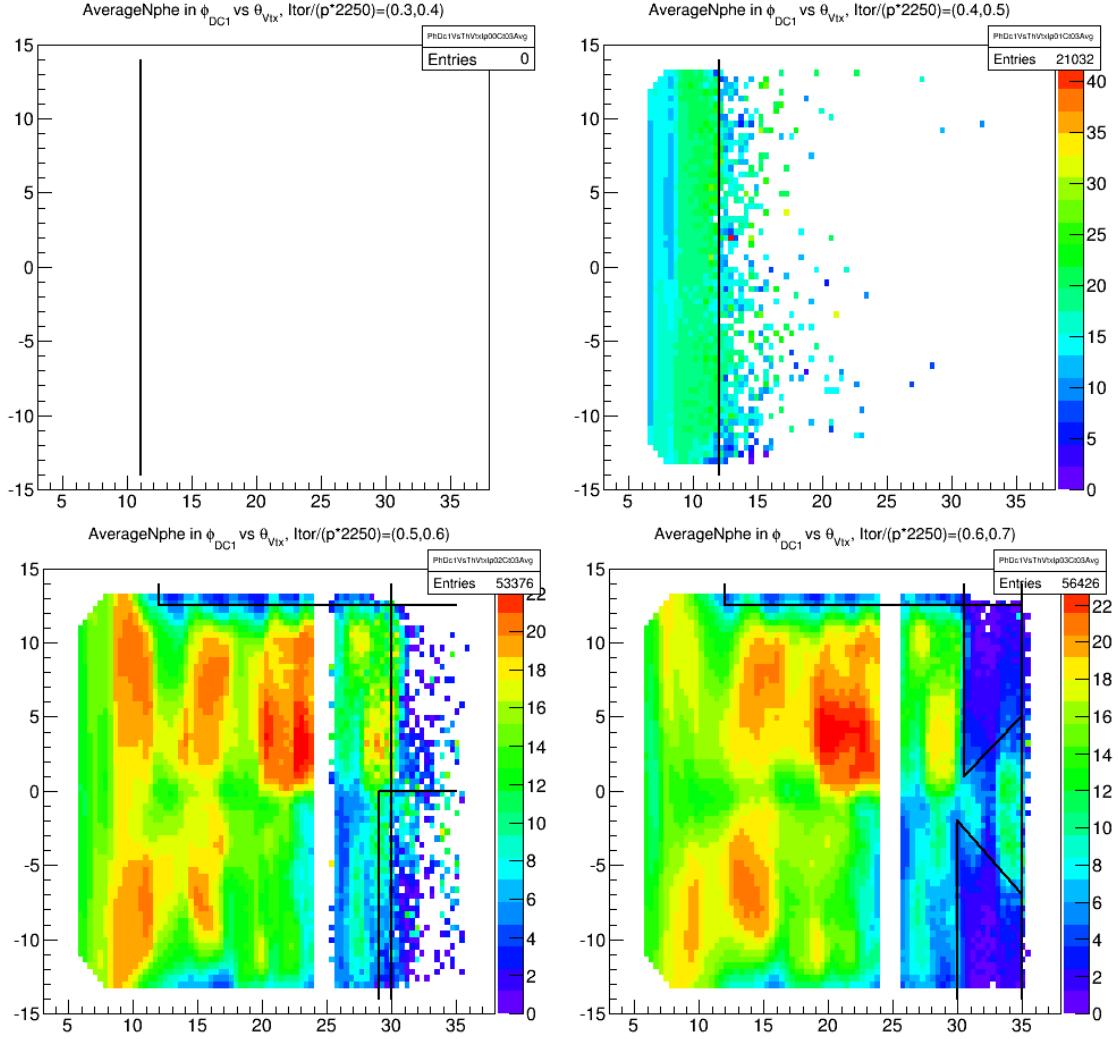


Figure 3.19: Average Nphe distributions as a function of ϕ_{DC1} (along Y-axis) and θ_{vtx} (along X-axis) in first four bins of $\frac{I_{tor}}{p \cdot 2250}$. The black lines show the cuts that reject the very low CC-inefficiency regions.

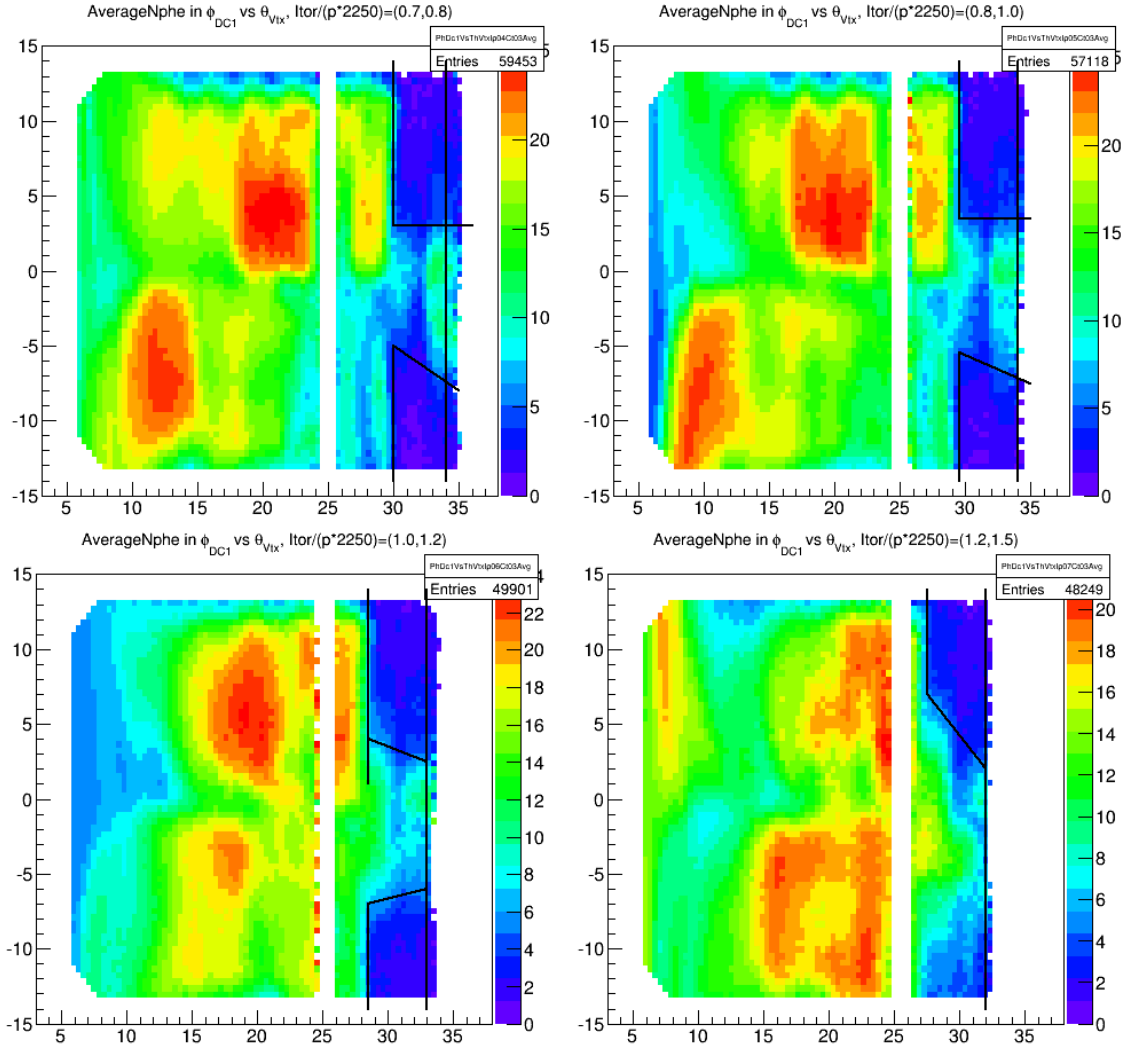


Figure 3.20: Average Nphe distributions as a function of ϕ_{DC1} (along Y-axis) and θ_{vtx} (along X-axis) in next four bins of $\frac{I_{tor}}{p \cdot 2250}$. The black lines show the cuts that reject the very low CC-inefficiency regions.

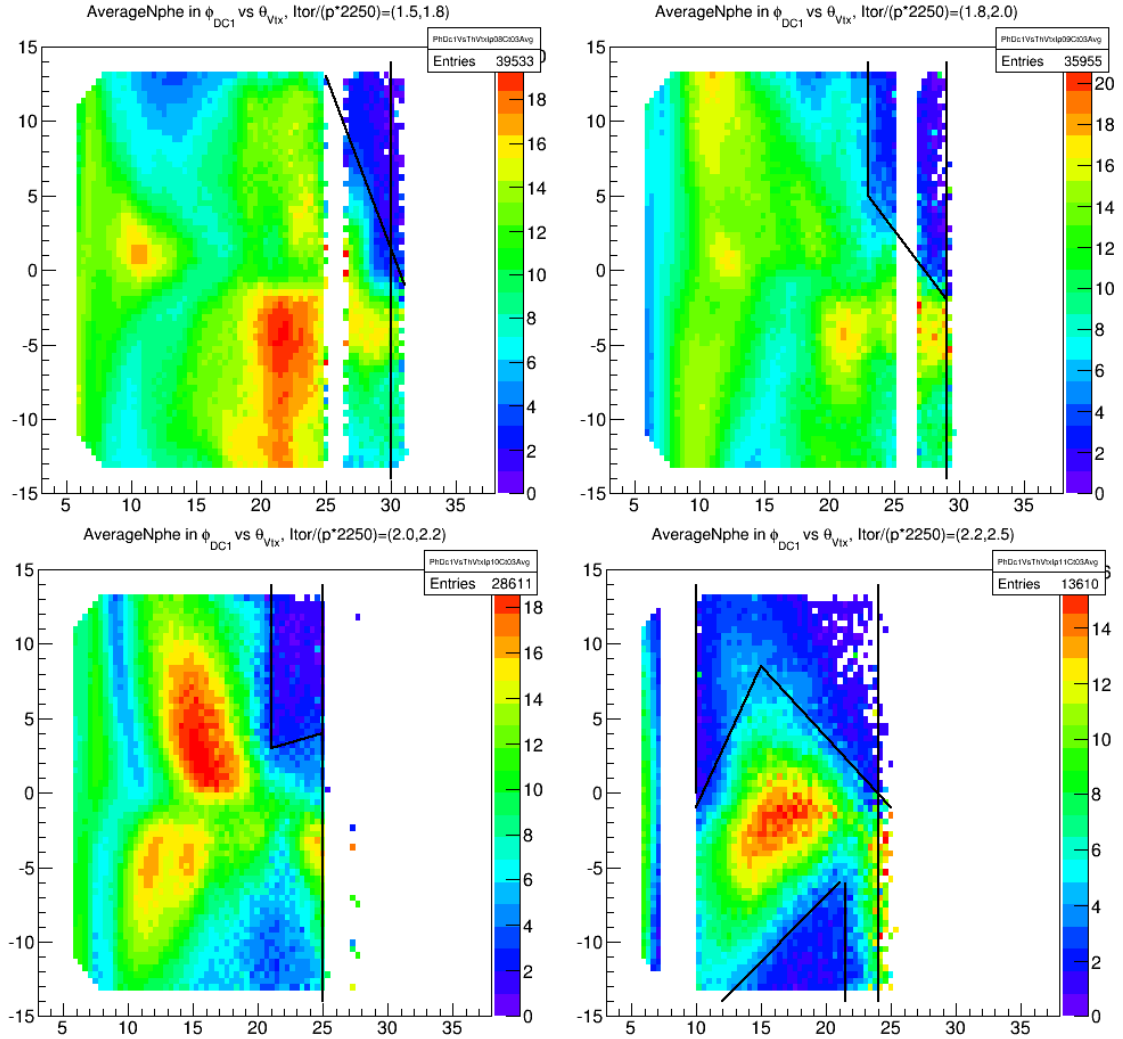


Figure 3.21: Average Nphe distributions as a function of ϕ_{DC1} (along Y-axis) and θ_{vtx} (along X-axis) in last four bins of $\frac{I_{tor}}{p^*2250}$. The black lines show the cuts that reject the very low CC-inefficiency regions.

674 3.4 Data Quality and Stability Checks

675 With an available set of good event/electron selection cuts, beam charge
676 (measured by Faraday cup) normalized total event counts (sometimes also
677 known as event “yield”), as well as polarization dependent differences, were
678 calculated for each of the data files for all the runs and then plotted against
679 the run number to study the data quality and stability as shown by Figs.
680 3.22, 3.23 and 3.24.

681 If nothing unusual happened or if the experimental conditions are not
682 changed, then it is expected that the event yield as well as the count differ-
683 ences remain constant over time. Therefore, the graphs of these event counts
684 plotted versus time or run number (which also roughly reflect the flow of
685 time) should indicate the stability and quality of the data collected. For
686 example, Fig. 3.22 shows such a total yield plot for all the data files from
687 the 2.0 GeV beam energy data set on deuteron target. We can see that these
688 data runs display some features of instability over the full period of time, but
689 stability over short time periods. For example, all the data with run numbers
690 below about 51610 show significantly higher event yield than the runs after
691 that run (possibly due to beam-target misalignment as indicated by raster
692 magnet ADC values in Fig 3.24).

693 Likewise, the stability of the polarized count differences in the elastic
694 region ($0.9 \text{ GeV} < W < 1.0 \text{ GeV}$) as well as separately in the delta (Δ)
695 resonance region were studied by plotting them versus the same run numbers
696 (here the elastic and Δ -resonance regions are considered separately, because
697 the spin asymmetries in these two regions have opposite signs, which would
698 have decreased the observed difference if combined. To further enhance the
699 sensitivity of the observation, the difference of the count differences measured
700 in the elastic and Δ -resonance regions as given by

$$\Delta N_{elastic} - \Delta N_{\Delta-res} = \frac{1}{P_b P_t} \left[\left(\frac{N^+}{FC^+} - \frac{N^-}{FC^-} \right)_{elastic} - \left(\frac{N^+}{FC^+} - \frac{N^-}{FC^-} \right)_{\Delta} \right] \quad (3.3)$$

701 were plotted (see Fig. 3.23). It was observed that this elastic normalized
702 count difference (which is what really matters to our analysis, in the end)
703 was much more stable than the total yield.

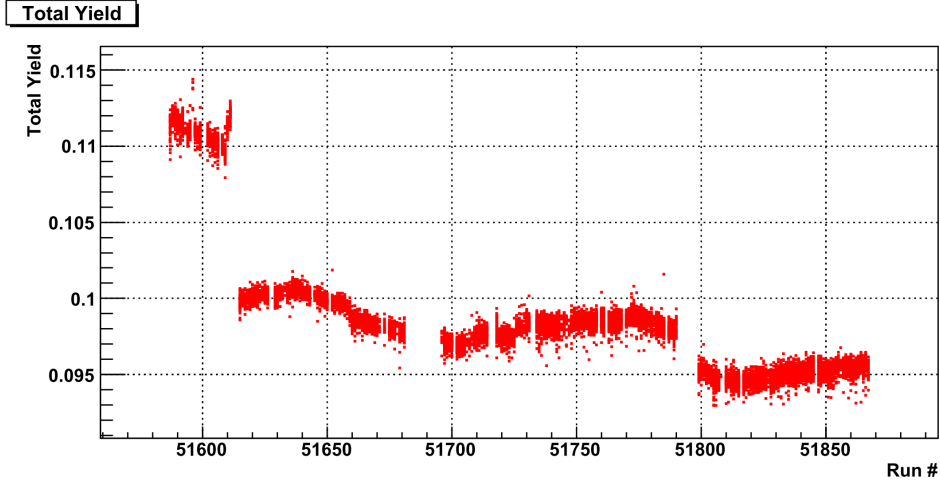


Figure 3.22: Total normalized yield ($= \frac{N^+ + N^-}{FC^+ + FC^-}$) for 2.0 GeV ND₃ runs.

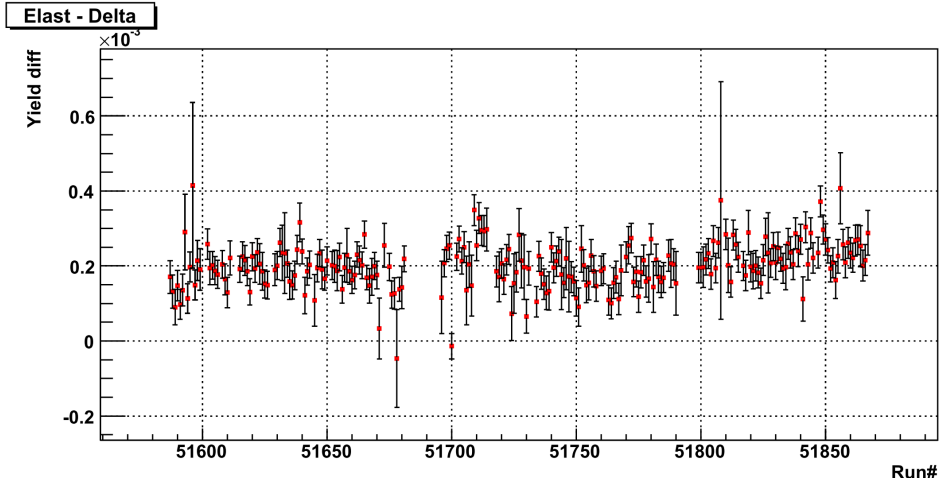


Figure 3.23: Polarized yield differences (Eq. 3.3) normalized with $P_b P_t$ and BPM/F-cup for elastic peak minus that for the Δ peak for the 2.0 GeV ND₃ runs.

704 The same was also repeated for the other variables such as the root-
 705 mean-square of the ADC values (see Fig. 3.24) which carry information on
 706 the X and Y coordinates of the beam at the interaction vertex, thus their
 707 plots giving us somewhat more direct information on whether there was any
 708 misalignment between the beam and the target.

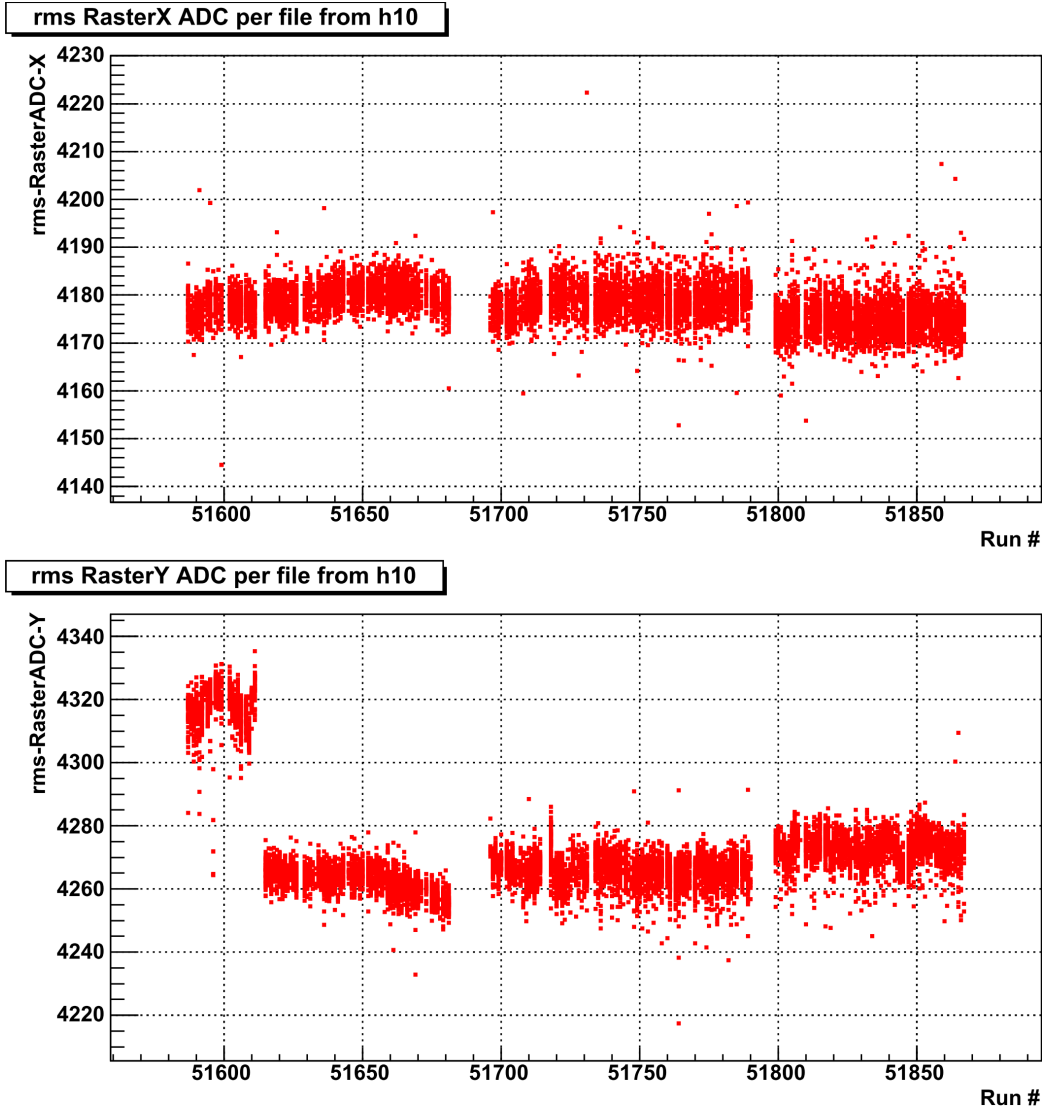


Figure 3.24: Root-mean-square of the ADC values for the raster magnet currents in the directions X and Y. The distributions show a larger raster size in the y-direction for the first group of runs, indicating that the beam may have been hitting the edges and the walls of the target or other more dense structure support materials, thus explaining the higher total yield for the corresponding runs as shown by the Fig. 3.22. This does not affect our final analysis because these off-target materials are not polarized and, hence, do not contribute to the polarization dependent count difference (ΔN) used in the final analysis.

709 Based on the studies of these quality and stability plots, the data runs
710 were divided into subgroups with each beam energy data set. In each sub-
711 group, the data showed more stability than over the whole run period for
712 the given beam energy. For example, in case of the 2.0 GeV deuteron data,
713 the runs were divided into four distinct sub groups corresponding to the four
714 separate bands as seen in the Fig. 3.22. These subgroups were later treated
715 and analyzed separately to get the corresponding normalized polarized count
716 differences (with all data runs from each subgroup combined together). After
717 the initial combination within the subgroups, they were again combined into
718 the grand total by properly considering the half-wave-plate status, and the
719 target polarization directions.

720 **3.5 Kinematic Corrections**

721 The reconstructed event vertices and associated particle 4-momenta are slightly
722 off from their true values for several reasons. First, RECSIS does not take
723 into account the fact that the beam is rastered in polarized target experi-
724 ments. Next, any imperfections and mis-alignments of detectors and other
725 components of the experimental set-up are not accounted for. Furthermore,
726 the torus field map is not known precisely. In addition, the effects of multiple-
727 scattering and particle energy losses are not considered in RECSIS. There-
728 fore, to get more accurate results from the data analysis, the data quality
729 must be improved by applying various kinematic corrections. Following is
730 the list of the corrections that were applied for the analysis:

- 731 1. Incoming (beam) energy loss correction (due to ionization)
- 732 2. Tracking corrections
- 733 3. Drift chamber dependent momentum correction
- 734 4. Outgoing energy loss correction (due to ionization after scattering)

735 **3.5.1 Incoming Energy Loss Correction**

736 The first correction listed above considers the loss of beam energy due to
737 atomic collisions before the actual nuclear scattering takes place. A good
738 estimate for this loss is 2 MeV on average [25, 26], which is subtracted from

739 the nominal beam energy. This correction is applied during the analysis
740 whenever the beam energy is involved⁴, and therefore it is not included in
741 the correction package described below.

742 3.5.2 Tracking Corrections

743 This work is mostly based on the work documented in the EG1-DVCS-TN-
744 004[28] , in which a routine or method is developed to swim the particles
745 through the field map of the target magnet to the drift chambers in order
746 to determine the particle angles and position at the target, provided the di-
747 rection cosines of the tracks at DC and the beam position from the raster
748 magnets are known. It is expected that the method improves both the angu-
749 lar resolution and the reconstructed longitudinal vertex position. The slightly
750 modified version of the corresponding C/C++ routine is used with some of
751 the constants in the routine replaced by new parameters to be determined
752 by the method of **χ^2 -square minimization** using ep-elastic events. (Since
753 this data set didn't have enough e^+e^- pairs, we didn't use them in the min-
754 imization like in the EG1DVCS.)

755 Method

756 First of all, in order to convert raster magnet ADCs into corresponding
757 beam positions x_0 and y_0 , we need conversion parameters. These param-
758 eters are determined by using a method outlined in EG1-DVCS-TN-002[29].
759 The method determines the values of the slopes and offsets that convert the
760 X- and Y-raster ADC readings to corresponding beam positions x_0 and y_0
761 in cm by minimizing the sensitivity of target vertex position (v_z) for charged
762 tracks to beam motion.

763 Next, ep-elastic events are skimmed (from all of the NH_3 target data-
764 set) using electron ID cuts for the electrons (see section 3.3) in the sixth
765 sector and proton ID consisting mainly of the time-of-flight cuts are used to
766 select protons in the third sector (opposite to the sixth one). Then missing
767 momentum cuts (less than 0.1 GeV for each of the four components P_x ,
768 P_y , P_z and E) based on 4-momentum conservation requirements (within
769 measurement uncertainties) are used to help further clean up the accidental

767
768
769
4The beam energies that we used were derived from the Hall A and Hall C Tiefenback
energies or the MDSY1c or MDSY3c energies[27]

770 coincidences. These skimmed events are saved in root files and later reused
771 for the minimization process described here.

772 The cuts used in the initial data skimming required that each of the four
773 missing components $(Px, Py, Pz, E)_{miss}$ be less than 0.1 GeV.

774 After that a correction routine involving a set of correction equations
775 with several unknown parameters are established. Then with the help of
776 TMinuit (ROOT version of Minuit), several sets of trial values are given to
777 these unknown parameters and the corresponding correction is applied to
778 the particles in the skimmed events. For each set of these trial values, a
779 specifically defined χ^2 (see below) is evaluated looping over all the skimmed
780 events and the Minuit tries to find the optimum set of these parameter values
781 for which the χ^2 is minimum. Such an optimal set of values are chosen as
782 the correct values of these parameters and is used in the eventual correction
783 routine.

784 **The correction routine**

785 The routine uses 17 constants (free parameters determined by the above
786 mentioned process of χ^2 -minimization) and the following input and output
787 variables:

- 788 • **Input variables:** $x_r, y_r, \text{cxd}, \text{cyd}, \text{xdc}, \text{ydc}, \text{zdc}, p, q$.

- 789 – x_r, y_r are x & y beam positions as returned by the raster correction
790 routine (see appendix)
791 – **cxd, cyd** are direction cosines of the track as measured at DC1
792 – **xdc, ydc, zdc** are the coordinates of the track measured at DC1
793 – p, q are the momentum and charge of the track

- 794 • **Output variables:** $\text{cxc}, \text{cyc}, \text{czc}, \text{vzc}$ (all three corrected direction
795 cosines and the corrected Z-coordinate at the vertex) .

796 The sequence of calculation steps taken (inside the routine) to arrive at the
797 output results are as follows (where, I am also using the notations of P.
798 Bosted i.e., subscripts '0' used to indicate variables at vertex, subscript 'f'
799 for those at the drift chambers (these are the tl1_ variables in the ntuples),
800 and the values of (x, y, z) are in cm):

- 801 • First of all, get ready the following constants and variables:

- 802 – $f_c = \frac{B}{50} = 0.995$ is the overall field correction
 803 * (i.e., the $B.dl$ correction factor. Our $B = 4.97T$, with B in
 804 kG f_c is 0.995)
 805 – $targsign = 1$
 806 – $\theta_f = \arccos(cz_{dc})$
 807 – $\phi_f = \text{atan2}(cy_{dc}, cx_{dc})$
- 808 • Then, θ_f is corrected (for the misalignment of the DC) as follows:
 - 809 – If it's the electron in the event,
 - 810 * $\theta_f = \theta_f + (\text{par}[0] + \text{par}[1] \times \phi_f) \frac{\cos\theta_f}{\cos\phi_f} + (\text{par}[2] + \text{par}[3] \times \phi_f) \sin\theta_f$
 - 812 – else if its the proton,
 - 813 * $\theta_f = \theta_f + (\text{par}[4] + \text{par}[5] \times \phi_f)$
 - 815 • Next, get ϕ_0 without raster corrections yet
 - 816 – $\phi_0 = \phi_f + targsign \times f_c (0.186 + \text{par}[10] + (0.045 + \text{par}[11]) \theta^2 + (0.008 + \text{par}[12]) \theta_f^3 + (0.0032 + \text{par}[13]) \theta_f^3/p^2) \frac{q}{p}$
 - 818 • Correction to polar angle from focusing effect. First, get focusing term
 819 for beam (x,y)=0.
 - 820 – $\delta\theta = f_c (0.90 \theta_f + 1.2 \theta_f^3)/(100 p^2)$
 - 821 • Displacement of beam along trajectory (x_p) and perpendicular to it
 822 (y_p)
 - 823 – $x_p = x_r \cos\phi_0 + y_r \sin\phi_0$
 - 824 – $y_p = -(x_r + \text{par}[6]) \sin\phi_0 + (y_r + \text{par}[7]) \cos\phi_0$
 - 825 • Correction to $\delta\theta$ from radial target field, which only depends on raster
 826 x and y but not vertex z. Also, no effect on peak at zero!
 - 827 – $\delta\theta = \delta\theta (1. + targsign q p (0.5/\theta_f) (y_p/0.75))$

828 • Now can get cz

829 – $\theta_0 = \theta_f + \delta\theta$

830 – $cz_c = \cos\theta_0$

831 • Now ϕ_0 again, this time including raster correction

832 – $\phi_0 = \phi_f + \text{targsign } f_c (0.186 + \text{par}[10] + (0.045 + \text{par}[11]) \theta^2 +$
833 $(0.008 + \text{par}[12]) \theta_f^3 + (0.0032 + \text{par}[13]) \theta_f^3/p^2) \frac{q}{p} (1 - (0.09 +$
834 $\text{par}[14]) \frac{0.35 - \text{par}[15]}{\theta_f} x_p)$

835 • Get cx and cy using this cz

836 – $cx_c = \sin\theta_0 \cos\phi_0$

837 – $cy_c = \sin\theta_0 \sin\phi_0$

838 • Renormalize czc

839 – $cz_c = \sqrt{1.0 - cx_c^2 - cy_c^2}$

840 • Apply target field rotation correction

841 – $cx_c = cx_c - \text{targsign } q \text{par}[8] cz_c/p$

842 – $cy_c = cy_c + \text{targsign } q \text{par}[9] cz_c/p$

843 • Renormalize again:

844 – $czc = \sqrt{1.0 - cx_c^2 - cy_c^2}$

845 – $\theta_0 = \arccos(cz_c)$

846 • Get vertex z in cm

847 – $r_{dc} = \sqrt{(x_{dc} - x_r)^2 + (y_{dc} - y_r)^2}$

848 – $Z_c = Z_{dc} - \frac{r_{dc} - (22 + \text{par}[16]) \cos\theta_0 (\tan\theta_0 - \tan\theta_f)}{\tan\theta_f}$

849 • Finally, the routine outputs (returns) the four corrected quantities

850 – cx_c, cy_c, cz_c, Z_c .

851 **Calculation of χ^2 (to be minimized)**

852 The chi-square has different components as follows:

$$853 \quad \chi^2 = \chi_{\text{Zvar}}^2(\mathbf{e}) + \chi_{\text{Zvar}}^2(\mathbf{p}) + \chi_{\text{Evar}}^2 + \chi_{\text{miss}}^2 + \chi_{\text{Ppen}}^2 + \chi_{\text{Epen}}^2 + \chi_{\text{Zpen}}^2 + \chi_{\Delta E}^2$$

854 where,

- 855 • $\chi_{\text{Zvar}}^2(\mathbf{e})$ and $\chi_{\text{Zvar}}^2(\mathbf{p})$ are Z-variance contributions from electron and
856 proton candidates in the ep-elastic events and are calculated as $\chi_{\text{Zvar}}^2 =$
857 $\frac{1}{N_{ep}-1} \left(\sum Z_c^2 - \frac{(\sum Z_c)^2}{N_{ep}} \right) / (0.05)^2$ separately for the electrons and protons.
858 (Here, Z_c is the corrected Z of vertex and N_{ep} is the number ep-elastic
859 events used in the minimization)
- 860 • $\chi_{\text{Evar}}^2 = \frac{1}{N_{ep}-1} \left(\sum E_b^2 - \frac{(\sum E_b)^2}{N_{ep}} \right) / (0.005)^2$ is E_b -variance contribution.
861 (Here, $E_b = M_p \left(\frac{1}{\tan(\theta_p)\tan(\theta_e/2)} - 1 \right)$ is the beam energy calculated after
862 the angles are corrected by the correction routine.)
- 863 • $\chi_{\text{miss}}^2 = 100 \times \left(\frac{\sum p_x^2(\text{miss}) + \sum p_y^2(\text{miss})}{0.02^2} + \frac{\sum p_z^2(\text{miss}) + \sum E^2(\text{miss})}{0.05^2} \right)$ is missing
864 four-momentum contribution. (Here, 100 is an arbitrary number to
865 make the weight of this contribution comparable to others.)
- 866 • $\chi_{\text{Ppen}}^2 = \sum_{i=0}^{16} \frac{(par[i] - iPar[i])^2}{0.01^2}$ is the contribution due to runaway penalty
867 on free parameters of the minimization. (Here, par[i] & iPar[i] are the
868 current and initial values of the 'i'th parameter. In the first iteration,
869 initial values were set to either zeros or the corresponding values as
870 determined for EG1-DVCS by P. Bosted. In later iterations, they were
871 set to the values determined from the previous iteration of the mini-
872 mization.)
- 873 • $\chi_{\text{Zpen}}^2 = \sum_{e,p} \left(\sum_{N_{ep}} \frac{(Z_c - (-100.93))^2}{0.05^2} \right)$ is a penalty term when Z_c runs away
874 from the known/nominal target center (-100.93 cm)
- 875 • $\chi_{\text{Epen}}^2 = \sum_{i=2}^4 \left(\frac{\sum_{N_{ep}} E_b}{N_{ep}} - E_0 \right)^2 / (0.005)^2$ is a penalty term to constrain E_b
876 running away from the nominal values E_0 of beam energy.

- 877 • $\chi^2_{\Delta E} = \left(\sum_{i=2}^4 \frac{\sum N_{ep}}{N_{ep}} (E_b - E_0)^2 \right) / (0.005)^2$ is another penalty term to constrain
 878 E_b running away from the nominal values E_0 of beam energy.

879 **Minimization**

880 TMinuit is used to minimize the value of χ^2 as calculated above and, thereby,
 881 determine the values of the free parameters used in the correction routine.
 882 The minimization was done in such a way that the parameters were deter-
 883 mined step by step - first deciding the first six parameters (keeping others
 884 fixed to initial values), then next two, then next two, then next four, then
 885 next 2 and finally the last one respectively.

886 **Tracking Correction Results**

887 With the method of χ^2 -minimization described above, the following set of
 888 values were determined for the 17 parameters from par[0] through par[16]
 889 respectively:

890 -0.00165789, -0.00131314, -0.00643021, -0.00721441, -0.00775272, 0.00483673,
 891 0.063387, -0.0615822, 0.00133127, 0.000839944, 0.0210091, -0.0363265, 0.00335536,
 892 0.00104193, 2.51519, -0.0313527, -1.29325

893 As a result of the corrections with these newly determined parameter
 894 values, various quantities before and after the corrections looked as shown in
 895 the following figure:

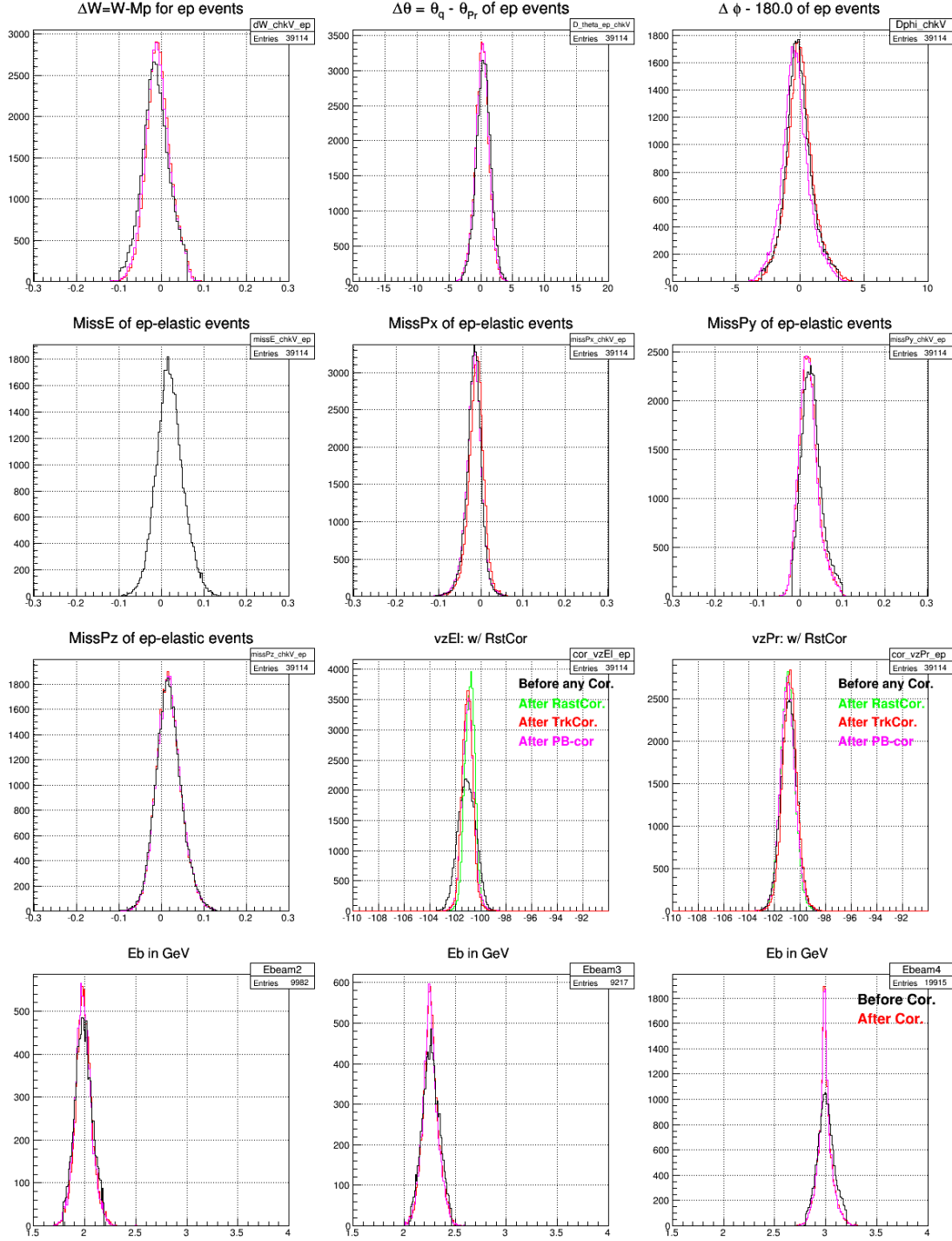


Figure 3.25: Comparing various quantities before and after the tracking corrections which affects only the angles (and ~~not~~ the magnitude 'p') of the momentum.

896 **3.5.3 Momentum Correction**

897 Different DC related factors contribute to the biggest part of the system-
898 atic deviations of particle momenta as reconstructed by RECSIS. The drift
899 chambers could be misaligned relative to their nominal positions or the sur-
900 vey results that is used by RECSIS could be inaccurate or out-of-date. The
901 effects of physical deformations (due to thermal and stress distortions) of
902 the chamber including wire-sag, incorrect wire positions may not have been
903 incorporated properly. The torus field map used by the reconstruction soft-
904 ware may not have been accurate and complete enough [30]. Effects on angles
905 θ and ϕ due to these contributions are already factored in the tracking cor-
906 rection described earlier. However, a separate method is developed to correct
907 for the effect on the magnitude p of the momentum. This p -correction meth-
908 ods picks up and builds on some of the ideas outlined in the CLAS-NOTE
909 2003-005 [30].

910 **Procedure to determine the first 11 parameters**

911 The procedure involved dividing the covered kinematic space into a number
912 of bins, finding in them the magnitude of shifts of the inclusive elastic peaks
913 w.r.t. the expected position and use that to fit to a function to get an
914 analytical expression for the correction. The following angular bins were
915 used:

- 916 • Six θ_{dc1} bins: (0,8),(8,10),(10,12),(12,15),(15,20),(20,30) degrees
917 • Five ϕ_{dc1} bins: (-10,-6),(-6,-2), (-2,2), (2,6), (6,10) degrees

918 where the angles used are the ones measured at the first drift chamber and
919 ϕ_{dc1} is measured w.r.t the sector mid-plane (thus the maximum range allowed
920 is (-30.0,30.0)).

$$E'_{elastic} = \frac{E_{beam}}{1 + \frac{2E_{beam}}{M_p} \sin^2(\theta_e/2)} \quad (3.4)$$

921 In each of these kinematic bins, the quantity $\Delta E = E'_{elastic} - p$ (see Eq.
922 3.4) is histogrammed for both NH₃ and ¹²C data separately. Next, the carbon
923 histogram is cross-normalized with the ammonia histogram (by comparing
924 the two in the region left to the quasi-elastic peak) and subtracted from the

925 latter one to remove the nuclear background. The difference gives histograms
 926 for the elastic events (as shown by the dashed green histogram in Fig. 3.26).
 927 A Gaussian fit to the extracted elastic histogram gives the position and width
 928 of the distribution. The offset or shift of average position of the peak with
 929 respect to the expected $\Delta E = 0$ gives us the needed correction on energy
 930 $E \approx p$ for the electron. This process is repeated for all of the bins listed
 931 above and the corresponding ΔE offsets or the corrections are determined
 932 for each of them. Additionally, ΔE distributions using ^{15}N nuclear mass
 933 in calculating $E'_{elastic}$ are also made and off-sets in the corresponding elastic
 934 peaks are also recorded whenever possible (particularly from the lower θ bins
 935 from low beam energy data where the nuclear-elastic and quasi-elastic peaks
 936 are well separated). Finally, these values of corrections for different average
 937 values of θ_{dc1} and ϕ_{dc1} are fit to Eq. 3.5 (which is based on similar work done
 938 for EG1b analysis[20]) and using the method of χ^2 -minimization in order to
 939 determine the values of the 11 fit parameters.

$$\frac{\Delta p}{p} = Pcorr1 + Pcorr2 + PatchCorr \quad (3.5)$$

940 where, $\frac{\Delta p}{p}$ is the ratio of the correction (Δp) to the magnitude (p) of the
 941 momentum and

$$Pcorr1 = \left((E + F\phi) \frac{\cos\theta}{\sin\phi} + (G + H\phi) \sin\theta \right) \frac{p}{qB_{torus}} \quad (3.6)$$

$$Pcorr2 = (J\cos\theta + K\sin\theta) + (M\cos\theta + N\sin\theta)\phi \quad (3.7)$$

$$PatchCorr = 0.02 \left(P + (Q + R \frac{\phi_{deg}}{30^\circ}) (\frac{10^\circ}{\theta_{deg}})^3 \right) \quad (3.8)$$

942 The quantity B_{tor} stands for $\int B_\perp dl$ along the track length multiplied by
 943 the speed of light in the units of m/ns ($c = 0.29979$ m/ns) and is given by

$$B_{tor} = 0.76 \frac{I_{tor} \sin^2(4\theta)}{3375\theta/rad} \quad \text{for } \theta < \frac{\pi}{8} \quad (3.9)$$

$$B_{tor} = 0.76 \frac{I_{tor}}{3375\theta/rad} \quad \text{for } \theta > \frac{\pi}{8} \quad (3.10)$$

944 In all these equations, sector number, θ , ϕ , θ_{deg} , and ϕ_{deg} come from the
 945 angle information measured at DC1. The direction cosine variables tl1_cx,
 946 tl1_cy, tl1_cz (from pass1 ntuple) are used to derive these quantities. C++
 947 standard functions `acos()` and `atan2()` are used to evaluate θ , ϕ (w.r.t the
 948 sector mid plane).

949 These total of eleven unknown parameters were determined by fitting
 950 above mentioned momentum offsets (in combination with ionization energy
 951 loss correction for electrons (see Sec.3.5.4 below)) to the correction function
 952 given by the Eq. 3.5.

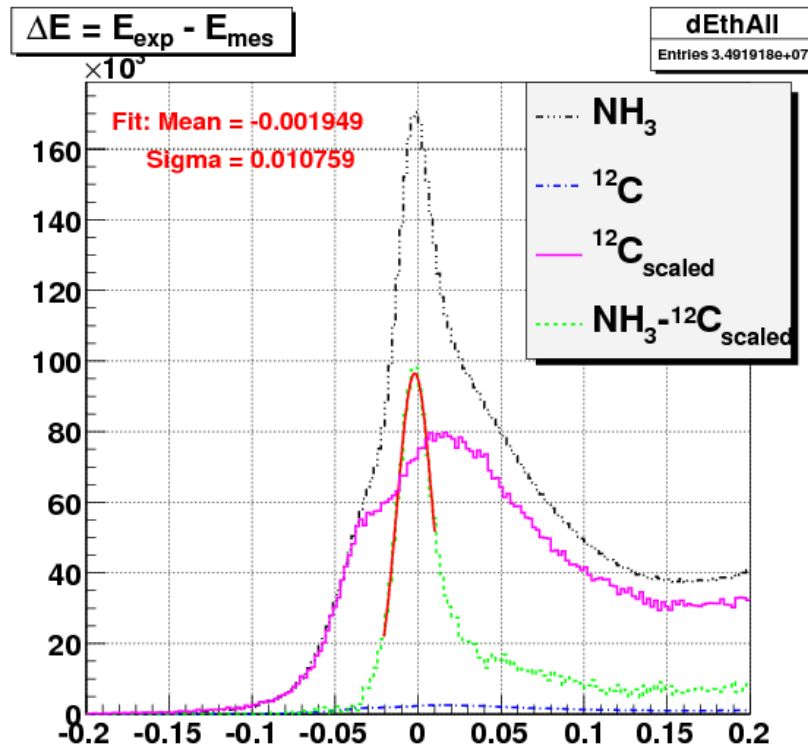


Figure 3.26: Plots showing background removal from the ΔE counts from NH_3 (shown by “ NH_3 ” line) data (by subtracting cross-normalized counts from ^{12}C data (shown by “ $^{12}\text{C}_{\text{scaled}}$ ” line)) to separate the elastic peak (shown by “ $\text{NH}_3 - ^{12}\text{C}_{\text{scaled}}$ ” line) in one of the kinematic bins, thereby getting the momentum offset for that bin. The ^{12}C data is used to account for the nuclear elastic background from ^{15}N nucleii in the ammonia target. It would have been best to have data from ^{15}N target itself but due to technical difficulties that was not possible and, therefore, ^{12}C target was chosen as the closest possible approximation of ^{15}N target.

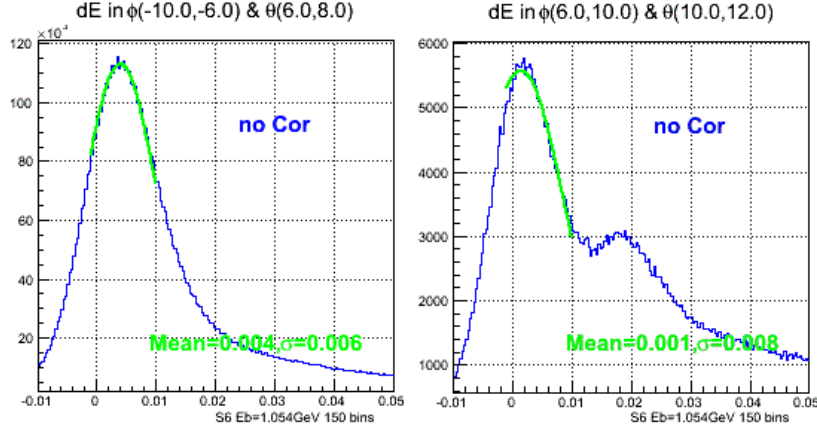


Figure 3.27: Nuclear elastic peaks from ^{15}N target and the Gaussian fits in two of many kinematic bins as seen in $\Delta E = E'_{\text{elastic}} - p$ distributions from NH₃ data before the momentum corrections. In this case E'_{elastic} is evaluated using known mass of ^{15}N in Eq. 3.4. In the second plot, the proton elastic peak is also visible. Ideally, after all the corrections, the nuclear elastic peak is expected to be centered at zero. But, as is obvious from these figures, these peaks show offsets. These offsets (given by the mean values of the Gaussian fits) are collected from those bins in which the nuclear elastic peaks are very well separated (particularly the first few angular bins) and used in the χ^2 -minimization along with all the offsets of elastic peaks (see Fig. 3.26)

953 3.5.4 Outgoing Ionization Loss Correction

954 In addition to the corrections described above, the energy (E) of each of the
 955 particles is corrected for the outgoing ionization loss by adding an estimation
 956 of ionization loss as follows: $E_{\text{cor}} = E + \Delta E$ with $\Delta E = \frac{dE}{dX}\tau$ where the factor
 957 τ is the total effective mass thickness traversed by the particle and

$$dE/dX \approx 2.8 \text{ MeV}/(\text{g cm}^{-2}) \quad \text{for electrons} \quad (3.11a)$$

958 and, for hadrons [31]

$$dE/dX \approx 0.307 \times \frac{0.5}{\beta^2} \left(\ln \left(2.0 \times 511.0 \frac{\beta^2 \gamma^2}{0.090} \right) - \beta^2 \right) \text{ MeV} \quad (3.11b)$$

959 which is an approximation of the Bethe-Block formula [31]:

$$-\frac{1}{\rho} \frac{dE}{dx} = 4\pi N_a r_e^2 m_e c^2 \frac{Z}{A} \frac{1}{\beta^2} \left(\ln \left(\frac{2m_e c^2 \gamma^2 \beta^2}{I} \right) - \beta^2 \right) \quad (3.12)$$

960 The total effective mass thickness τ (in cm) is calculated as follows:

961 • $\tau = \tau_{||}/\cos\theta$ if $\theta \leq \pi/4$

962 • $\tau = \tau_{||}/\cos(\pi/4)$ if $\theta > \pi/4$

963 where $\tau_{||}$ is calculated as:

964 • $\tau_{||} = \Delta z \times 0.6 + 0.4$ if $\Delta z > 0.0$ and $\Delta z < 1.0$

965 • $\tau_{||} = 0.6 + 0.4$ if $\Delta z \geq 1.0$

966 • $\tau_{||} = 0.4$ if $\Delta z \leq 0.0$

967 with $\Delta z = z_{target_center} - z_{ave} + L_{target}/2 = (-101.0 \text{ cm} - z_{ave} + 0.5) \text{ cm}$ being
968 the physical distance (along the target length) traveled by the particle
969 through the polarized target material (e.g. the EG4 ND₃ target has length
970 1.0 cm and is positioned at $z = -101.0 \text{ cm}$). The factor 0.6 is the effective
971 mass thickness of ND₃ (density of ND₃ ($\sim 1 \text{ g/cm}^3$) multiplied by the pack-
972 ing fraction which is roughly 0.6 [32], whereas 0.4 is the sum of the mass
973 thicknesses of He (~ 0.3) and that of window foils (~ 0.1) [20].

974 Using the ionization loss corrected energy and the rest mass of the parti-
975 cle, momentum is recalculated as $p_{cor} = \sqrt{E_{cor}^2 - m^2}$ (where m is the mass
976 of the particle). Finally, this new p is used along with the previously cor-
977 rected angles to evaluate the three cartesian components p_x , p_y and p_z of the
978 momentum as follows:

$$\begin{aligned} p_x &= p \sin \theta \cos \phi \\ p_y &= p \sin \theta \sin \phi \\ p_z &= p \cos \theta \end{aligned} \tag{3.13}$$

979

980 3.6 Cerenkov Counter (CC) Efficiency

981 In the EG4 experiment, the Cherenkov Counter (CC) signal plays a major
982 part in forming the event trigger for the data-acquisition system (DAQ). As
983 stated earlier (see 2.1), for the purpose of achieving low Q^2 measurements
984 with high detector efficiency⁵, a new dedicated CC was designed and placed

⁵High detection efficiency is crucial for achieving smaller systematic uncertainties in the extracted physics quantities.

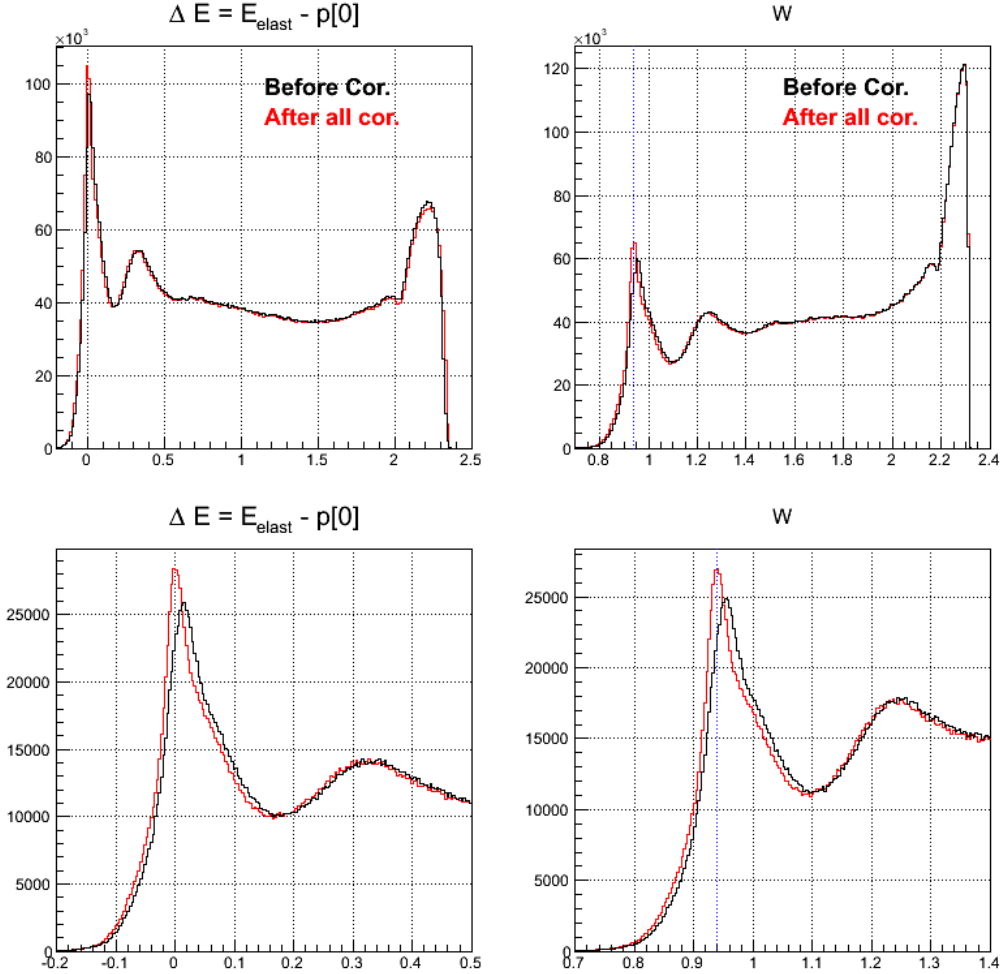


Figure 3.28: Effects of kinematic corrections on inclusive events from 3 GeV NH₃ data. Here, distributions of ΔE and W are shown in two different ranges. The upper ones show the full range distributions, whereas the lower two show the distributions near the quasi-elastic peak. The distributions before the corrections are shown by **black continuous** lines and the ones after the corrections are shown by the **red** lines. Here, E_{elast} is the calculated or expected energy of the scattered electron assuming it was scattered off elastically, whereas, $p[0]$ is the momentum as measured by CLAS. From these plots it is evident that the momentum correction works as expected because the peak of ΔE is narrower and better centered at zero after the correction.

985 in the sixth sector. Even though the new CC was designed to have a very
986 high and uniform detection efficiency, some variation occurs over the covered
987 kinematic range and therefore the knowledge of the detector efficiency as a
988 function of the kinematics is required by our method of absolute cross-section
989 difference. Therefore, a study was done to determine the CC efficiency as
990 follows.

991 **3.6.1 Procedure**

992 The efficiency for some specific kinematic bin depends on the average num-
993 ber of photoelectrons produced by electrons in that bin which, in turn, is
994 determined by the hit location on the Cerenkov PMT-projected plane as
995 well as the angle with which the electron hits (or intersects) the plane. In
996 the following, we describe how we determined the efficiency as a function of
997 kinematic variables.

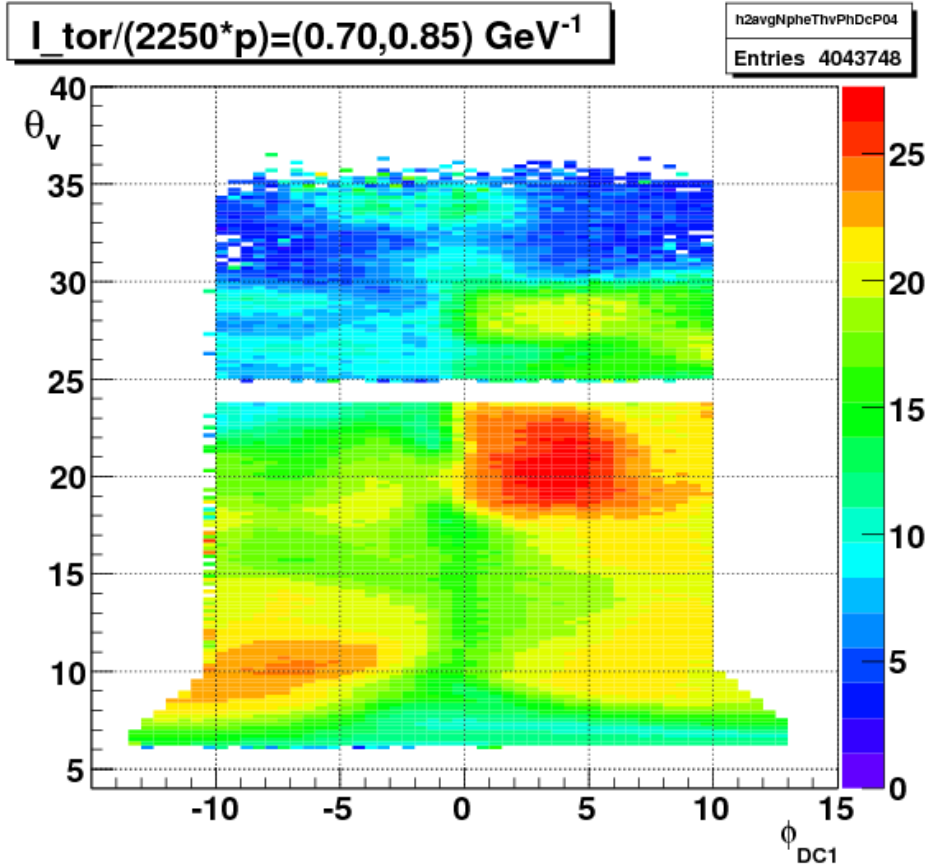


Figure 3.29: Average photoelectron number (color-coded) produced in the 6th sector CC as a function of θ_{vtx} and ϕ_{DC1} in the second bin of the variable $ip = (I_{tor}/2250)/p$ (from the 2.3 GeV NH₃ data).

- 998 1. First, we define a torus-current normalized inverse-momentum variable
- 999 $ip = (I_{tor}/2250)/p$ (see above), and divide the whole kinematic space
- 1000 into 12 bins in “ip” as follows: (0.3, 0.4, 0.5, 0.6, 0.7, 0.85, 1.0, 1.25,
- 1001 1.5, 1.75, 2.0, 2.25, 2.53). (For example, a 0.5 GeV electron during a
- 1002 2 GeV run, which used 2250 A for torus current, would have $ip = 2.0$
- 1003 GeV^{-1})
- 1004 2. Next, for each bin in “ip”, a 2D map of the average number of photoelec-
- 1005 trons is produced in a kinematic space defined by θ_{vtx} (scattering angle
- 1006 measured at the event vertex) and ϕ_{DC1} (azimuthal angle as measured

1007 at DC1). For this step, some data from NH₃ production runs⁶ are used
1008 with the standard electron selection cuts. One of these average-nphe
1009 maps is shown in the Fig. 3.29.

- 1010 3. Next, using the “EC-only-trigger” data runs, good electron candidates
1011 are selected using the same cuts as before but without any CC-related
1012 cuts. For each of the selected electrons, the expected number of photo-
1013 electrons in the CC is determined in a look-up from the above average
1014 N_{ph}-maps based on its momentum and angles. This expected N_{ph} is
1015 then histogrammed in two ways - one histogram for those electrons
1016 which either didn’t trigger CC or didn’t pass all of the CC related
1017 cuts and another histogram for all electrons. The ratio of these two
1018 histograms (shown in the top-right and top-left panels of Fig. 3.30 re-
1019 spectively) gives us the inefficiency of the CC-detector as a function of
1020 N_{ph} (as shown by the bottom two panels of the same figure). (Errors
1021 in the inefficiencies have not been drawn (for the purpose of cleaning)
1022 in the figures but they were calculated using the fact that the error in
1023 a ratio N2/N1 is $\sqrt{N2(1 - N2/N1)/N1}$).
1024
- 1025 4. The ideally expected CC intrinsic inefficiency is given by the Poisson
1026 distribution, since we require more than 2 photoelectrons, the theoret-
1027 ical prediction for the inefficiency is actually $(1 + N_{ph} + 1/2 N_{ph}^2) * \exp(-N_{ph})$. However, we found empirically that if we calculate N_{ph} only with
1028 electrons that exceed the threshold of 2.5, then we find that the func-
1029 tional form is pretty close to the form $y = p_0 + p_1 \cdot \exp(-p_2 x)$, where
1030 x represents $\langle N_{ph} \rangle$, and y represents the inefficiency. This form was
1031 used to fit with the above measured inefficiency and the result of the
1032 fit is shown in Fig. 3.30. We find that the inefficiency agrees very well
1033 with the expectation at low nphe, but remains at a very small constant
1034 value of around 0.01 (we call it the “constant background”) at higher
1035 nphe.

⁶This method relies on the use of two different sets of data. One is the regular NH₃ target data and another is the “EC-only” data runs which were collected without using CC in the trigger. Since the latter type of data were collected with NH₃ as target, to be consistent, NH₃ production data was chosen rather than the ND₃ ones to make the N_{ph}-maps.

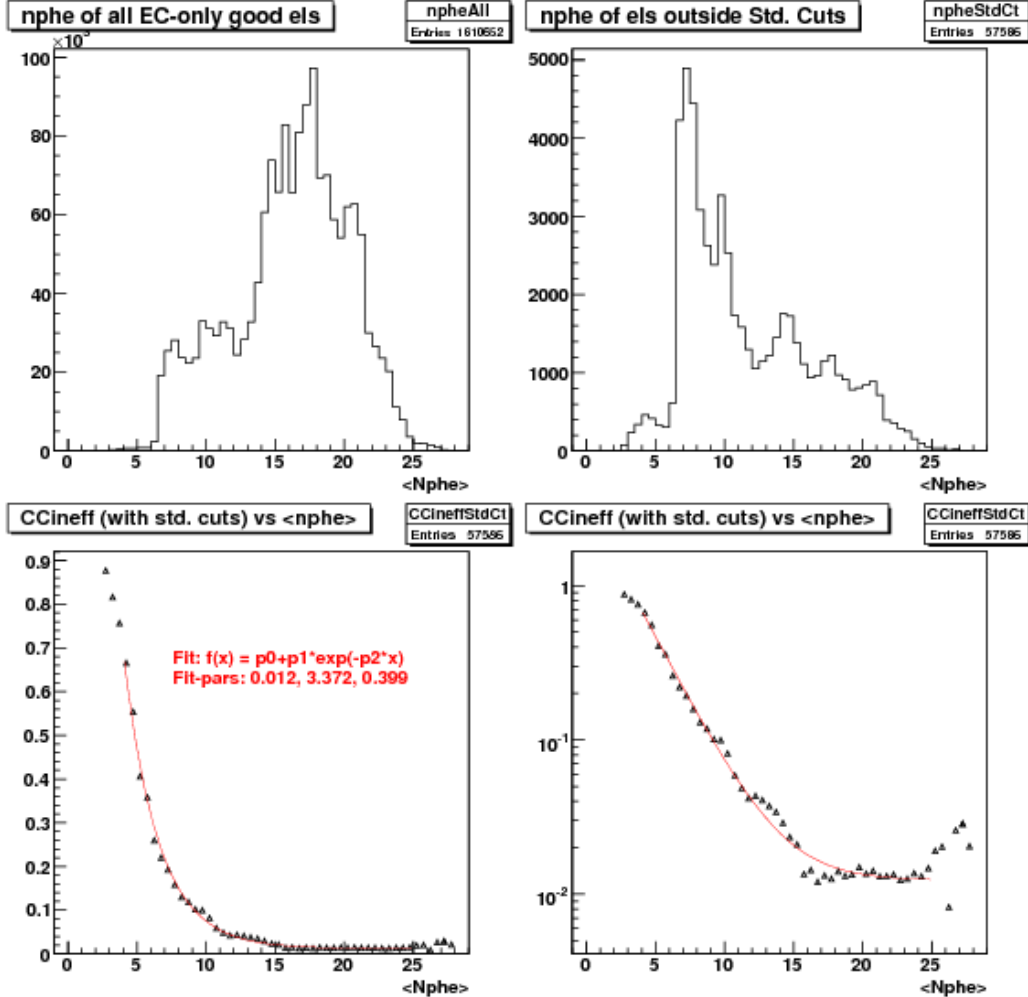


Figure 3.30: EC detected good electrons (for all momenta) as a function of $\langle N_{ph} \rangle$ (top left). Similar distribution (top right) for those good electrons that were detected by the EC but were rejected by the standard set of event selection cuts which includes CC-dependent cuts. By dividing the latter with the former, one gets the calculated CC inefficiency. The bottom two plots show the inefficiency distribution and a fit (red continuous line) in both linear (in third panel) and logarithmic (fourth panel) scales. Looking at the first plot, it can be seen that most electrons are above $N_{ph} = 15$ where the inefficiency is at most 1-2 %.

- 1036 5. Finally we use the inefficiency fit just developed to evaluate the corre-
 1037 sponding efficiencies and transform the 2D map of N_{ph} into the corre-

1038 sponding efficiency maps (see Fig. 3.31 for such a map in one momen-
 1039 tum bin.). These maps are later used to apply the efficiency correction
 1040 on an event by event basis in the simulation.

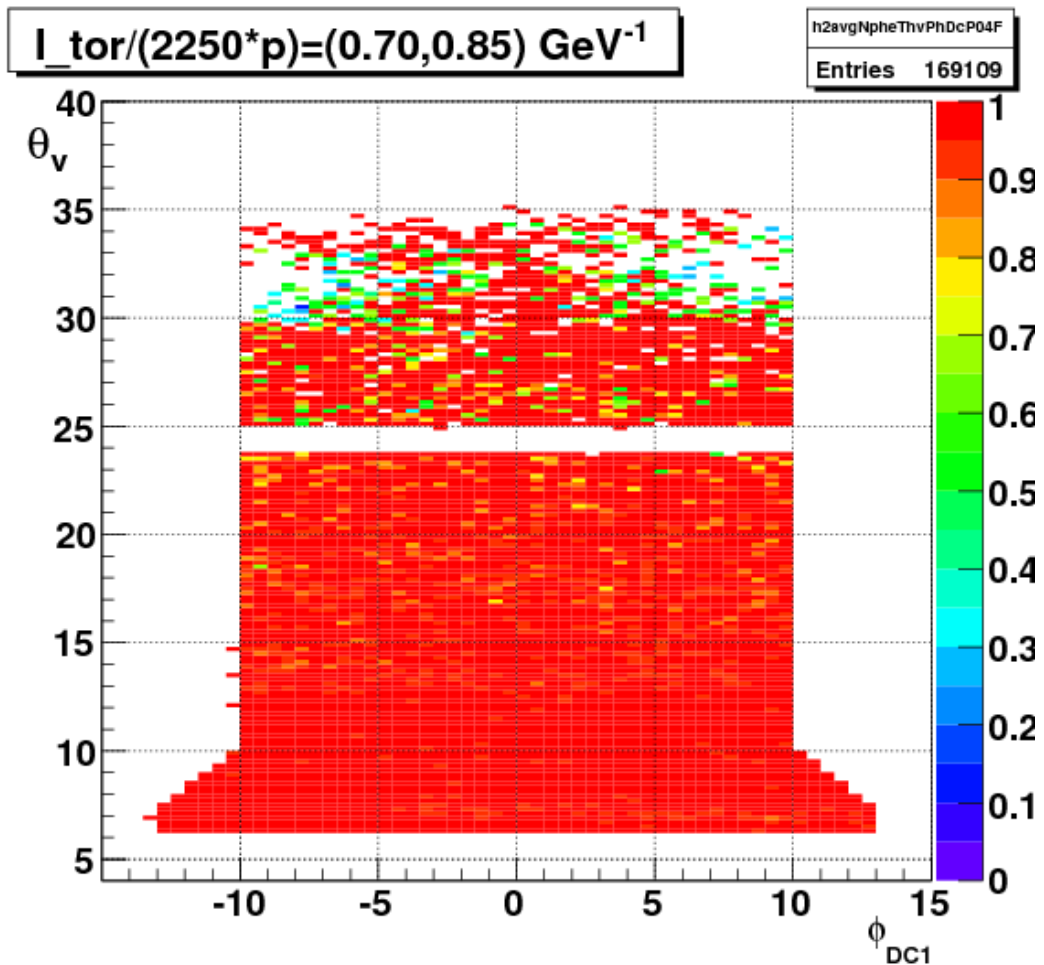


Figure 3.31: CC-efficiency in a momentum bin .

1041 From this study, we see that the CC is very efficient in most of the
 1042 kinematic region (see Fig. 3.31). Once, the CC-(in)efficiency was estimated,
 1043 we use the calculated CC efficiency to multiply our simulation (i.e., for each
 1044 simulated event, we look up the CC efficiency and weigh the event with it).

3.7 Pion Contamination Corrections

One of the two major sources of backgrounds in the measured EG4 electron rates comes from misidentified negatively charged pions (π^-) that produce similar set of signals as electrons in various detector components and thus pass the electron ID cuts. In the EG4 experiment, signals from the electromagnetic calorimeter (EC) and Cherenkov counter (CC) are used to identify electrons from pions, but even with stringent conditions on these signals, some of the pions get misidentified as electrons. To avoid limiting statistics too much in order to minimize the final statistical error in a given kinematic bin, a trade-off in purity versus efficiency (statistics) is made by quantifying the amount of this kind of contamination.

3.7.1 Method

First, the whole kinematic space covered by EG4 is divided into 90 two-dimensional bins - 9 in p and 10 in θ ⁷.

For each kinematic bin, a histogram of the number of photo-electrons (variable ' N_{phe} ' in the data ntuple) produced by the electron candidates (selected using the standard particle selection conditions (cuts) except that no cut on ' N_{phe} ' is included is made (see Fig. ??). Likewise, using a very stringent set of cuts, a similar histogram is made for the cleanest possible sample of pion candidates in the same kinematic bin.

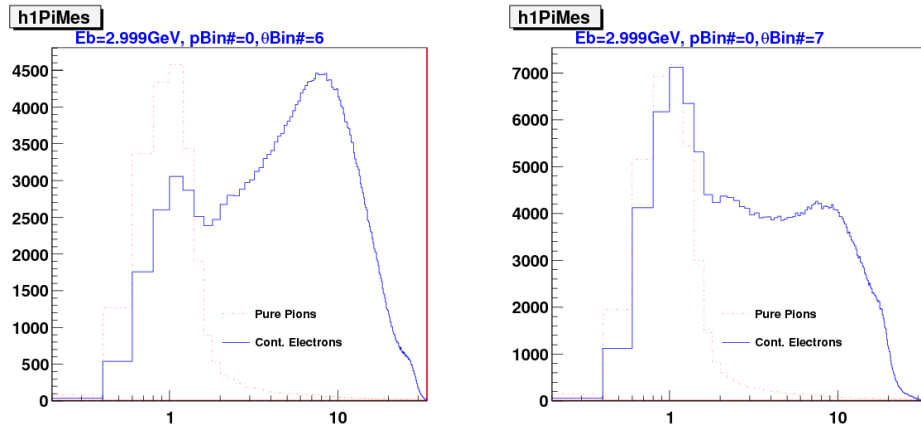
- **Estimating the contamination in each bin:** A 7th order polynomial is fit to the N_{phe} histogram for electrons in the N_{phe} range extending from $N_{phe} = 1.8$ to $N_{phe}=10$. The fit is then extrapolated down to $N_{phe} = 0$ (see Fig. ??). Subtracting the extrapolated fit from the impure electron distribution results in the extraction of the contaminating pion peak⁸. Rescaling the pure pion sample to the extracted

⁷For 2 GeV or higher beam energy data sets, the p -bin boundaries are chosen as (0.30, 0.60, 0.90, 1.20, 1.50, 1.80, 2.20, 2.60, 3.00) and (0.30, 0.45, 0.60, 0.75, 0.9, 1.1, 1.4) for others. And, for θ , the boundaries are (5.0, 6.0, 7.0, 8.0, 9.0, 10.0, 12.0, 15.0, 19.0, 25, 49). The choice of the binning was rather arbitrary. Nevertheless higher statistics region was divided into relatively finer bins (event population peaks around $\theta= 10$ degrees).

⁸Beyond $N_{phe} = 1.8$, the electron sample is nearly pure except for a tiny fraction due to the pion tail, so any function that fits that section of the N_{phe} -distribution is supposed to represent the pure electron distribution. In order to simplify the situation, we chose to fit only from 1.8 to 7.0 rather than covering the full range beyond 7.0.

peak gives us the distribution of the actual pion contamination over
 the complete range of N_{phe} . Finally, the counts corresponding to this
 rescaled pure sample in the region above the standard cut $N_{phe} > 2.5$
 is calculated. Then the ratio of this count to the impure electron count
 in the same standard N_{phe} range gives the measured contamination for
 the bin.

- The contaminations thus evaluated for different momentum bins belonging to a particular θ -bin are then plotted against the corresponding momenta. Then, this is fit to an exponential function.
- The parameters par1 and par2 of the exponential fit performed in different theta bins are next graphed together to see the presumed linear dependence.
- Finally, a global fit is performed on all the contaminations in different θ - and p - bins (not on the fit parameters). The fit parameters from the earlier two fits only give us a hint to the type of the dependence, thus allowing us decide the form of the fit function.



(a) For the first in momentum and seventh in θ bin.
 (b) For the first in momentum and eighth in θ bin.

Figure 3.32: Number of photo-electrons produced in CC by clean pion and contaminated electron samples (3.0 GeV data)

1087 From the study, it is found that the typically pion contamination is less
1088 than 1 %.

1089 **3.8 e^+e^- -Pair Symmetric Contamination Cor-** 1090 **rections**

1091 The next major source of background is the secondary electrons from various
1092 e^+e^- pair production processes. When an electron originating from such a
1093 pair passes through the detector, the detector has no way to distinguish it
1094 from the electrons that actually scattered off the target. Therefore, the detec-
1095 tor simply accepts it as a true scattered electron candidate, thus producing
1096 a contamination that has to be estimated and corrected for. The first such
1097 source is the wide-angle e^+e^- pair production from bremsstrahlung photons
1098 generated in the target. The other major source is hadron decay such as
1099 the Dalitz decay ($\pi^0 \rightarrow e^+e^-\gamma$), $\pi^0 \rightarrow \gamma\gamma$ and then conversion of these photons
1100 into e^+e^- pairs. Likewise, the pseudoscalar particle η , and the vector mesons
1101 ρ , ω , ϕ also decay to e^+e^- , but they are not major contributors because of
1102 their very small decay probabilities as well as the small population compared
1103 to the π^0 and photons. Of all these sources, the biggest contributor to the
1104 secondary electrons is the $\pi^0 \rightarrow \gamma\gamma$ with γ conversion to e^+e^- [33].

1105 The amount of contamination from this type of process can be estimated
1106 by monitoring the amount of positrons that were recorded under the same
1107 experimental and kinematic conditions. Because of the symmetry in the
1108 amount of electrons and positrons produced from these sources, the positron
1109 to electron ratio gives us the amount of the pair-symmetric contamination.
1110 However, due to the presence of the strong magnetic field inside the detector
1111 and the fact that the positrons have opposite charges, their detector accep-
1112 tance would be different in a given setting. By reversing the magnetic field
1113 while keeping everything else the same, it is possible to estimate the con-
1114 tamination. For some of the beam energies used for the NH₃ data of the
1115 EG4 experiment, some data were collected with identical experimental set-
1116 ting but with the torus field reversed. The data from those runs were used
1117 to estimate the amount of positrons in somewhat the same fashion as pion
1118 contamination. For example, Fig. 3.34 shows one estimate (both data points
1119 and the fit) of the contamination in EG4 compared with those determined
1120 for the EG1b experiment [20].

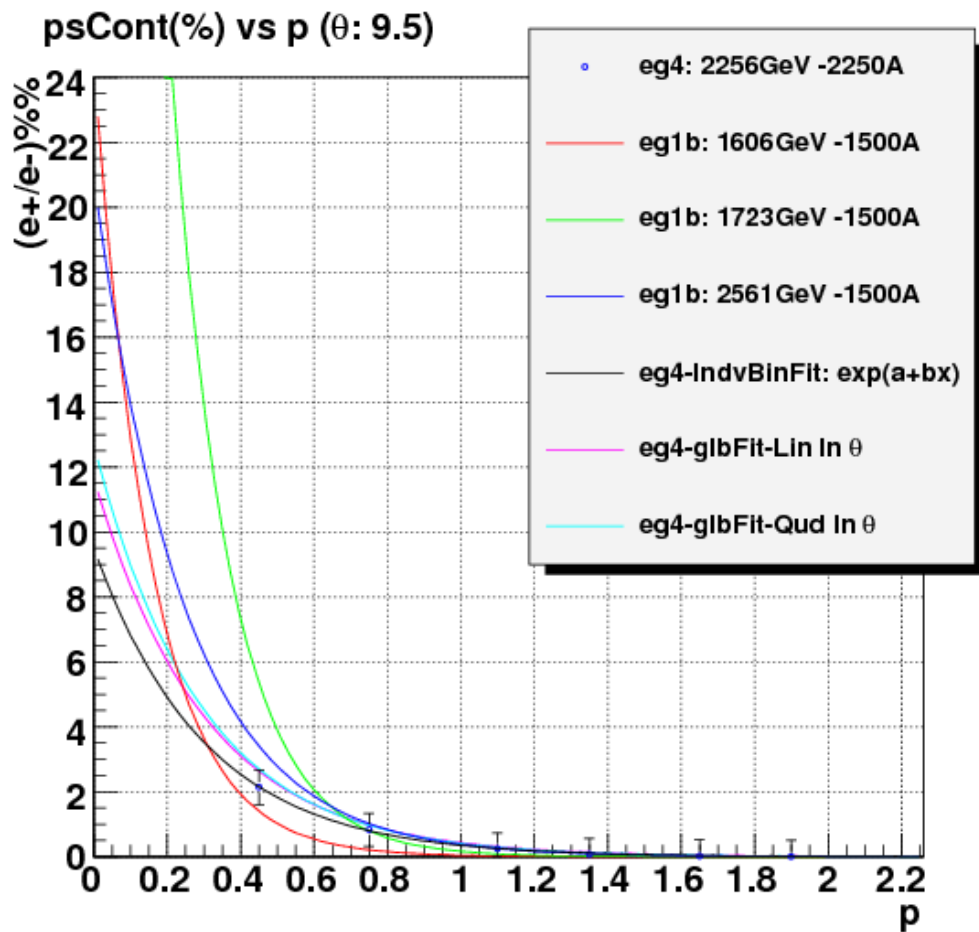


Figure 3.34: Pair-symmetric contamination Fits (%) as a function of electron momentum.

1121 For this analysis, both the pion and e^+e^- pair symmetric contaminations
 1122 are small enough to be ignored. This leads to only a slight increase in the
 1123 systematic error in the final physics results.

₁₁₂₄ **3.9 Study of NH₃ Contamination of EG4 ND₃**
₁₁₂₅ **Target**

₁₁₂₆ In equation (3.1), it is assumed that the ammonia target is 100% pure i.e.
₁₁₂₇ composed of only ¹⁵ND₃ molecules and that the contribution from the
₁₁₂₈ slightly polarized nitrogen is negligible. But, in practice, the standard ND₃
₁₁₂₉ sample is not a 100% pure material. Rather, it contains one or two percent
₁₁₃₀ of ¹⁴ND₃, ¹⁵NH₃ [34], and some traces of other isotopic species of ammonia.
₁₁₃₁ It was reported by the EG1-DVCS experiment at Jlab [35][36] that a higher
₁₁₃₂ than usual amount of NH₃ (about 10%) was observed in the ND₃ target,
₁₁₃₃ indicating that an inadvertent mix-up of NH₃ and ND₃ materials could have
₁₁₃₄ happened during the experimental run. Wondering if the EG4 experiment
₁₁₃₅ had a similar incident, we decided to investigate and estimate the amount of
₁₁₃₆ NH₃ contamination of our ND₃ target by looking at the data from the ND₃
₁₁₃₇ run period of the experiment as described below.

₁₁₃₈ **3.9.1 Procedure**

₁₁₃₉ The method involves using ep elastic (or quasi-elastic in the case of non-
₁₁₄₀ proton target) events and comparing the width in some quantity that reflects
₁₁₄₁ the correlation between the scattered electron (e) and the recoiling proton (p)
₁₁₄₂ due to the kinematic constraints of such events. The most suitable correlation
₁₁₄₃ is the one between the polar angles of the electron and the proton. That is
₁₁₄₄ because of the better angular resolution in CLAS than that for momentum,
₁₁₄₅ and also due to the fact that polar angle (θ) resolution is much better than
₁₁₄₆ that of the azimuthal angle (ϕ) because of the rotational effect (on ϕ) of the
₁₁₄₇ polarized target field as well as the drift chamber resolutions [35].

The θ -correlation can be studied mainly in two ways. The first way is to reconstruct and histogram the beam energy using the measured polar angles and the known target mass and then compare the histogram from the ND₃ target run with that from a pure NH₃ target run. The other equivalent way is to predict the proton polar angles (using the measured electron angles, known target mass and the beam energy) and then histogram the deviation of the measured proton angles from the expected values. We chose to use a slightly modified version of the latter approach in which we histogram the

following quantity⁹:

$$\Delta = p_p \cdot (\sin\theta_q - \sin\theta_p) \quad (3.14)$$

where p_p is the measured proton momentum, θ_p is the measured polar angle of the proton, and θ_q is the expected polar angle of the recoiling proton (which is also the angle of the exchanged virtual photon (q)) given by:

$$\theta_q = \tan^{-1} \left(\frac{M_p}{\tan(\theta/2) \cdot (E_{beam} + M_p)} \right) \quad (3.15)$$

The method exploits the fact that the width of the quantity Δ from data with deuteron target decreases because the Fermi motion of the protons in the deuteron nuclei gives a spread of the order of 50 MeV in transverse momentum, and for longitudinal particle momenta of order of a few GeV, we obtain a polar angle spread about 20 mr, which is much larger than the intrinsic CLAS resolution of about 2 mr.

3.9.2 Event Selection

First, for each data set (corresponding either to NH₃, ND₃ or ¹²C runs), using standard electron and proton identification cuts , events with a well reconstructed scattered electron and a similarly well reconstructed candidate for proton are selected. We accept only events each of which have one electron, one proton and at most one neutral particle candidate (expected to be a neutron coming off from the deuteron target break-up). If the event is of the above type, the following additional cuts are applied to make sure it is elastic or quasi-elastic event:

- $E_X < 0.15$ GeV with $E_X = M_p + E_e - E_{e'} - E_p = M_p + \nu - E_p$
- $P_X < 0.5$ GeV/c with $\vec{P}_X = \vec{0}_p + \vec{P}_e - \vec{P}_{e'} - \vec{P}_{p'} = \vec{P}_e - \vec{P}_{e'} - \vec{P}_{p'}$
- $0.88GeV < M_X < 1.04GeV$
- $\theta_q < 49.0^\circ$
- $|\phi_e - \phi_p| - 180.0^\circ | < 2.0^\circ$

⁹We chose this quantity Δ rather than the simple angle difference ($\theta_q - \theta_p$) because the former is more directly interpretable in terms of transverse missing momentum for the case of quasi-elastic scattering.

1168 where X indicates the missing entity in the $d(e,e'p)X$ channel, which is ex-
1169 pected to be neutron in the case of the quasi-elastic channel, thus E_X is the
1170 missing energy and so on.

1171 If it passes these cuts, the quantity Δ in Eq. 3.14 is calculated for
1172 the event and then histogrammed as shown by the red curves in the top-left
1173 (from ^{12}C runs), top-right (from NH_3 runs), and bottom-right (from ND_3
1174 runs) panels of Fig. 3.35.

1175 After getting the histograms for the quantity Δ for the ep-elastic or
1176 quasi-elastic events from the NH_3 , ND_3 and ^{12}C target data sets, we first
1177 remove the contribution from the non-hydrogen component of NH_3 and ND_3
1178 targets by subtracting the corresponding carbon histogram (properly scaled
1179 to match with the left-shoulders (mainly from the nuclear elastic background
1180 in each of the ammonia data)). Since the carbon data is too low in counts
1181 (hence the raggedness in the histogram), a fit (a 'gaussian' times a 'linear'
1182 function) to the carbon data is obtained, and that fit (shown as the blue
1183 line in the first panel in Fig. 3.35 is used instead of the histogram itself
1184 to remove the background. The blue line in the second (top-right) panel
1185 and the cyan line in the last (bottom-right) panel show the properly scaled
1186 carbon fits which are subtracted from the NH_3 and ND_3 histograms (shown
1187 by red lines) respectively. After the subtraction, we get new histograms
1188 that represent 'pure' elastic or quasi-elastic data from protons and deuterons
1189 (shown by the magenta lines in the third and last panels respectively).

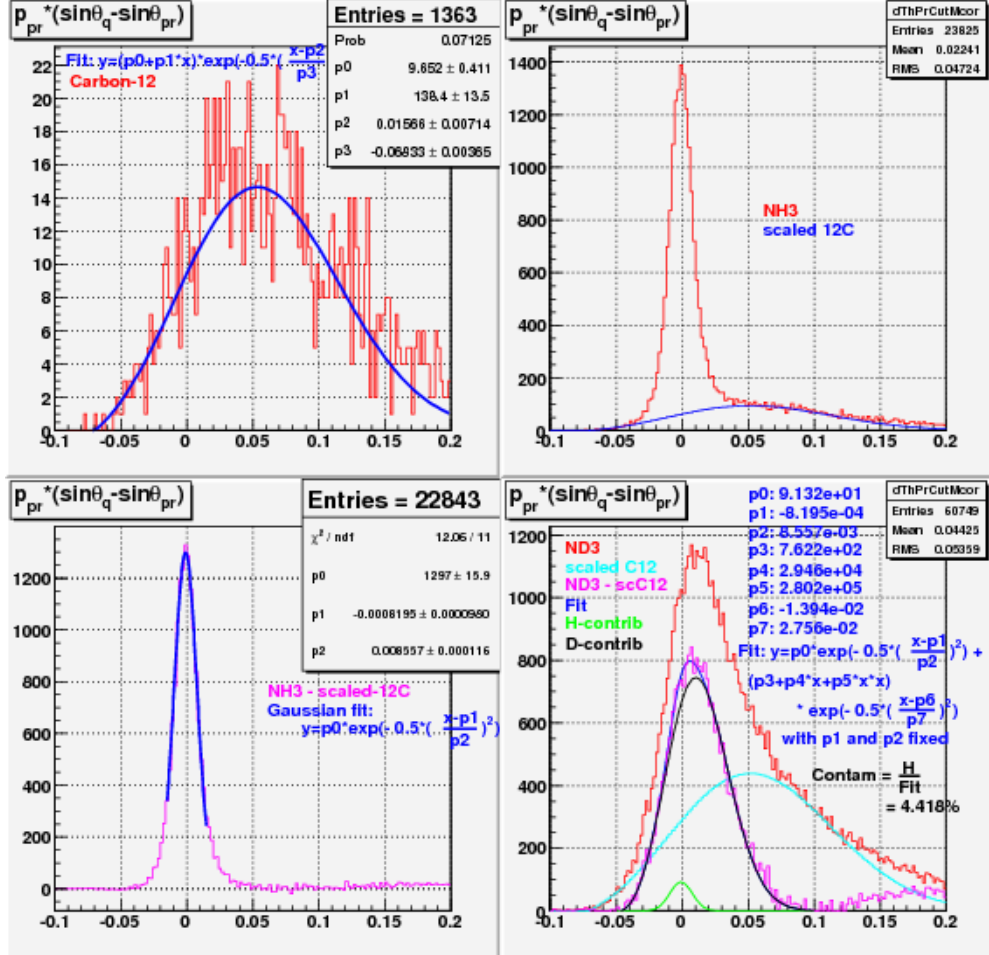


Figure 3.35: Histograms showing the quantity $\Delta = p_p \cdot (\sin\theta_q - \sin\theta_p)$ for elastic or quasi-elastic events from carbon-12 (top-left), NH₃ (top-right) and ND₃ (bottom-right) target runs respectively. The third (bottom-left) panel shows the background removed elastic events from the NH₃ data. In the fourth panel, various Δ are shown - red is the raw ND₃, light green is the scaled-¹²C for the nuclear background, brown is for the difference between the two.

1190 3.9.3 Extracting the Contamination

1191 After we have the 'pure' elastic or quasi-elastic data from NH₃ and ND₃ runs,
 1192 we get the mean and the spread (standard deviation σ) of the proton elastic
 1193 peak by fitting the NH₃ data to a Gaussian function $f_p(x)$ (the blue line in

1194 the third panel with parameters p0=height, p1=mean and p2= σ). After
 1195 we have the fit for the proton elastic peak, we fit the background subtracted
 1196 deuteron data to a function $f(x)$ that is a linear combination of the pure
 1197 proton fit and a pure deuteron fit (the latter with the form of **a quadratic**
 1198 **function \times a Gaussian**¹⁰) as follows:

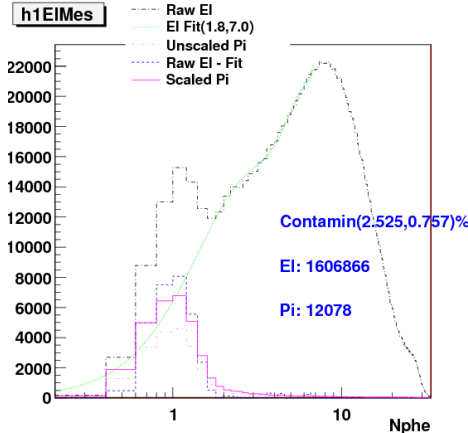
$$f(x) = p_0 \cdot f_p(x) + (p_1 + p_2 \cdot x + p_3 \cdot x^2) \cdot e^{-0.5 \cdot \left(\frac{x-p_4}{p_5}\right)^2} \quad (3.16)$$

1199 where p_i ($i = 0, 2, \dots, 5$) are the free parameters which are determined by
 1200 fitting of $f(x)$ to the deuteron data. The first term $p_0 \cdot f_p(x)$ in $f(x)$ represents
 1201 the contribution from the contaminant (i.e., protons in ND_3) and the rest
 1202 of the term in $f(x)$ represents the contribution from the deuterons in ND_3 .
 1203 The total fit function $f(x)$, the proton contribution and the deuteron part are
 1204 shown by the blue, green and black lines in the fourth panel. The ratio of
 1205 the area under the green line to that under the blue line gives us the relative
 1206 amount of the NH_3 contamination in the ND_3 target.

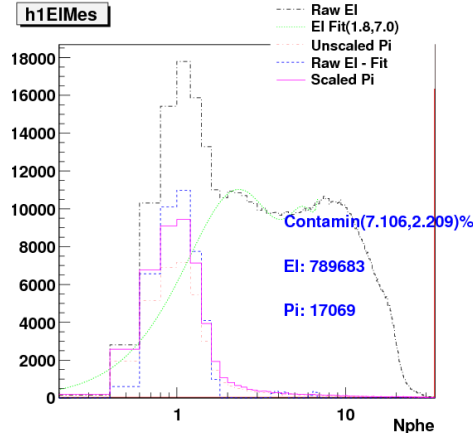
1207 3.9.4 Results and Conclusion

1208 From the calculation as described above, the estimate for the ND_3 contam-
 1209 ination came out to be 4.4% It was not possible to do a similar analysis on
 1210 the 1.3 GeV ND_3 data, because the CLAS acceptance constraints did not al-
 1211 low for the coincident detection of e and p from the exclusive (quasi-)elastic
 1212 events. The basic conclusion is that at 2 GeV, we cannot get a 'pure' Gaus-
 1213 sian spectrum for deuteron, and therefore, there is no way to unambiguously
 1214 separate deuteron from proton in ND_3 . The fact that the fit looks reason-
 1215 ably well (with contamination coming out to be only a few percent) and that
 1216 we clearly do not see a narrow peak on top of a wider one (unlike in EG1-
 1217 DVCS) should be sufficient to ascertain that EG4 did NOT have the same
 1218 contamination problem as EG1-DVCS (which still has not been explained
 1219 yet) [25]. To accommodate the fact that the contamination measurement is
 1220 not reliably unambiguous, we will assume a rather generous systematic error
 1221 due to the contamination.

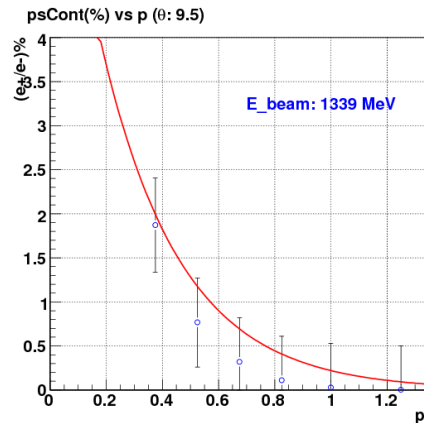
¹⁰A pure Gaussian and other forms for the deuteron spectrum were tried but the overall fit was not as good.



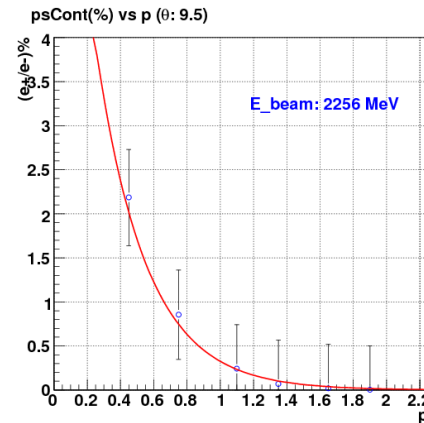
(a) For the first bin in momentum and seventh bin in θ .



(b) For the first bin in momentum and eighth bin in θ .



(c) Fits in the $\theta(9.0, 10.0)$ bin for 1.339 GeV data.



(d) Fits in the $\theta(9.0, 10.0)$ bin for 2.0 GeV data.

Figure 3.33: The top row plots show the calculation of pion contamination of electrons for the given kinematic bins of 3.0 GeV data. The dotted black line indicated by the label “Raw El” in the legends of each of the two plots are the contaminated electrons. Likewise, the line labeled “El Fit” is a polynomial fit to the electron distribution (in this case fitted from Nphe=1.8 to 7.0, but extrapolated down to Nphe=0). The line labeled “Unscaled Pi” is the pure pion distribution obtained with stringent set of cuts. “Raw El - Fit” is the difference between the contaminated electron sample and the polynomial fit and finally “Scaled Pi” is the pure pion-sample but after its scaled to match with the “Raw El - Fit” at the pion peak position (around 1 Nphe). The bottom row plots show the fits of the contaminations as a functions of momentum (p) in a given θ bin.

1222 Chapter 4

1223 Monte Carlo Simulations and 1224 Extraction of g_1 and $A_1 F_1$

1225 4.1 Simulation and Approach to Analysis

The EG4 data consist of a table numbers of electrons reconstructed within various (W, Q^2) bins that are scattered off polarized hydrogen (NH_3) or deuteron (ND_3), divided by the (life-time gated) integrated charge, for two different combinations of target polarization and beam helicity:

$$n^\pm = N^\pm / FC^\pm, \quad (4.1)$$

where “+” refers to beam helicity and target polarization anti-parallel, while “−” refers to the parallel case. The difference between these two normalized counts is given by

$$\Delta n(W, Q^2) = n^+(W, Q^2) - n^-(W, Q^2) = \mathcal{L}_r \cdot P_b P_t \cdot \Delta\sigma(W, Q^2) \cdot AccEff(W, Q^2) + Bg \quad (4.2)$$

1226 where the “relative luminosity” \mathcal{L}_r is a constant factor containing the density of polarized target nuclei per unit area and the conversion factor from 1227 Faraday cup counts to integrated number of electrons incident on the target; 1228 P_b and P_t are the beam and target polarization, Acc and Eff are the 1229 geometric acceptance and detection efficiency of CLAS for electrons within 1230 the kinematic bin in question (including cuts and trigger efficiency), and 1231 the background Bg comes from several sources, including pions misidentified 1232 as electrons, electrons from e^+e^- pair production, and electrons scattered off 1233 (partially) polarized target nucleons and nuclei that are not the 1234

intended species (e.g., bound protons in ^{15}N , free proton contamination in nominal ND_3 targets, and bound proton-neutron pairs in any ^{14}N contamination present)¹.

Our main goal is to extract the spin structure function g_1 and calculate its moments. The cross section difference $\Delta\sigma(W, Q^2)$ on the right side of the above equation is what contains the information on $g_1(W, Q^2)$ along with various other contributions.² This means we can, in principle, calculate the cross section (and then use that to extract g_1), from the background corrected measured quantity $\Delta n(W, Q^2)$ by putting in the values for all the rest of the quantities involved in Eq. 4.2. But, in reality, having an accurate knowledge of Acc and Eff is challenging and the available measurements of polarizations and luminosities are not reliable enough. So, experimentalists usually resort to Monte-Carlo simulation to determine some or all of those factors that are involved in the relation between the counts and cross-section differences.

A standard way to extract the sought-after Physics quantities from these kinds of measurements proceeds along the following steps [37]:

1. Use a full simulation of CLAS with a “realistic” event generator, detector simulation and event reconstruction including cuts to obtain the product AccEff as the ratio of events reconstructed in a particular bin, divided by events thrown in that same bin.
2. Extract the product $\mathcal{L}_r \cdot P_b P_t$ from the ratio of the acceptance and efficiency corrected Δn in the (quasi-)elastic region ($0.9 < W < 1.0$) to the well-known theoretical cross section difference for elastic (or quasi-elastic) scattering off the proton (deuteron).
3. Estimate and correct for Bg .
4. Apply radiative corrections, which use a model of the unradiated Born cross section and a calculation of the radiated cross section based on programs like RCSLACPOL (see below).

¹While this background is a small correction for hydrogen targets, in the case of deuteron targets, it must be corrected for (see Sec. 5.1).

² $\Delta\sigma(W, Q^2)$ also has contributions from the unmeasured g_2 or, equivalently, from the product $A_2 F_1$. Moreover, the cross section receives modifications and tails from radiative effects (both internal and external radiation) and kinematic resolution smearing.

- 1264 5. Express the extracted Born cross section difference in terms of the de-
 1265 sired quantity (here: g_1) and additional inputs (e.g., $A_2 F_1$). Use a
 1266 model for the latter to extract g_1 only. Vary the model (concurrently
 1267 with the model input to the previous step) to assess systematic uncer-
 1268 tainties.

1269 One conceivable problem with this approach lies in the first step, and in
 1270 particular with the choice of the “realistic event generator”. However, this
 1271 choice would not matter at all if two conditions are fulfilled [37]:

- 1272 1. The kinematic bins are chosen so small that the variation of the cross
 1273 section over the bin (and/or the corresponding variation of the accep-
 1274 tance times efficiency) do not lead to any significant deviations for the
 1275 *average AccEff* between the simulation and the real detector.
- 1276 2. The counts reconstructed within any one bin are directly proportional
 1277 to the number of initial electrons generated within that *same* bin (the
 1278 proportionality constant being *AccEff*), without any “bin migration”
 1279 from other kinematic bins. (Otherwise, the ratio reconstructed/generated
 1280 depends on those “migration tails”, and the simulation will give differ-
 1281 ent results from the “true value” if the overall cross section model of
 1282 the generator is not accurate enough.)

1283 Unfortunately, assumption 1 tends to directly contradict assumption 2
 1284 because 1 favors small bins and 2 favors large bins! For most precision
 1285 experiments, bin migration effects are significant. This is aggravated by
 1286 the difficulty of making a clean separation between bin migration due to
 1287 detector resolution alone and the contribution from radiative effects. For
 1288 instance, GEANT and therefore GSIM includes (at least by default) photon
 1289 radiation as part of the simulation of outgoing electron tracks throughout
 1290 the gas and building materials of all detectors. It is very important not to
 1291 “double count” when simulating an experiment; the radiative calculations in
 1292 step 4 above should not include any “after” radiation beyond the limit of
 1293 the target itself (which, in turn, should then **NOT** be included in the GSIM
 1294 simulation as material to be traversed).

1295 This is a problem for all CLAS experiments attempting to extract abso-
 1296 lute cross sections (or, here, cross section differences); however, the problem
 1297 is magnified for our case: Since the cross section difference itself is not re-
 1298 quired to be positive, one can have both positive and negative tails migrating

1299 into adjacent bins. In any case, it is clear that using the average, **unpolarized**
1300 cross section as a model for the generator is not really appropriate (unless
1301 one is confident that the asymmetry is fairly constant or slowly-varying – not
1302 a good assumption in the resonance region where the $\Delta(1232)$ with negative
1303 asymmetry is adjacent to the S11 with positive asymmetry). Using a (hope-
1304 fully realistic) model of the cross section difference instead would be much
1305 better, but this causes two new problems [37]:

- 1306 1. Prima facie it is unclear how to simulate a negative cross section (dif-
1307 ference). This problem can be circumvented fairly easily (see below),
1308 albeit at extra cost in terms of simulation effort.
- 1309 2. It obviously becomes impossible to extract $AccEff$ from a simple ratio
1310 of reconstructed divided by generated events; both of these quantities
1311 could be positive, negative (even different sign under extreme circum-
1312 stances), or simply zero (which is particularly bad for the denominator).
1313 From this discussion, it is also clear that such a ratio would depend very
1314 sensitively on the cross section model and bin migration tails and be a
1315 very poor indicator of the actual product $AccEff$.

1316 For this reason, we decided to try a different approach outlined in the
1317 following. The basic idea is to study the dependence of the reconstructed
1318 count difference on the model input (in particular g_1) directly through the
1319 whole chain of simulation and reconstruction, and then use tables of Born
1320 and radiated cross section differences for various model inputs as estimates
1321 of systematic uncertainties³.

1322 4.1.1 Outline of the method

1323 The basic idea is the following: If we already had a perfect model of g_1 and all
1324 other ingredients that go into Δn (including a perfect simulation of CLAS), a
1325 simulation of Δn would agree 100% with the data (within statistical errors).
1326 Any (larger than statistical) deviation between such a simulation of Δn and
1327 the data can only be due to the following possible sources:

- 1328 1. The model for g_1 is not perfect and, therefore, must be adjusted to
1329 reflect the “true” g_1 . This is the default assumption which we will use

³We developed this method for the case of an ND₃ target; however, it could, of course, easily be adopted to NH₃, as well

1330 to extract g_1 from the data. This will be done by finding the proportionality factor between *small* changes in g_1 and the reconstructed Δn
1331 and then adjusting g_1 to fully account for the observed Δn .
1332

- 1333 2. There could be a systematic error on this proportionality factor (which,
1334 after all, will come from simulation); for instance, there could be sys-
1335 tematic deviations from the simulated results for acceptance and effi-
1336 ciency (in particular efficiencies of the CC, EC, or tracking, that are
1337 not perfectly simulated by GSIM). This is a multiplicative uncertainty
1338 that must be carefully estimated and applied to the final data.
- 1339 3. Any imperfect simulation of the “background” due to all events not
1340 originating in the bin in question (migration, radiation), or due to
1341 undesired target components (hydrogen, bound polarized nucleons in
1342 nitrogen), or from misidentified pions or e^+e^- pairs, or due to contribu-
1343 tions to $\Delta\sigma$ from A_2 can lead to an additive systematic deviation
1344 that would then be misinterpreted as a change in g_1 . This systematic
1345 uncertainty must be studied by varying model inputs, parameters etc.
1346 in the simulation.

1347 4.2 Radiative Corrections

1348 The physics quantities that we seek to extract from measurements are theo-
1349 retically defined or interpreted and calculated in terms of the cross-section of
1350 the so called “Born” scattering process, which is represented by the simplest
1351 possible Feynman diagram i.e., by the lowest order approximation of a single
1352 photon exchange process. However, the measured cross-sections also contain
1353 contributions from higher order electromagnetic processes, which must be
1354 accounted for before extracting the quantities of our interest. These additional
1355 contributions are grouped into two categories - **internal and external**
1356 radiative corrections.

1357 The **internal corrections** are the contributions from the higher order
1358 QED processes (higher order Feynmann diagrams) which occur during the
1359 interaction. These include the correction for the internal Bremsstrahlung
1360 (i.e., the emission of a real photon while a virtual photon is being exchanged
1361 with the target) by the incoming or the scattered electron), the vertex correc-
1362 tion (in which a photon is exchanged between the incoming and the scattered
1363 electron), and the correction for the vacuum polarization of the exchanged
1364 virual photon (e^+e^- loops).

1365 External corrections include those that account for the energy loss (mainly
1366 by the Bremsstrahlung process) of electrons well before or after the interac-
1367 tion while passing through the target material and the detector.

1368 If the beam electron radiates a photon before the scattering, the kinemat-
1369 ics of the actual process will be different from the the one calculated with the
1370 nominal beam energy. Likewise, if the radiation occurs after the scattering,
1371 the actual energy and momentum of the scattered electron will be different
1372 from what is calculated normally (i.e., without any radiation). The effect
1373 can be quite large for elastic scattering.

1374

1375 4.3 “Standard” simulation

1376 The simulation process consists of mainly three parts - generating inclusive
1377 events similar to the ones produced in the double polarization scattering
1378 process, simulating the CLAS detector response, and finally the event recon-
1379 struction from the simulated detector signals.

1380 The first part is accomplished by using a program that is made by com-

1381 bining the essential elements of an updated version of the “RCSLACPOL”
1382 program (for cross section generation) and some parts of the “STEG” (Sim-
1383 plesT Event Generator) event generator (see sections 4.3.1 and 4.3.2). The
1384 second part is done by two standard CLAS software packages running in
1385 succession - “GSIM” and “GPP”(see sections 4.3.3 and 4.3.4). And, finally,
1386 the standard CLAS package “RECSIS” is used to reconstruct the events in
1387 the same way as for the real CLAS data.

1388 4.3.1 RCSLACPOL

1389 The simulation for the standard model cross sections proceeds as follows.
1390 We use the code “RCSLACPOL” [38] that can generate polarized and un-
1391 polarized cross sections (both Born and radiated) based on the approach by
1392 Shumeiko and Kuchto [39] as well as Mo and Tsai [40], including external
1393 radiation in the target. This code has been extensively tested and used for
1394 the analysis of SLAC experiments E142, E143, E154, E155 and E155x as
1395 well as Jefferson Lab experiments like EG1a and EG1b. It has been updated
1396 with the most recent models on polarized and unpolarized structure func-
1397 tions (F_1 , F_2 , A_1 and A_2) [38, 41–43] and an implementation of the folding
1398 algorithm developed by W. Melnitchouk and Y. Kahn [44] for structure func-
1399 tions of the deuteron. The models have been fitted to and tested with data
1400 from EG1b as well as world data on both A_1 and A_2 over a wide range of Q^2
1401 and W , including the resonance region and the DIS region.

1402 For EG4, we have combined the “RCSLACPOL” code with that of the
1403 “STEG” event generator. This generator uses a grid of (radiated) cross sec-
1404 tions generated by our modified version of RCSLACPOL to generate events
1405 that are distributed according to these cross sections (i.e., the number of
1406 events generated in a given bin is proportional to the cross section integrated
1407 over this bin).

1408 4.3.2 Event Generator

1409 The concept and some part of the generator skeleton was inherited from the
1410 STEG (SimplesT Event Generator) program obtained from INFN, in Genova,
1411 Italy. The old event sampling part (which made the program run extremely
1412 slow) of the code was replaced by a new one developed by myself which
1413 made the event generation process much faster. The cross section calculating

1414 part was replaced by codes from an updated version of RCSLACPOL (see
1415 Sec. 4.3.1).

1416 The generator works in two steps. First, it generates two separate two-
1417 dimensional maps or tables (in $(p, \cos\theta)$ space) of radiated inclusive polarized
1418 cross differences (for the scattering of polarized electrons from a longitudi-
1419 nally polarized deuteron target, by using RCSLACPOL) in various kinematic
1420 bins encompassing the kinematic region covered by EG4 data. One map is for
1421 positive values of polarization $\Delta\sigma$ and the other is for negative values of the
1422 polarization. These cross section maps (and the corresponding events later
1423 on) were generated in the following angular and momentum ranges: 5.0-45.0
1424 degrees for θ , 250.0-325.0 degrees for ϕ (to ensure the CLAS 6th sector is
1425 completely covered) and $(0.2, E_{beam})$ GeV for the momenta, where the beam
1426 energy E_{beam} took values of 1.337 and 1.993 GeV, corresponding to the two
1427 ND₃ data sets of EG4. In our case, the map was created by dividing the
1428 kinematic phase space into a grid of small rectangles and then calculating
1429 the differential cross-section at the geometric center of each of those squares
1430 (such as ABCD in Fig. 4.1). For our application, we need to generate two
1431 such maps (because of the impossibility of generating events according to
1432 negative cross-sections) and run the program twice - once corresponding to
1433 positive $\Delta\sigma$ and the next for the negative one. For all bins in which the inte-
1434 grated cross section $\Delta\sigma \geq 0$, we fill the first table (“positive map”) which is
1435 therefore positive-definite. For all bins in which this cross section is below 0,
1436 we fill a second table (“negative map”), but with the absolute (i.e. negative)
1437 value of this cross section.

1438 In the second stage, events are thrown according to the cross section maps
1439 produced in the first stage. The events are given vertex coordinates that are
1440 uniformly distributed over the volume of a 1 cm long cylinder with radius
1441 0.01 cm around the beam line - with the center of this volume being at the
1442 EG4 target position of $(0, 0, -100.93$ cm). Nearly equal numbers of events are
1443 generated for each sign of $\Delta\sigma$; they are finally normalized according to their
1444 total cross sections (integrals of the corresponding maps).

1445 The kinematic and other information (positions, momenta, charge) of
1446 these generated events are recorded and saved in the BOS format⁴ output
1447 files which organizes data into banks. In our case, HEAD, MCEV, MCTK,
1448 and MCVX banks are used for the generator output. The generator is also
1449 capable of producing output in the hbook format which makes it possible

⁴Existing versions of GSIM, GPP and RECSIS accept only BOS format for input files.

1450 to study the Monte Carlo data using PAW (or ROOT because the h2root
1451 program easily converts “hbook” files into “root” files).

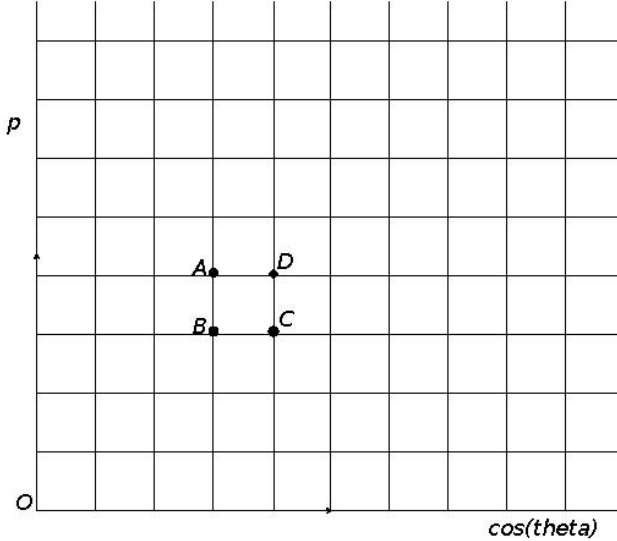


Figure 4.1: Corners of a typical bin highlighted in the kinematic space covered by the event generator.

1452 4.3.3 GSIM - CLAS Detector Simulation

1453 The Monte Carlo events thus generated are next fed into GSIM - the CLAS
1454 Monte Carlo simulation program using GEANT 3.21 libraries from CERN
1455 [45]. It simulates the CLAS detector response by implementing a complete
1456 model of the detector as well as the propagation of particles through different
1457 materials including all physics processes, such as multiple scattering, energy
1458 loss, pair production, and nuclear interactions. The program takes the in-
1459 put event particles and then, based on their types, momenta and positions,
1460 “swims” (traces) them through all volumes of different materials that are
1461 defined using various library routines and the detector parameters. Charged
1462 particles are also subjected to the effects of the torus and target magnetic
1463 fields of the same strength as in the actual experiment (for this the same field
1464 maps are used as in the track reconstruction process using RECSIS). All the
1465 ingredients of the program (field maps, active detection volumes, passive vol-
1466 umes of detector support structures etc) are modeled as accurately as possible

1467 with the help of engineering designs and actual detector measurements. Spe-
1468 cial subroutines corresponding to various active parts of the detector produce
1469 outputs resembling the real detector signals which can then be reconstructed
1470 and analyzed just as the real experimental data [46][47]. GSIM is configured
1471 to match with the conditions of a given experiment by giving it proper val-
1472 ues of input parameters via a command line input file which contains various
1473 “ffread cards” some of which are listed in table-A.1 along with their values
1474 that were used in our simulation.

1475 **4.3.4 GSIM POST PROCESSOR (GPP)**

1476 The GSIM output is next passed onto GPP - another standard CLAS soft-
1477 ware package - to process the simulated data further so that the detector
1478 response is accounted for more accurately. This package improves the re-
1479 sponse by smearing the detector signals and removing them if there are dead
1480 regions (determined by querying a data base which in turn is made by looking
1481 at the raw data of the experiment).

1482
1483 A lot of known, unknown, quantified, and unquantified factors such as
1484 temperature, alignment, dead channels, electronic malfunction etc affect the
1485 performance of the CLAS detector. But, GSIM does not include all these
1486 effects and, hence, the efficiency of the detector is always less than what
1487 the simulation provides us. To make the simulation more realistic by taking
1488 into account some of those effects, another CLAS software called GSIM Post
1489 Processor (GPP) is used to process the GSIM output. The GPP can change
1490 the DC, SC, CC and EC signals produced in the simulation⁵.

1491 As the experimental conditions and detector configurations can change
1492 from one experiment to another, in order to run the GPP, we must have
1493 our own experiment specific calibration constants and parameters such as
1494 the run number (R), the DC smearing scale values for regions 1, 2 and 3
1495 (a, b, c) and the SC smearing scale value (f). Even for a given experiment,
1496 these constants and parameters are determined to be different for different

⁵The DC signals can be changed by (a) accounting for the dead wires according to the calibration database, (b) shifting the DOCA mean value, and (3) smearing the hit signals according to the resolution determined by the calibration database or according to the command line input. Likewise, SC signals can be changed with a parameter input for smearing the time resolution. And, for EC signals, the GPP can use the hardware thresholds [48].

1497 data sets (corresponding to a given beam energy, for example). The value
1498 for R can be any run number belonging to a specific data set. This number
1499 is used to identify the entry of the calibration constants in the database that
1500 corresponds to the given data set. In order to simplify the job, we decided to
1501 use the timing resolutions determined by the calibration database assuming
1502 that they are good enough and need only to determine new values for the
1503 DC smearing. To further simplify the job, we assumed that the three DC
1504 Regions had identical resolutions, so the DC smear parameters a, b, and c
1505 would have the same values, and the common DC-smear value is what is
1506 determined from the procedure described below.

1507 In order to determine the DC-smear, we generated a statistically significant
1508 number (about half million) of elastic-electron events distributed according
1509 to the elastic cross section and then ran them through GSIM, GPP
1510 and RECSIS. The pure proton target events, turning off the radiative effects
1511 are generated using the existing STEG event generator.

1512 The simulated elastic events are then fed into GSIM, GPP and RECSIS,
1513 with GSIM and RECSIS used in the same configuration as when processing
1514 the CLAS data during the “pass-1” phase, and GPP run with different values
1515 of DC-smear scales as inputs. The reconstructed data coming out of RECSIS
1516 corresponding to a given value of DC-smear is then histogrammed in ΔE
1517 again and fitted to a Gaussian to get its σ (characterizing width) and mean
1518 (characterizing position). As we can see in figures 4.2(a) and 4.2(b), the width
1519 of the elastic peak increases with the DC-smear but the position stays more
1520 or less the same as expected. In fact, when the two are plotted against DC-
1521 smear (as in figures 4.3(a) and 4.3(b)) the width shows a linear dependance.

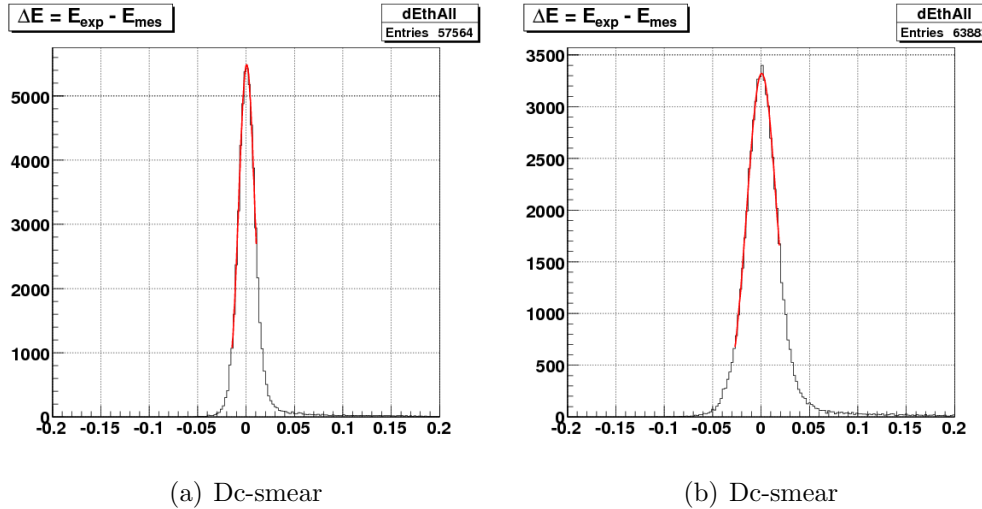


Figure 4.2: ΔE of 2.3 GeV simulated elastic-only proton-target events passing through GSIM, GPP (with two different Dc-smear scales of 1.3 (a) and 2.9 (b)), and RECSIS.

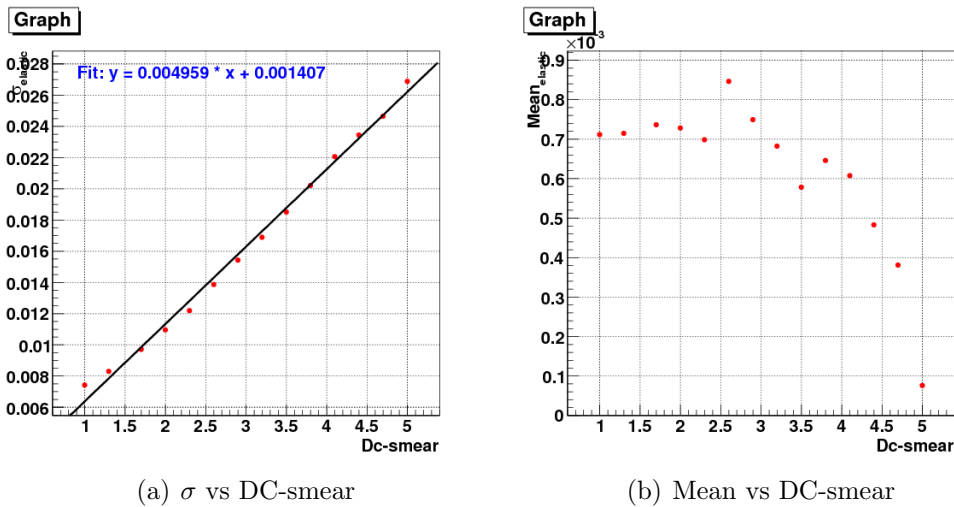


Figure 4.3: Graphs showing the dependence of width and position (obtained from the Gaussian fits as shown in the fig (??) of the elastic peaks on the DC-smear applied to GPP.

1522 **4.3.5 Finding the width of the real CLAS data elastic
1523 peak.**

1524 With the knowledge of the DC-smear dependence of energy resolution (Fig.
1525 4.3(a)), if we also know the resolution in the real data, we can determine the
1526 right value of DC-smear which would make the resolution in the simulation
1527 comparable with that in the real data. So, the next step is to find the
1528 resolution in the real CLAS data, which is done again by measuring the
1529 width of the elastic peak in the real data. But, because the real data is a
1530 very complex mixture of events coming from various reaction channels, we
1531 must first have a way to separate the elastic data from the rest. One method
1532 entails histogramming ΔE from both the NH_3 and ^{12}C target data (for a
1533 given beam energy) and subtracting the latter (after cross-normalization)
1534 from the former (as in fig (4.4)) to effectively remove the contribution from
1535 nitrogen component of the NH_3 target leaving the contribution coming only
1536 (mostly) from the proton component. Another method consists of using
1537 only the NH_3 data but this time calculating the helicity dependent cross-
1538 section difference in the elastic region Fig. (4.5). In the latter method, the
1539 difference removes the contribution from the unpolarized nuclear background
1540 because they have the same contribution to the opposite helicity state cross-
1541 sections. After the elastic data is separated, its ΔE distribution is fitted to
1542 a Gaussian as with the simulation data and we arrive at the experimental
1543 energy resolution.

1544 Using the first of the two methods mentioned above, the real data reso-
1545 lutions were evaluated for three different polar angle (θ) cuts - all θ (in fact
1546 $\theta \geq 7^\circ$), $\theta > 15^\circ$, and $\theta > 20^\circ$. The dependence of these experimental res-
1547 olutions on the beam energy for these cases are shown together in the Fig.
1548 4.6, along with the resolution for the case “all θ ”, but determined from the
1549 cross-section difference method. Likewise, as described above, the DC-smear
1550 dependence of the simulated resolution were determined separately for all
1551 these three cases of angle cuts, so that we could compare the experimental
1552 resolutions with the simulations correspondingly. One such comparison is
1553 illustrated in the figure 4.7, where we show resolutions evaluated for the case
1554 of “all θ ” - first two for the experimental data and the rest for the simulated
1555 data.

1556 Looking at Fig. 4.6, it is obvious that the resolution is θ -dependent as ex-
1557 pected. When the experimental and simulated resolutions are compared for
1558 the three different cases of θ cuts, we realize that the GPP asks for the θ de-

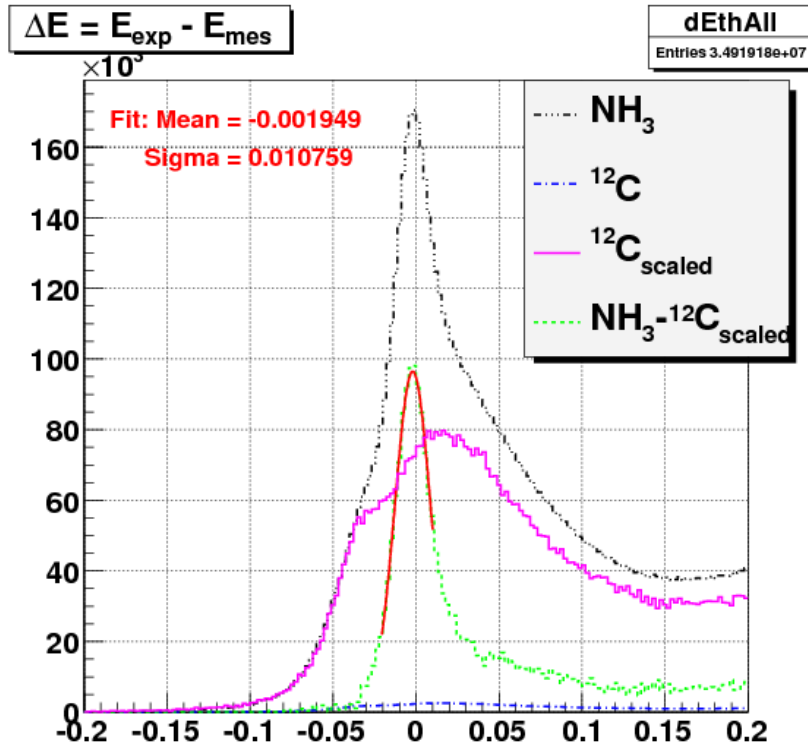


Figure 4.4: Histograms illustrating the extraction of elastic peak for 2.3 GeV by using carbon-12 data for background removal from the total-cross section (all good electrons with $\theta > 7$ used).

1559 pendent DC-smearing, which makes the simulation work very complicated
 1560 with the current version of GPP. To simplify the situation, we decide to have
 1561 a global (θ independent) value of DC-smearing (for a given beam energy) by
 1562 comparing the experimental and simulated resolutions corresponding to the
 1563 case of “all θ ” cut. By taking into account the fact that there seems to be
 1564 an inherent uncertainty in the measurement of the resolutions (evident from
 1565 the discrepancy of the experimental resolutions determined from the two dif-
 1566 ferent methods) and comparing the experimental and simulated results, the
 1567 values as listed in Table. 4.1 are chosen for the DC-smearing scales for the
 1568 GPP.
 1569

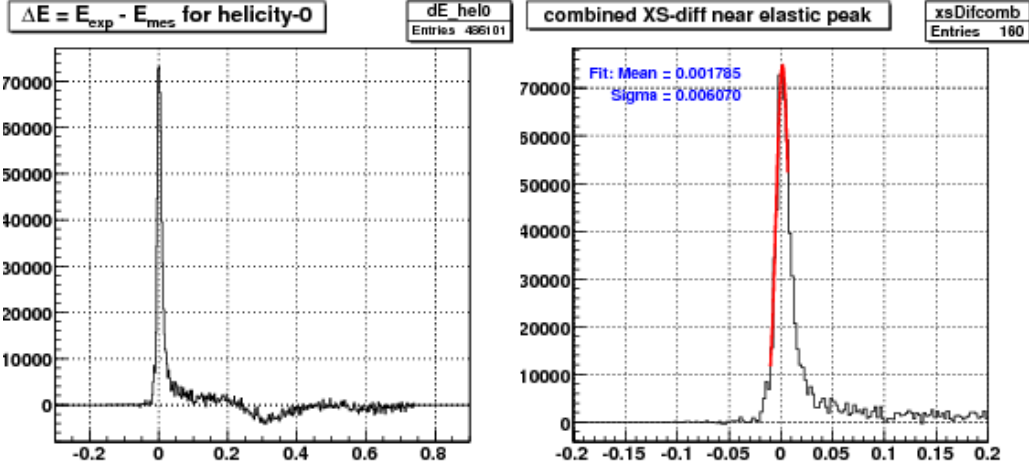


Figure 4.5: Plots showing the cross-section difference for 2.3 GeV NH₃ target data with the right one zoomed in around the elastic region (all good electrons with $\theta > 7$ used).

Table 4.1: DC-smearing scales determined for different beam energies.

E_{beam} (GeV)	1.054	1.339	1.989	2.256	2.999
DC-smear	2.6	2.0	2.0	2.0	1.7

1569

1570 4.4 Comparison of Data and Simulation

1571 Using our final values for the smear parameters, the simulated data were
 1572 passed through GPP and then reconstructed with RECSIS. Finally, all ap-
 1573 plicable cuts and corrections were applied to both sets of polarized simu-
 1574 lation data. Because the CC was turned off in GSIM for the simulation, all
 1575 experimental data cuts except those depending on CC were applied to the
 1576 simulated data. However, the cuts were modified (see Sec. 3.3) to account
 1577 for differences between simulation and data.

1578 In the end, we had two sets of simulated events (for the two cases of
 1579 $\Delta\sigma \geq 0$ and $\Delta\sigma < 0$) in each kinematic bin. The number of these two
 1580 type of events in each bin were then cross-normalized with respect to each

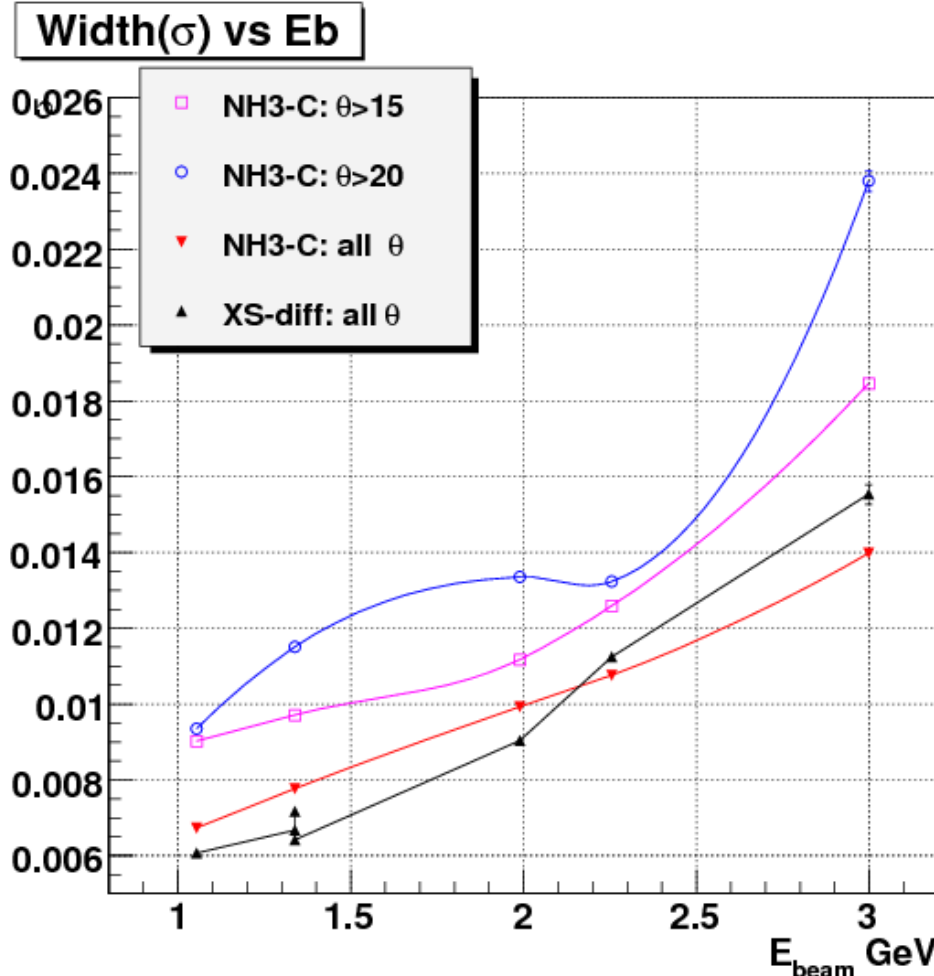


Figure 4.6: Graphs showing the dependence of width (σ) of the elastic peaks (from experimental data) on the beam energy (GeV).

other by their respective cross-section map integrals and the number of generated Monte-Carlo events and then combined to make the simulated polarized count difference Δn . To do that, the number of simulated event counts in a kinematic bin corresponding to the positive $\Delta\sigma$ was kept unchanged but the one corresponding to the negative $\Delta\sigma$ was multiplied with the following

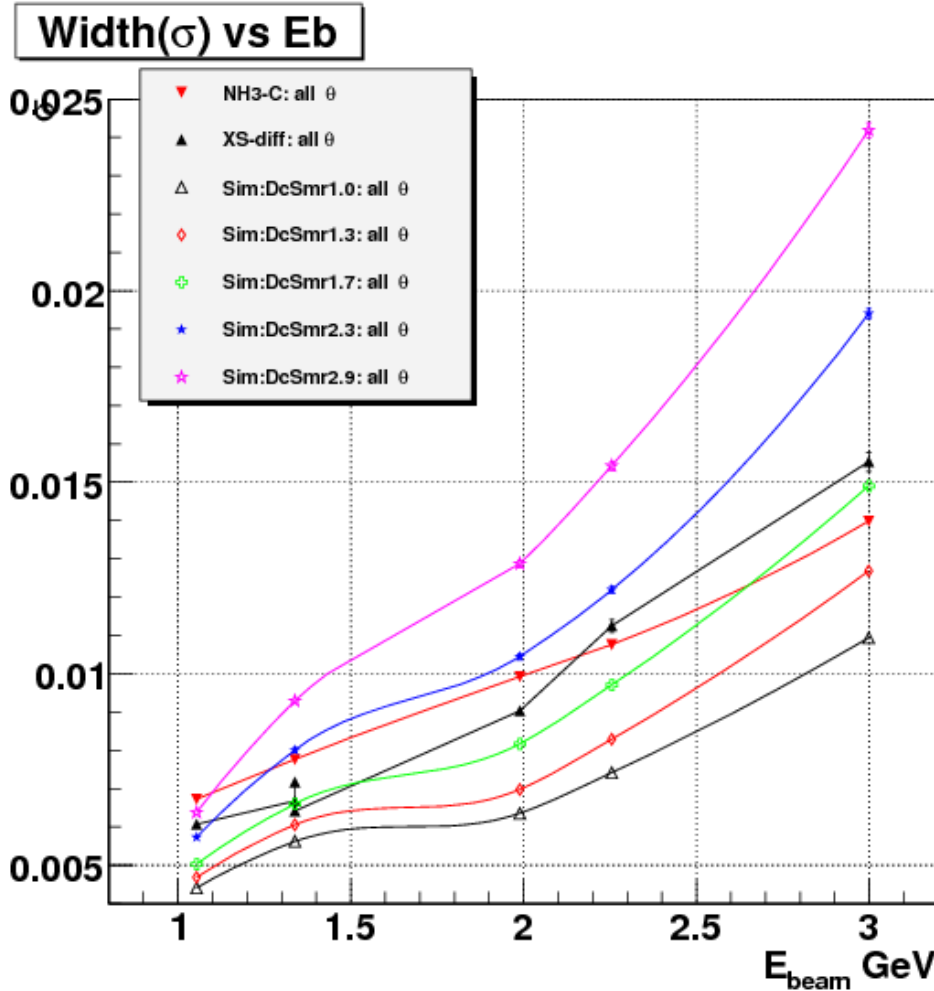


Figure 4.7: Graphs showing the dependence of width (σ) of the elastic peaks (from both experimental and simulated data) on the beam energy (GeV).

₁₅₈₆ normalization factor:

$$norm^- = \frac{\sigma_{tot}^-}{\sigma_{tot}^+} \times \frac{N^+}{N^-} \quad (4.3)$$

₁₅₈₇ where $\sigma_{tot}^{+/-}$ and $N^{+/-}$ are the total integral of the cross section map and
₁₅₈₈ the corresponding number of Monte-Carlo events generated for each of the
₁₅₈₉ polarization cases (+/-).

1590 The next step was to properly cross-normalize the simulated events to
1591 the data. For this, we found the scale factor SF necessary to have the same
1592 Δn in the quasi-elastic region (e.g., $0.9 \leq W \leq 1.0$). This factor represents
1593 the ratio

$$SF = \frac{n^+ - n^-}{\Delta n(simul)} \quad (4.4)$$

1594 since the physics of QE is known (from form factors etc), we expect the
1595 simulation in this region is reliable and all other factors are common to the
1596 simulation and the data. In fact, we chose one Q^2 bin (the 20th one - for
1597 which the agreement between the data and simulation was among the best)
1598 and calculated above ratio to get the global preliminary value of the scaling
1599 factor SF_{20} . The simulated Δn was then multiplied with this factor to get
1600 our best “prediction” of the real data in all the kinematic bins, in order to
1601 directly compare it with the real data (see Figs. 4.8 and 4.9).

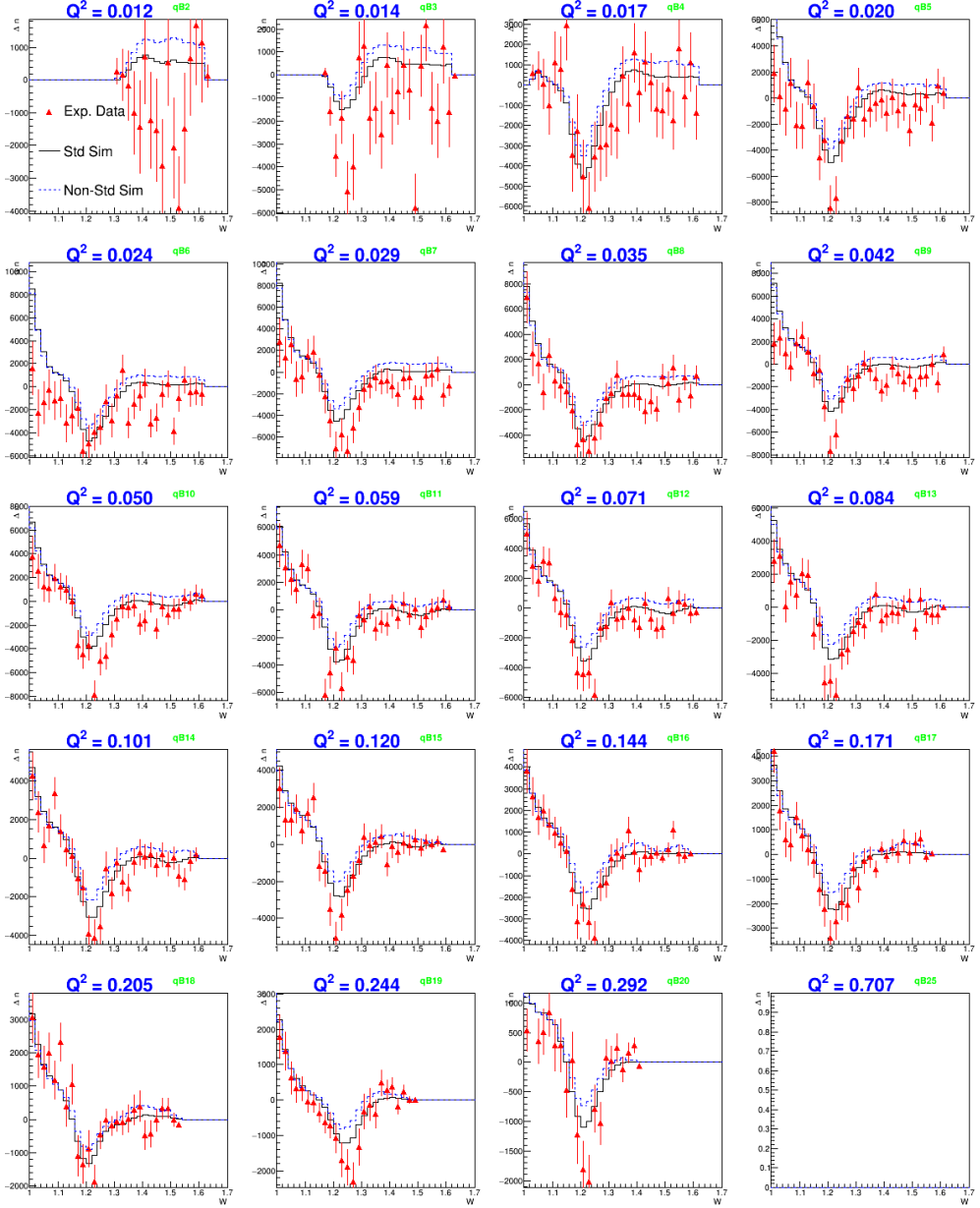


Figure 4.8: Comparison (in different Q^2 bins) of polarized count differences from 1.3 GeV experimental (red points with error bars) and two versions of normalized simulation data. The black continuous histograms are for “standard” simulation with values of A_1 in the inelastic region as given by the model used in the simulation. The blue dotted histograms are for “non-standard” simulated data with A_1 changed to $A_1 + 0.1$.).

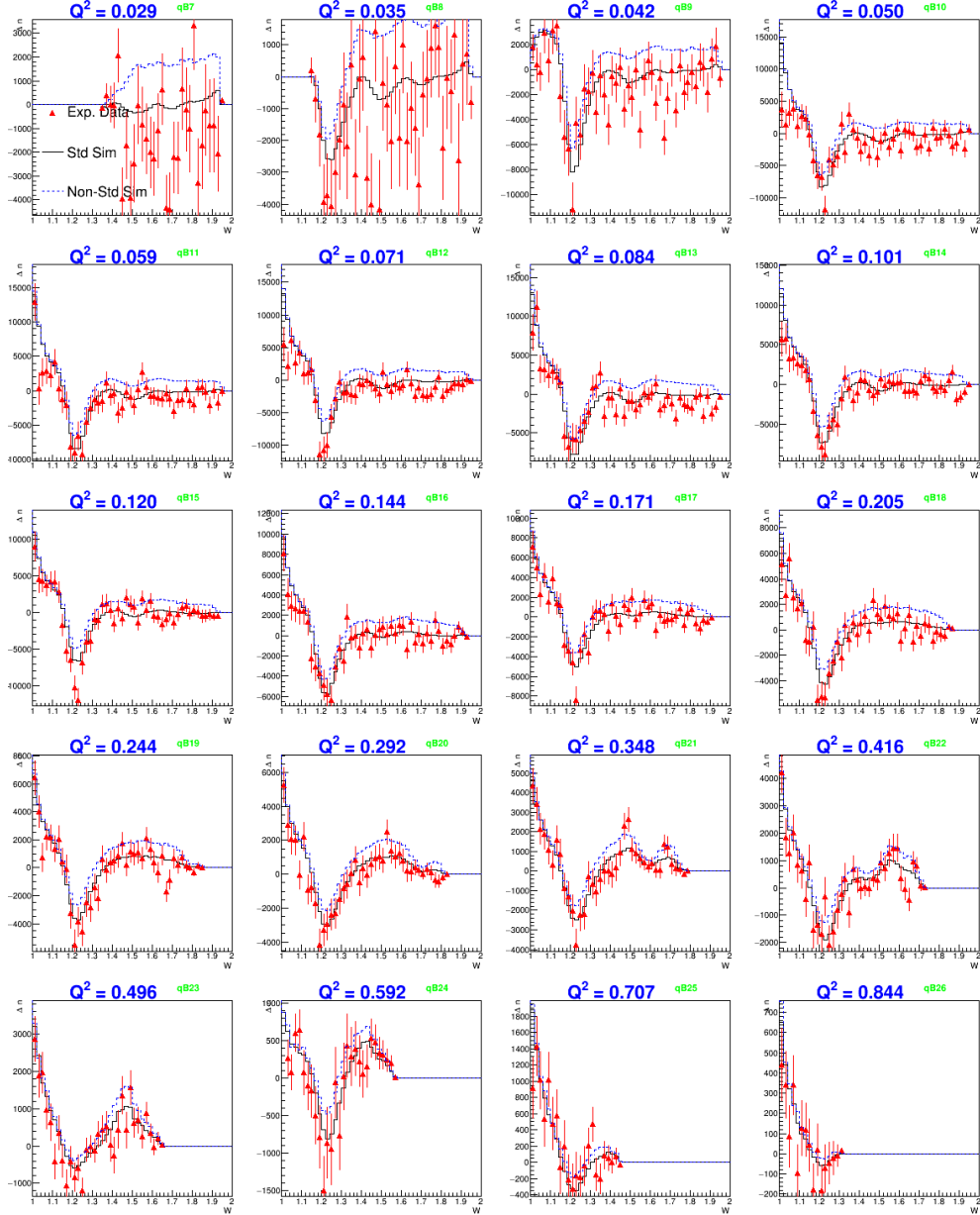


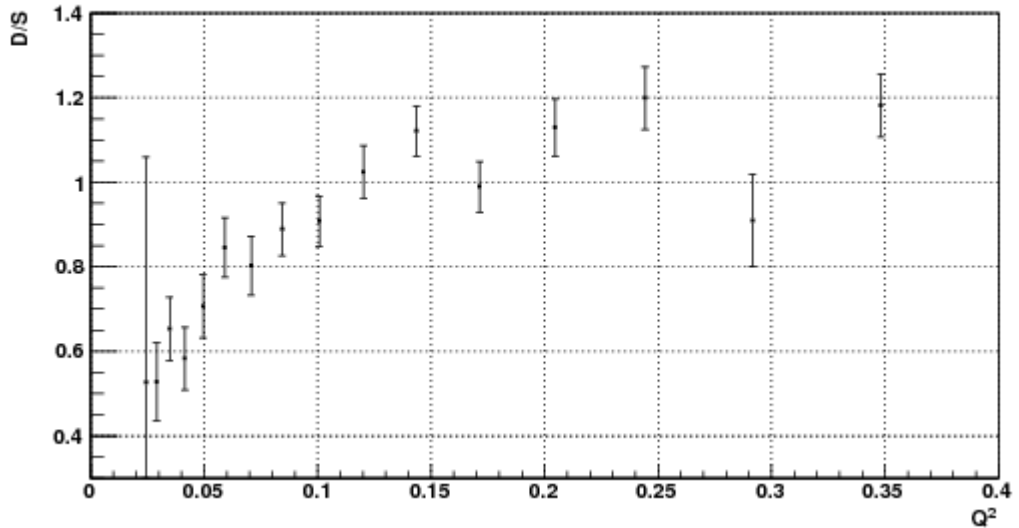
Figure 4.9: Comparison (in different Q^2 bins) of polarized count differences from 2.0 GeV experimental (red points with error bars) and two versions of normalized simulation data. The black continuous histograms are for “standard” simulation with values of A_1 set as given by the used model. The blue dotted histograms are for “non-standard” simulated data with A_1 changed to $A_1 + 0.1$.

1602 After this normalization, the ratios $(n^+ - n^-)/\Delta n(simul)$ in the quasi-
1603 elastic region for all Q^2 bins were calculated and plotted versus Q^2 as well as
1604 θ (see Figs. 4.10(a) - 4.13(a)) along with the corresponding statistical errors
1605 as given by $\sqrt{(n^+ + n^-)/\Delta n(simul)}$. As the figures show, the ratio in the
1606 quasi-elastic region drops off rapidly at small Q^2 . The fall-off is likely due
1607 to CC inefficiencies for very high momenta and very forward angles. Also,
1608 our simple cross section model for the deuteron is less accurate at low Q^2 .
1609 Figs. 4.10(b) - 4.13(b) show that the Δ -resonance region does not suffer
1610 from similar problems as the Delta model is quite reliable too (just like QE
1611 model).

1612 The final normalization was obtained by calculating the error weighted
1613 average $SF_{average}$ of above ratios in the quasi-elastic region. The average was
1614 calculated using only those Q^2 bins which had ratios reasonably stable and
1615 closer to each other. Because, the ratios are reasonably stable only above
1616 $Q^2 \approx 0.045 \text{ GeV}^2$ and $Q^2 \approx 0.09 \text{ GeV}^2$ in the 1.337 and 2.0 GeV data sets
1617 respectively (as can be seen from Figs. 4.10(a) and 4.12(a)), only those Q^2
1618 bins above these two limits were used in calculating the weighted average of
1619 these ratios. In addition, even above those two limits, some of those which
1620 had too large ratios - greater than 2.0 (or 2.5) for 1.337 (or 2.0) GeV data
1621 set- were not used in the weighted average. However, it should be noted that
1622 the bins not used in the average ratio calculations were not entirely discarded
1623 from the final analysis. Only those below $Q^2 = 0.02 \text{ GeV}^2$ were completely
1624 thrown out from the final analysis because they did not cover the resonance
1625 (particularly the Δ) region very well. The resulting simulated data in the
1626 form of count differences Δn in various Q^2 bins are shown in Figs. 4.8 and
1627 4.9 along with the corresponding experimental data.

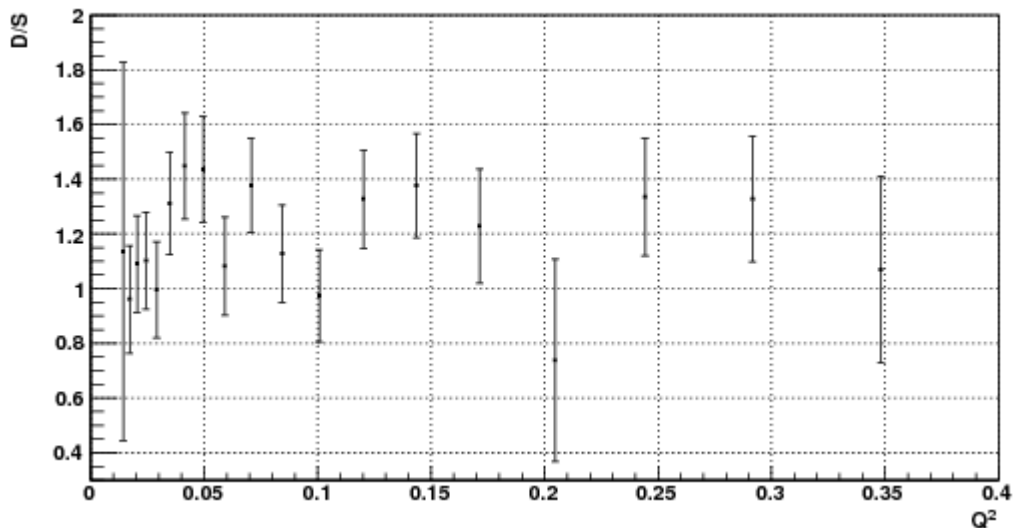
1628 A complete systematic error analysis was done to study the effect of the
1629 overall scaling factor SF on the extracted g_1 (see below) and to estimate
1630 its statistical (due to the number of counts) and systematic (due to model
1631 uncertainties and backgrounds) error.

Data/Sim for W(0.9,1.05)



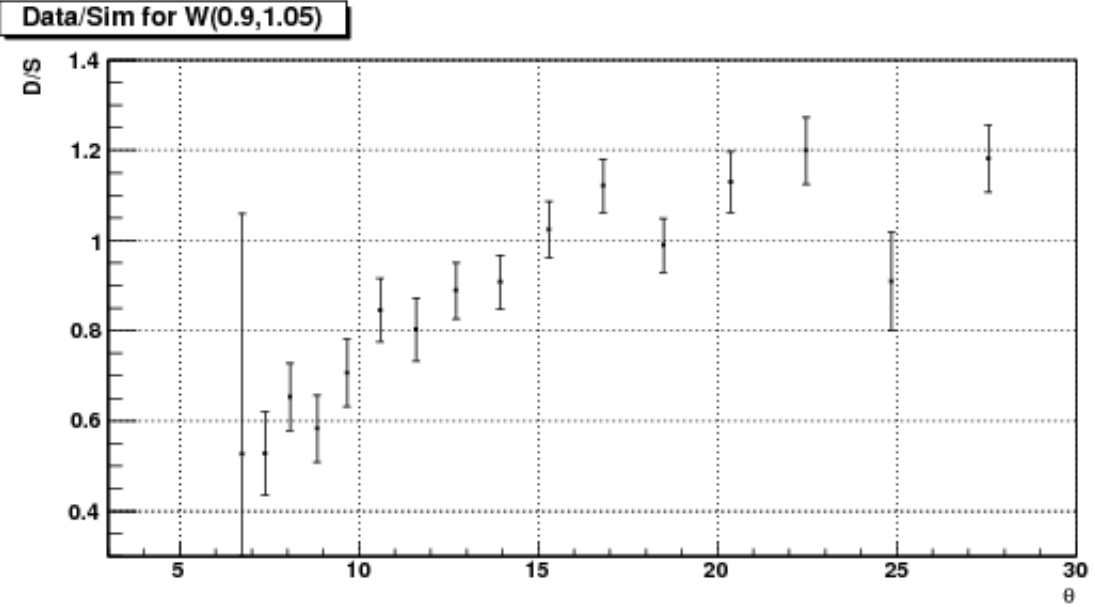
(a) Data/Sim ratio vs Q^2 in 1.3 GeV quasi-elastic data.

Data/Sim for W(1.15,1.3)

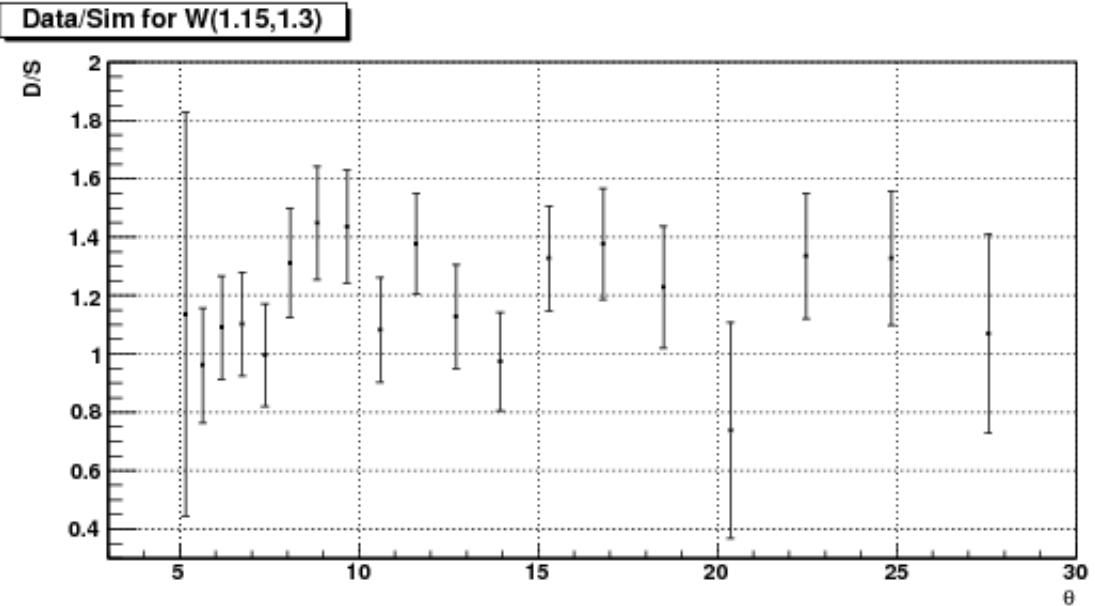


(b) Data/Sim ratio vs Q^2 in Δ -resonance region of 1.3 GeV data.

Figure 4.10: Q^2 dependence of ratios of 1.3 GeV data and simulation in the quasi-elastic and Δ -resonance regions.

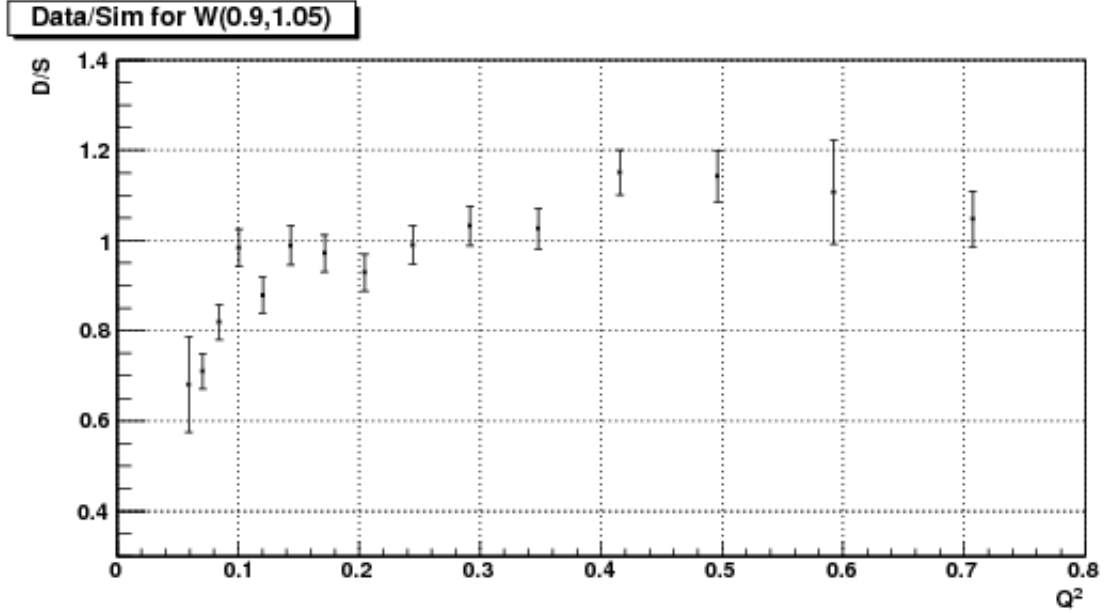


(a) Data/Sim ratio vs θ in 1.3 GeV quasi-elastic data.

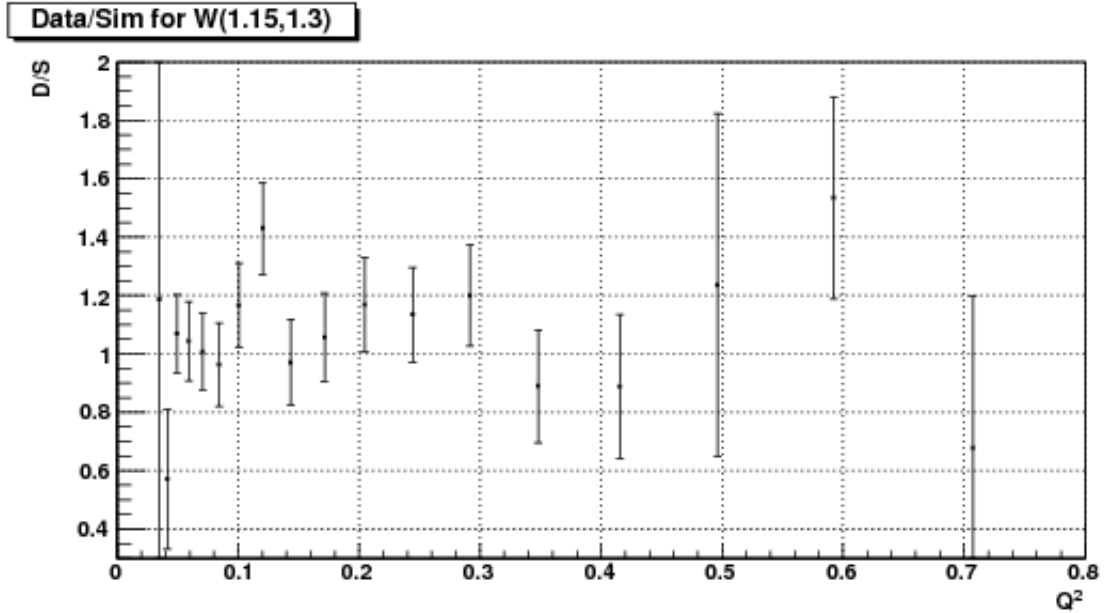


(b) Data/Sim ratio vs θ in Δ -resonance region of 1.3 GeV data.

Figure 4.11: The same data as in Fig. 4.10, but plotted versus average scattering angle (θ). Here we can see that the data for $\theta > 10^{\circ}$ are reasonably stable with $\pm 10\%$ fluctuation (which will be taken into account while calculating the systematic uncertainty later).

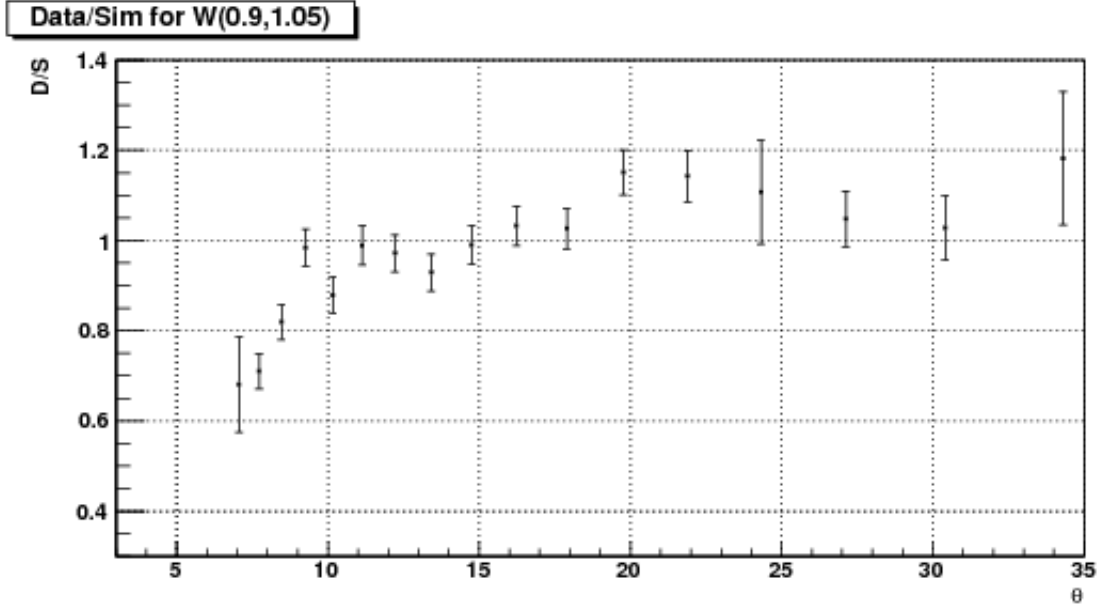


(a) Data/Sim ratio vs Q^2 in 2.0 GeV quasi-elastic data.

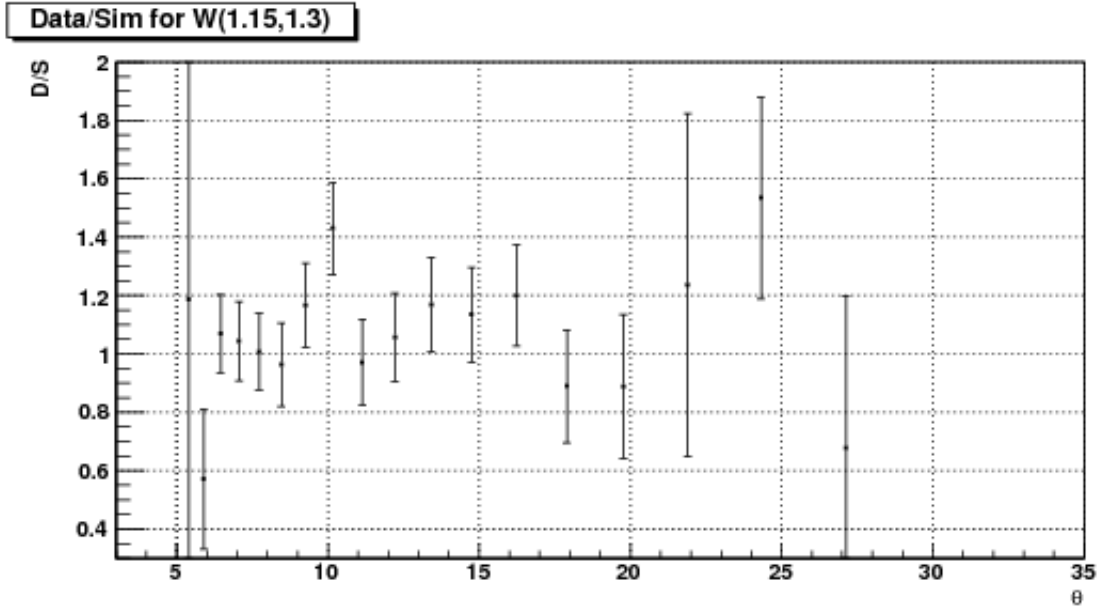


(b) Data/Sim ratio vs Q^2 in Δ -resonance region of 2.0 GeV data.

Figure 4.12: Q^2 dependence of ratios of 2.0 GeV data and simulation in the quasi-elastic and Δ -resonance regions.



(a) Data/Sim ratio vs θ in 2.0 GeV quasi-elastic data.



(b) Data/Sim ratio vs θ in Δ -resonance region of 2.0 GeV data.

Figure 4.13: The same data as in Fig. 4.12, but plotted versus average scattering angle (θ). Here we can see that the data for $\theta > 10^{\circ}$ are reasonably stable with $\pm 10\%$ fluctuation (which will be taken into account while calculating the systematic uncertainty later).

1633 4.5 Method to Extract g_1 and $A_1 F_1$

1634 4.5.1 ‘Variation’ of the standard simulation

The whole chain of steps outlined in the previous sections for the standard simulation is repeated with just one major difference: the model input for the asymmetries A_1 for both the proton and the neutron are increased by a constant value⁶ of 0.1. With all other model ingredients being kept constant, this change leads to a change of the spin structure function g_1 that can be straightforwardly calculated for each kinematic bin within the model:

$$\delta g_1(W, Q^2) = \delta A_1 \times F_1 \frac{\nu^2}{\nu^2 + Q^2} \quad (4.5)$$

1635 Correspondingly, the simulated count difference $\Delta n(W, Q^2)$ will change to
 1636 a new value $\Delta n'$. This ‘non-standard’ simulation with $A_1 = A_1(\text{standard}) +$
 1637 0.1 is performed generating an about equal number of Monte-Carlo events.
 1638 The final reconstructed data is then multiplied with the same overall scaling
 1639 factor SF as for the standard simulation and then further (cross-)normalized
 1640 by one additional factor $SF_{ext} = (\sigma_1^p / \sigma_2^p) / (N_1 / N_2)$ to account for the change
 1641 in cross section map and the (slight) difference in the number of the generated
 1642 events between the standard and non-standard simulations. Here, σ_1^p and σ_2^p
 1643 are the total cross sections for the positive $\Delta\sigma$ maps used for the standard and
 1644 non-standard simulations and, N_1 and N_2 are the corresponding numbers of
 1645 generated events. See Fig. (4.14) to see how the polarized count differences
 1646 look (in one particular Q^2 bin) in experimental and simulated data after such
 1647 normalizations (for all other Q^2 bins, see Figs. 4.8 and 4.9).

This change of the simulated $\Delta n(W, Q^2)$ to a new value $\Delta n'$ can be correlated to the increase in g_1 by solving for the two parameters A and B of the linear equation,

$$\Delta n(\text{simul}) = A + B \cdot \delta g_1, \quad (4.6)$$

where $A(W, Q^2)$ is the result for the simulated Δn for the standard set of model inputs i.e., $A(W, Q^2) = \Delta n^{\text{standard}}(W, Q^2)$, and $B(W, Q^2)$ is the proportionality factor representing the change in $\Delta n(\text{sim})$ per unit change in

⁶We arbitrarily chose 0.1 in the inelastic region, but could also have used any other value (not too big, however).

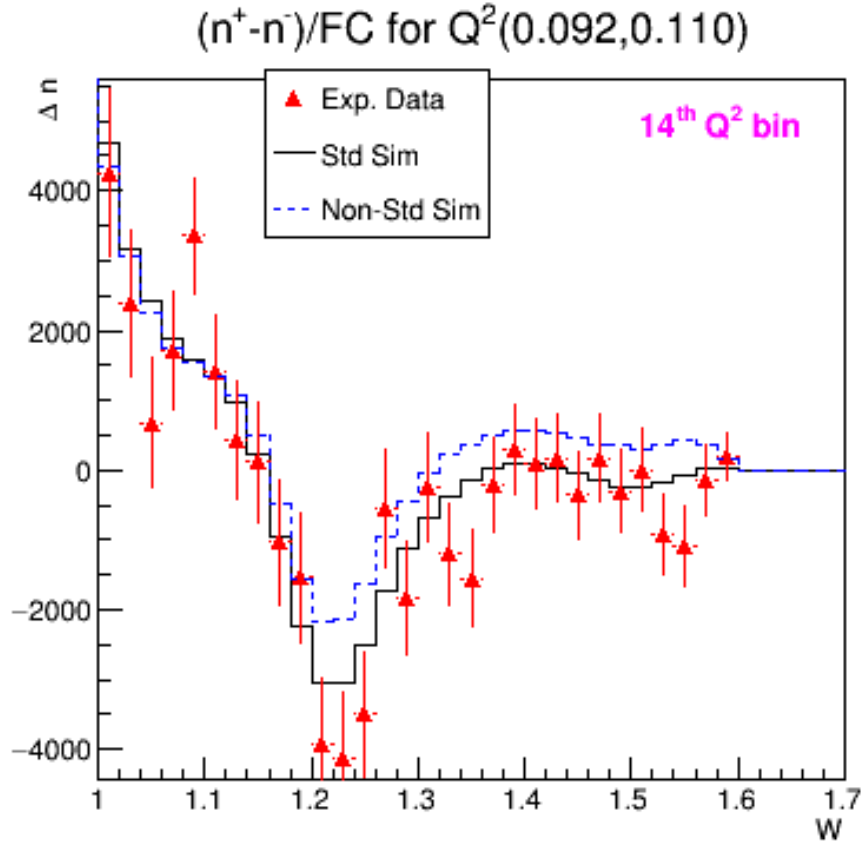


Figure 4.14: Δn of experimental data and two versions of simulations in one particular Q^2 bin for 1.3 GeV case (for data on more Q^2 bins, see Fig. 4.8).

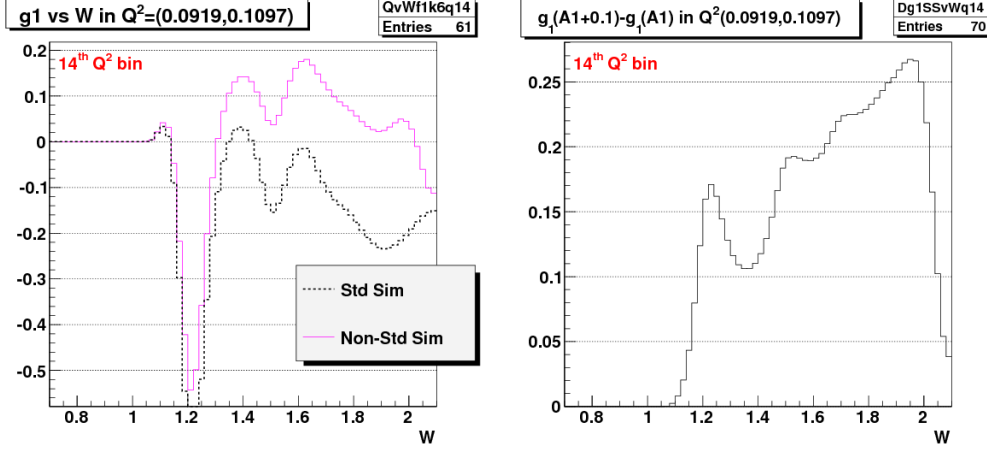
g_1 , as given by:

$$B(W, Q^2) = \frac{\Delta n' - \Delta n}{\delta g_1}. \quad (4.7)$$

Similarly, in case of $A_1 F_1$ evaluation, the factor is given by:

$$B(W, Q^2) = \frac{\Delta n' - \Delta n}{\delta A_1 F_1}. \quad (4.8)$$

1648 The proportionality factor $B(W, Q^2)$ is then determined for each of the
 1649 kinematic bins (in (W, Q^2)) in which the experimental data has been his-
 1650 togrammed. For this purpose, using the RCSLACPOL program, we produce
 1651 two values of structure function g_1 in each kinematic bin - one is $g_1^{Standard}$



(a) g_1 for standard and non-standard simulation

(b) Difference of the two g_1

Figure 4.15: Plots showing the change in model g_1 due to the change of A_1 to $A_1 + 0.1$.

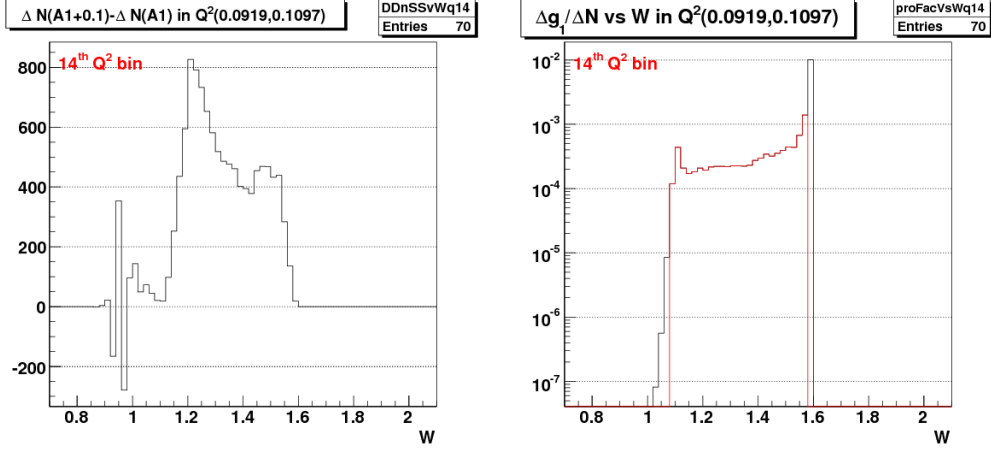
corresponding to the standard simulation and the other is $g_1^{non-standard}$ corresponding to the non-standard simulation. By dividing the above change in the count difference with the difference Δg_1 of these two structure functions, we get the factor $B(W, Q^2)$ for the bin. The similar procedure is followed to get the corresponding values of $B(W, Q^2)$ in the case of $A_1 F_1$ evaluation.

In principle (and ignoring the other enumerated possible sources of disagreement between data and simulation), we can then easily find the “amount of change” δg_1 to be added to the standard model g_1 to get perfect agreement:

$$\delta g_1 = g_1^{extr}(W, Q^2) - g_1^{Standard} = \frac{\Delta n^{data}(W, Q^2) - \Delta n^{standard}(W, Q^2)}{B(W, Q^2)} \quad (4.9)$$

where the values of Δn^{data} and $\Delta n^{standard}$ come from the polarized count differences Δn in the experimental data and the standard simulation respectively (as shown, for example, by the red points and black histograms in Fig. 4.14 for one particular Q^2 bin).

It is also straightforward to propagate the statistical uncertainty to the extracted g_1 . The statistical uncertainty in this extracted quantity totally comes from the uncertainty in the experimental counts Δn^{data} (assuming



(a) Change in $\Delta n(sim)$ simulated count difference i.e. $\Delta N = \Delta n'(A_1 + 0.1) - \Delta n(A_1)$ due to the change of A_1 to $A_1 + 0.1$ (for 1.3 GeV case).

(b) Proportionality factor ($1/B(W, Q^2)$) for 1.3 GeV case. Black is the original values. Red is the ones kept after discarding the first or last few (low statistics bins) that had unreasonably high (suddenly changing) ratios. This ensures we only show final data with “good” proportionality factor.

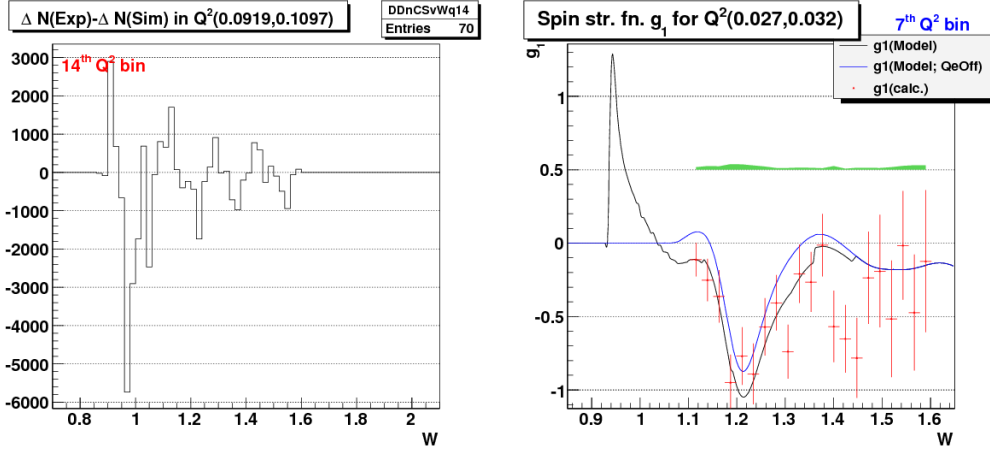
Figure 4.16: Plots for $\Delta n(sim)$ and the corresponding proportionality factors.

there is no uncertainty in the model quantities involved and also in the simulation counts because we did our simulation with large enough statistics to warrant ignoring the uncertainties) as follows:

$$\sigma(g_1^{extr}(W, Q^2)) = \frac{\sigma(\Delta n^{data}(W, Q^2))}{B(W, Q^2)}. \quad (4.10)$$

1661 The values of g_1 and its uncertainties thus extracted from 1.3 GeV data
 1662 for one Q^2 bin is shown in Fig. (4.17(b)). Similar results for all the bins
 1663 from two beam energy data sets in different kinematic bins can be seen in
 1664 Fig. 6.1.

1665 Because we are also interested in measuring the forward spin polarizability and the extended GDH integral, we also extract the product $A_1 F_1$ which
 1666 enters these integrals. We followed the exact same procedure for g_1 as outlined above. We determined new proportionality factors in each kinematic
 1667 bin, again using Eq. 4.12 as before but with the denominator replaced, this
 1668 time, with the corresponding change in $A_1 F_1$ (instead of the change in g_1).
 1669



(a) Difference $\Delta n(data) - \Delta n(sim)$ (for 1.3 GeV case).

(b) Calculated g_1 from 1.3 GeV data.

Figure 4.17: Plots for $\Delta(\Delta n)$ and the corresponding extracted g_1 . On the left, Δn are the normalized count differences from the experimental and simulated (using 'standard' model) data. On the right, the blue line is that of g_1 when the quasi-elastic part was turned off in the model that was used in simulation. We used $g_1^{extracted} = g_1^{q.e.Off} + \delta g_1$ to get the measured g_1 , where δg_1 was derived from the data shown on the left using Eq. 4.9.

1671 Then we can use the following expression (similar to equation 4.9) to extract
 1672 $A_1 F_1(W, Q^2)$:

$$\delta A_1 F_1 = A_1 F_1^{extr}(W, Q^2) - A_1 F_1^{Standard} = \frac{\Delta n^{data}(W, Q^2) - \Delta n^{standard}(W, Q^2)}{B_{A_1 F_1}(W, Q^2)} \quad (4.11)$$

where

$$B_{A_1 F_1}(W, Q^2) = \frac{\Delta n' - \Delta n}{\delta A_1 F_1}. \quad (4.12)$$

1673 And, the uncertainties on $A_1 F_1$ can also be dealt in the same way as on
 1674 g_1 .

₁₆₇₅ **Chapter 5**

₁₆₇₆ **Systematic Uncertainties**

₁₆₇₇ There is always a possibility that the final result(s) produced from any data
₁₆₇₈ analysis will be shifted from the true or ideally expected value(s) because the
₁₆₇₉ final result(s) are derived using the measured, modeled or estimated values
₁₆₈₀ of one or more other input parameters, whose values themselves usually have
₁₆₈₁ some systematic measurement or estimation uncertainties.

₁₆₈₂ The systematic effects due to a particular variable are studied by making a
₁₆₈₃ small change in the variable while holding the others constant, and measuring
₁₆₈₄ by how much the end result(s) changed.

₁₆₈₅ In this analysis, ten sources of systematic uncertainties are studied as
₁₆₈₆ listed below:

- ₁₆₈₇ 1. Possible Uncertainty in the overall scaling factor
- ₁₆₈₈ 2. Effect due to the contaminations from polarized H in the target and
₁₆₈₉ from misidentified π^- in the scattered electrons sample.
- ₁₆₉₀ 3. Potential deviations in the reconstructed kinematics
- ₁₆₉₁ 4. Possible uncertainty in the CC-inefficiency estimation
- ₁₆₉₂ 5. Effect due to the e^+e^- pair symmetric contamination
- ₁₆₉₃ 6. Possible uncertainty in the estimation of radiation lengths
- ₁₆₉₄ 7. Model variation using preliminary version (v1) of A_1 model by Guler/Kuhn
₁₆₉₅ (2008-9)
- ₁₆₉₆ 8. Model variation using old version of A_2 resonance model

1697 9. Model variation of F_2 (and proportionally of F_1) while keeping R con-
1698 stant

1699 10. Model variation of R or F_1 (with F_2 unchanged)

1700 For the ease of description later on, these ten components will be referred to
1701 by the index "k" with its value indicating the position in the list. So, the
1702 uncertainty due to scaling factor will be identified with k=1 and so on.

1703 5.1 Evaluation of Experimental Systematics

Possible Uncertainty due to the overall scaling factor This uncer-
tainty is due to the uncertainties in the overall scaling factor (SF), which is a
convolution of various unmeasured constants such as $P_b P_t$, packing fraction
etc (see Sec. 4.1.1). This contribution is estimated by assuming that the
uncertainties in SF is not more than 10%. Thus considering the worst case
scenario of 10% uncertainty in SF, we estimate the corresponding uncertainty
in g_1 as follows:

$$\Delta g_1^{SF}(W, Q^2) = g_1^{std}(W, Q^2) + \frac{\Delta n^{data}(W, Q^2) - 1.1 \cdot \Delta n^{std}(W, Q^2)}{1.1 \cdot B(W, Q^2)} - g_1^{data}(W, Q^2) \quad (5.1)$$

1704 with "std" shorthand used for "standard" model or the corresponding sim-
1705 ulation i.e. the ones provided by RCSLACPOL when the asymmetry A_1
1706 was not artificially increased to $A_1 + 0.1$. Here, Δn^{data} and Δn^{std} represent
1707 the polarized count differences for the experimental and simulated (without
1708 artificially changing A_1) data respectively.

Uncertainty from Polarized H in target and π^- contaminations This
contribution from polarized H in target and π^- contamination is evaluated as
follows,

$$\Delta g_1^{cont}(W, Q^2) = g_1^{std}(W, Q^2) + \frac{\Delta n^{data}(W, Q^2) \cdot 1.025 - \Delta n^{std}(W, Q^2)}{B(W, Q^2)} - g_1^{data}(W, Q^2) \quad (5.2)$$

1709 where we assume that the contamination is not more than 2.5%, which is
1710 consistent with what was found from our own study of the contamination.

Possible uncertainty in the beam energy measurement This contribution is evaluated assuming the uncertainty in beam energy measurement is not more than 10 MeV, so either the experimental data or the standard-simulation data can be analyzed assuming the beam energy was different by 10 MeV. In this analysis, the simulated data was analyzed assuming that the beam energy was 10 MeV more than that used during the event generation or simulation which was the same as that used for analyzing the experimental data. For example, for the lower beam energy data set, 1339 MeV was used to analyze the experimental data as well as to simulate the corresponding data, but during the analysis of the simulated data, the energy value used was 1349 MeV. Here, the change in energy results in changes in both Q^2 and W .

$$\Delta g_1^{Eb}(W, Q^2) = g_1^{std}(W, Q^2) + \frac{\Delta n_{Eb+}^{data}(W, Q^2) - \Delta n_{Eb+}^{std}(W, Q^2)}{B(W, Q^2)} - g_1^{data}(W, Q^2) \quad (5.3)$$

1711 where Δn_{Eb+}^{std} is now the simulated Δn^{std} obtained by analyzing the data
 1712 from the standard simulation as usual but with a beam energy that was 10
 1713 MeV more than the standard value.

Possible uncertainty in the CC-inefficiency estimation This contribution is estimated by assuming a maximum of 50% uncertainty in the estimated inefficiency as follows: The the 50% error is justified because the uncertainty in inefficiency is no more than 50% for $nphe > 2.5$ (see Fig. 3.30).

$$\Delta g_1^{Eb}(W, Q^2) = g_1^{std}(W, Q^2) + \frac{\Delta n_{0.5CCi}^{data}(W, Q^2) - \Delta n_{0.5CCi}^{std}(W, Q^2)}{B(W, Q^2)} - g_1^{data}(W, Q^2) \quad (5.4)$$

1714 where $\Delta n_{0.5CCi}^{std}$ is now the simulated Δn^{std} obtained after applying 50% more
 1715 inefficiency instead of the actually estimated value.

Possible uncertainty due to e^+e^- pair symmetric contamination The contribution due to e^+e^- pair symmetric contamination is calculated as follows:

$$\Delta g_1^{Eb}(W, Q^2) = g_1^{std} + \frac{\Delta n^{data} \cdot \frac{1}{1+f(e^+e^-)} - \Delta n^{std}}{B(W, Q^2)} - g_1^{data}(W, Q^2) \quad (5.5)$$

1716 where $f(e^+e^-)$ is the fraction of electrons in a given bin that come from pair-
1717 symmetric e^+e^- produced as estimated with EG1b fit by N. Guler [20] (used
1718 the closest available energies).

Radiative correction uncertainty Here, we need to change the parameter that most influences radiative corrections, the number of radiation lengths before (RADB) and after (RADA) the scattering. By increasing both numbers by 10%, we should have a safe upper limit on practically all uncertainties coming from the radiative procedure itself. But, to simplify the situation, we increased the RADA parameter in RCSLACPOL by 20% and repeated the full-statistic simulation. As a result the simulated count difference in each kinematic bin changed from Δn^{std} to a new value Δn^{rad} . This change can be converted to the corresponding inferred change in g_1 by using the same proportionality factors $B(W, Q^2)$ as used earlier in the g_1 (or $A_1 F_1$) extraction/calculation. In other words, for a given kinematic bin this particular contribution to the systematic uncertainty is calculated as:

$$\Delta g_1^{rad}(W, Q^2) = g_1^{std} + \frac{\Delta n^{data}(W, Q^2) - \Delta n^{rad}(W, Q^2)}{B(W, Q^2)} - g_1^{data}(W, Q^2) \quad (5.6)$$

1719 where the proportionality factor $B(W, Q^2)$ for the bin is exactly the same as
1720 that used to calculate g_1 earlier.

1721 5.2 Model uncertainties

1722 The remaining four components in the total systematic uncertainty (the last
1723 four in the list 5) account for the model uncertainty contributions. For this
1724 purpose, we changed the values of two of the model parameters “Asym-
1725 Choice” and “SFchoice” (each takes value of 11, in the standard case)

1726 We repeated the full statistics simulation four more times by changing
1727 the values of two RCSLACPOL parameters “AsymChoice” and “SFchoice”
1728 (which controls the values of model asymmetries and the structure functions,
1729 with each taking a value of 11 in the standard case) one by one corresponding
1730 to the following four model variations:

- 1731 1. Variation-1: AsymChoice=12, SFchoic=11
- 1732 2. Variation-2: AsymChoice=15, SFchoic=11

1733 3. Variation-3: AsymChoice=11, SFchoic=12

1734 4. Variation-4: AsymChoice=11, SFchoic=13

1735 where, the different values of the two RCSLACPOL parameters correspond
1736 to the following model choices:

1737 1. **AsymChoice** values are used to determine specific A_1/A_2 models used
1738 in the RCSLACPOL program

1739 (a) 11: Standard Resonance Model 2008-9 Guler/Kuhn (**Used for**
1740 **standard simulation**)

1741 (b) 12: Variation of A_1 model (earlier fit)

1742 (c) 15: Variation of A_2 resonance model: Vary the virtual photon
1743 asymmetry A_2 in the resonance region within its fit uncertainties.

1744 2. **SFchoice** values are used to determine specific F_1/F_2 models.

1745 (a) 11: 2009 version of $F_1^n/F_1^p/F_1^d$ by Peter Bosted/Eric Christie 2009,
1746 **HERMES (Used for standard simulation)** (with d in F_1^d de-
1747 noting a deuteron).

1748 (b) 12: Same version as 11, but with fit uncertainties added to F_2
1749 (and proportionally F_1)

1750 (c) 13: Same version as 11, but with fit uncertainties subtracted from
1751 R (F_2 unchanged)

After the simulation data for the above four cases (see 5.2) were available, four more data tables (TM1,TM2,TM3 and TM4) were produced for the corresponding model values of g_1 , A_1 , F_1 etc. Then, the contributions to the systematic uncertainty from each of these four cases of model variation were given as follows:

$$\Delta g_1^i(W, Q^2) = g_1^{std}(W, Q^2) - g_1^i(W, Q^2) + \frac{\Delta n^i(W, Q^2) - \Delta n^{std}(W, Q^2)}{B(W, Q^2)} \quad (5.7)$$

1752 with “i” indicating any of the four cases of model variation, g_1^i being the
1753 model prediction for the i^{th} case as obtained from the corresponding data
1754 table “TMi” and the proportionality factor $B(W, Q^2)$ again being exactly
1755 the same as used to calculate g_1 as earlier.

5.3 Combining uncertainties

Contributions from the 10 individual components are estimated and then a total contribution is estimated by first combining the corresponding individual components for each of the two beam energies and finally combining them all by calculating the RMS of the ten combined contributions.

5.3.1 Combining uncertainties from the two beam energies

In principle, each of the individual contributions to the systematic uncertainty can also be combined using the same equations as for combining g_1 and $A_1 F_1$ (see above). However, we must be careful to distinguish between correlated and uncorrelated uncertainties. If for a given (W, Q^2) bin, data is available only from one beam energy, then combined uncertainty for the k^{th} component is simply the uncertainty from that beam energy. If there are measurements from both beam energies, we combine them with statistical weights as follows:

1. The variations due to scale factor ($k=1$), beam energy ($k=3$) and CC-efficiency ($k=4$) are all un-correlated and, therefore, added in quadrature as follows:

$$\delta g_1(k=8,10,11, \text{combined}) = \sqrt{\left(\sum_i \frac{(\delta g_1)^2(i)}{(\Delta g_1)^2(i)} \right) / \text{Sum2}} \quad (5.8)$$

where, δ represents the k^{th} component of the systematic uncertainty, whereas, 'Sum2', 'i' and Δ have the same meanings as before, with 'Sum2' given by

$$\text{Sum2} = \sum_i \frac{1}{(\Delta g_1)^2(i)} \quad (5.9)$$

which provides the statistical weight, where the index 'i' represents two beam energy (1.3 and 2.0 GeV) data sets, and Δg_1 indicates the statistical uncertainty in g_1 in the corresponding kinematic bin.

- 1780 2. All other variations are correlated between the two beam energies and
 1781 should be averaged linearly (WITH sign):

$$\delta g_1(\text{other } k, \text{ combined}) = \left(\sum_i \frac{(\delta g_1)(i)}{(\Delta g_1)^2(i)} \right) / \text{Sum2} \quad (5.10)$$

1782 5.3.2 Combining uncertainties from the ten sources

1783 Once each of the k^{th} component of the systematic uncertainties are combined
 1784 between the two beam energies, we then proceed to combine them all to get
 1785 a grand total. This is done by simply adding the ten E_b -combined systematic
 1786 uncertainties in quadrature and taking the square-root of the sum as follows:

$$\text{Total Systematic Uncertainty} = \sqrt{\sum_{k=1}^{10} (\Delta g_1)_k^2} \quad (5.11)$$

1787 Figs. (5.2 and 5.3) show, for example, the different components of the
 1788 systematic uncertainties along with the grand total on g_1 (from 1.3 GeV
 1789 data) evaluated in the manner just outlined. Likewise, Figs. (5.4 and 5.5)
 1790 show similar plots for the 2.0 GeV data.

1791 These ten different components of systematic uncertainties on g_1 and
 1792 similarly on $A_1 F_1$ thus calculated separately for both beam energies are later
 1793 combined as described below.

1794 5.3.3 Combining data from the two beam energies

1795 Once the data g_1 and $A_1 F_1$ and their corresponding uncertainties are eval-
 1796 uated from each beam energy data set, they are combined as follows [25] (to
 1797 make the description simple, the procedure is described only for g_1 , but, in
 1798 the end, the exact same procedure is followed for $A_1 F_1$ as well):

- 1799 1. First a table is made, separately for each beam energy, of all (Q^2, W)
 1800 bins with calculated values of g_1 , their statistical uncertainties and each
 1801 of the ten components of the systematic uncertainties (making sure to
 1802 keep the correct signs of the systematic changes).
- 1803 2. Then another table is made for the combined values of g_1 , which are
 1804 evaluated as follows:

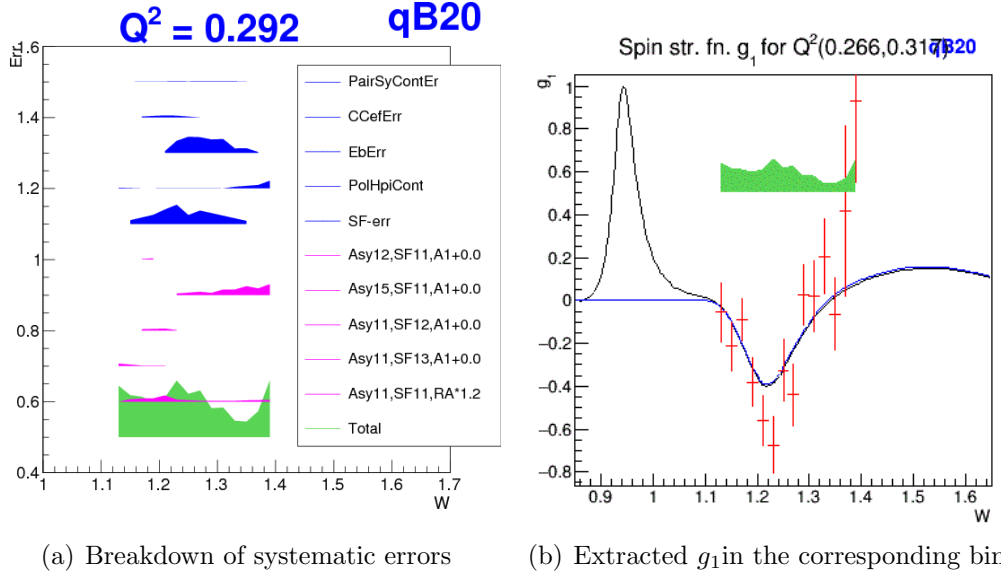


Figure 5.1: On the left: various components of systematic uncertainty (see Sec. 5 on g_1 plotted against W in a Q^2 bin (1.3 GeV data). The band width represents the size of the uncertainties. The vertical position of each band has no physical meaning (arbitrarily chosen for the convenience of display). The first five (blue) bands are the contributions due to e^+e^- -contamination , CC-inefficiency , uncertainties in beam energy measurement , polarized background (H, π^- etc) and scaling factor uncertainties respectively. The first (top) magenta band is the contribution due to the uncertainties in the radiative corrections , next four (magenta) are due to model uncertainties and the last (green) one is the total uncertainty after properly combining all components. For similar plots in other Q^2 bins see Figs. 5.2 and 5.3. On the right: extracted g_1 vs W shown along with the total systematic uncertainty.

- 1805 (a) If for a given (W, Q^2) bin, g_1 comes only from one beam energy,
1806 then all the entries from that energy go into the "combined" table
- 1807 (b) If g_1 has measurements from both beam energies, we combine
1808 them with statistical weights as follows:

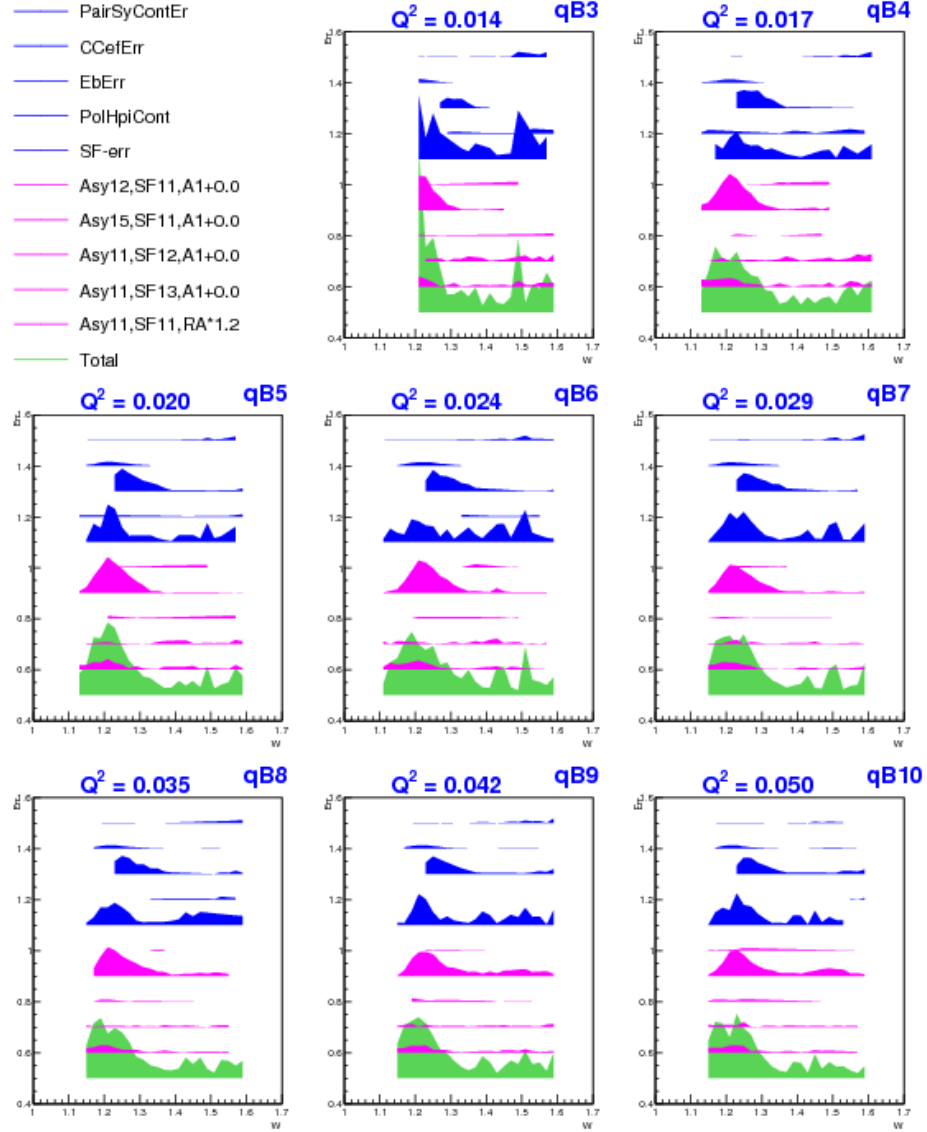


Figure 5.2: Plots like that shown in Fig. 5.1 showing various components of systematic uncertainty on g_1 plotted against W in different Q^2 bins for 1.3 GeV data.

$$Sum1 = \sum_i \frac{g_1(i)}{(\Delta g_1)^2(i)} \quad (5.12)$$

$$g_1(\text{combined}) = Sum1/Sum2 \quad (5.13)$$

$$\sigma g_1(\text{combined}) = \sqrt{1/Sum2} \quad (5.14)$$

1809 where the index 'i' represents two beam energy (1.3 and 2.0 GeV)
 1810 data sets, Δg_1 indicates the statistical uncertainty in g_1 and *Sum2*
 1811 is again given by Eq. 5.12 above..

- 1812 3. In principle, each of the individual contributions to the systematic un-
 1813 certainty can also be combined using the same equations. However,
 1814 we must be careful to distinguish between correlated and uncorrelated
 1815 uncertainties.
 1816 (a) The variations due to scale factor ($k=1$), beam energy ($k=3$) and
 1817 CC-efficiency ($k=4$) are all un-correlated and, therefore, added in
 1818 quadrature as follows:

$$\delta g_1(k=1,3,4, \text{ combined}) = \sqrt{\left(\sum_i \frac{(\delta g_1)^2(i)}{(\Delta g_1)^2(i)} \right) / \text{Sum2}} \quad (5.15)$$

1819 where, δ represents the k^{th} component of the systematic un-
 1820 certainty, whereas, 'Sum2', 'i' and Δ have the same meanings as
 1821 before.

- 1822 (b) while all other variations are correlated between the two beam
 1823 energies and should be averaged with linear weighting (WITH
 1824 sign):

$$\delta g_1(\text{other } k, \text{ combined}) = \left(\sum_i \frac{(\delta g_1)(i)}{(\Delta g_1)^2(i)} \right) / \text{Sum2} \quad (5.16)$$

- 1825 4. Once each of the k^{th} component of the systematic uncertainties are
 1826 combined between the two beam energies, we then proceed to combine
 1827 them all to get a grand total. This is done by simply adding the
 1828 ten combined systematic uncertainties in quadrature and taking the
 1829 square-root.

1830 Figures 5.6 and 5.8 show the breakdown of the total contribution to the
 1831 systematic uncertainty from different sources. We can see that the dominant
 1832 contribution comes from the uncertainties in the overall scale factor (the cyan
 1833 band indicated with SF-err in the legend) which is used to normalize the sim-
 1834 ulated data to make them comparable with data. One of the big part of this
 1835 uncertainty comes from those in $P_b P_t$ and target size measurements. Next

1836 big contributions seem to come from the model (in particular the model for
1837 the unmeasured A_2) and radiative corrections. Near the Δ -resonance region,
1838 the effect of beam energy uncertainty also seems to be very pronounced. The
1839 breakdown of the different components (but combined between the two beam
1840 energies) of the total systematic uncertainties are also shown separately in
1841 the Figs. 5.6 and 5.8.

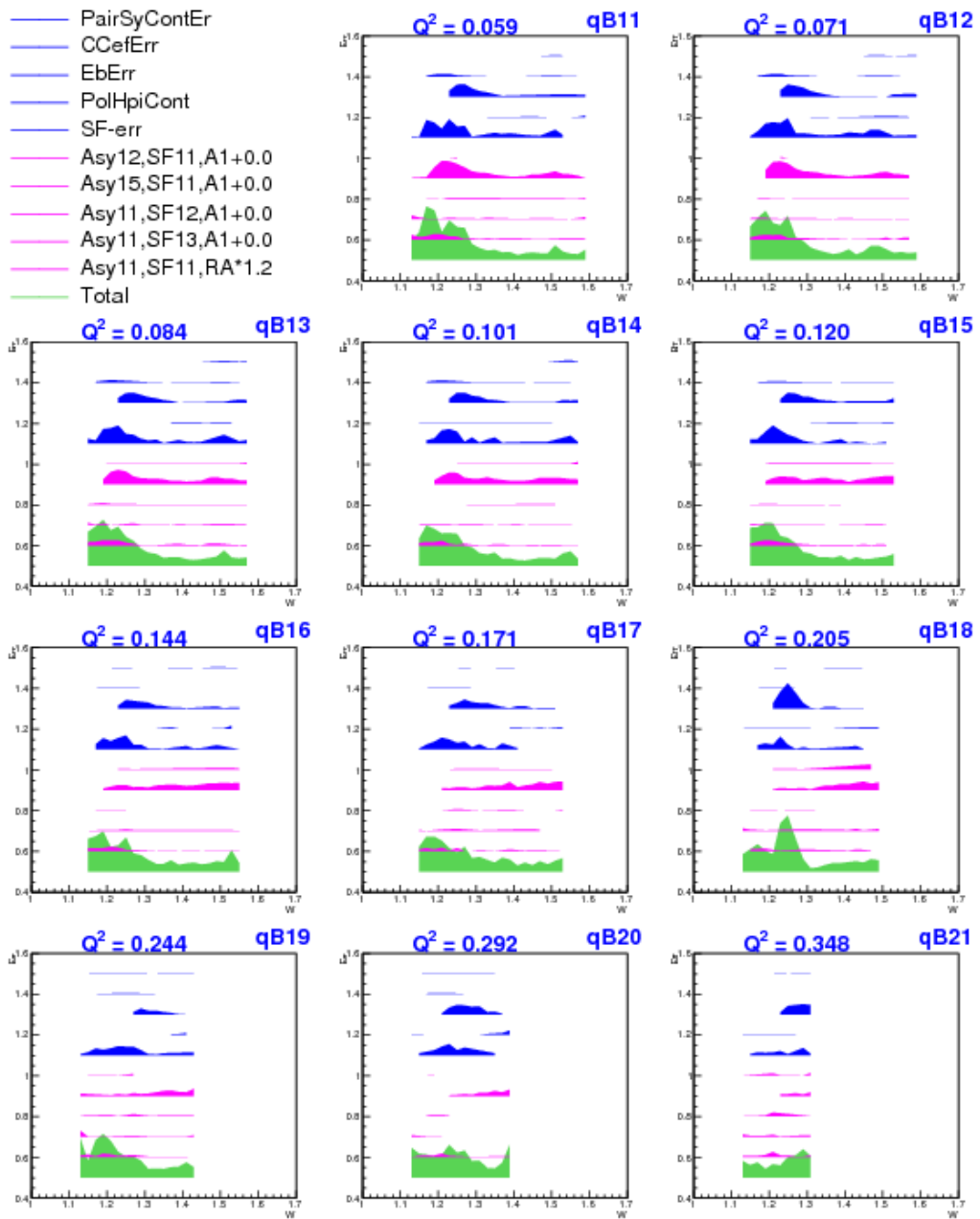


Figure 5.3: Systematic uncertainty components in remaining Q^2 bins (continuation of Fig. 5.2).

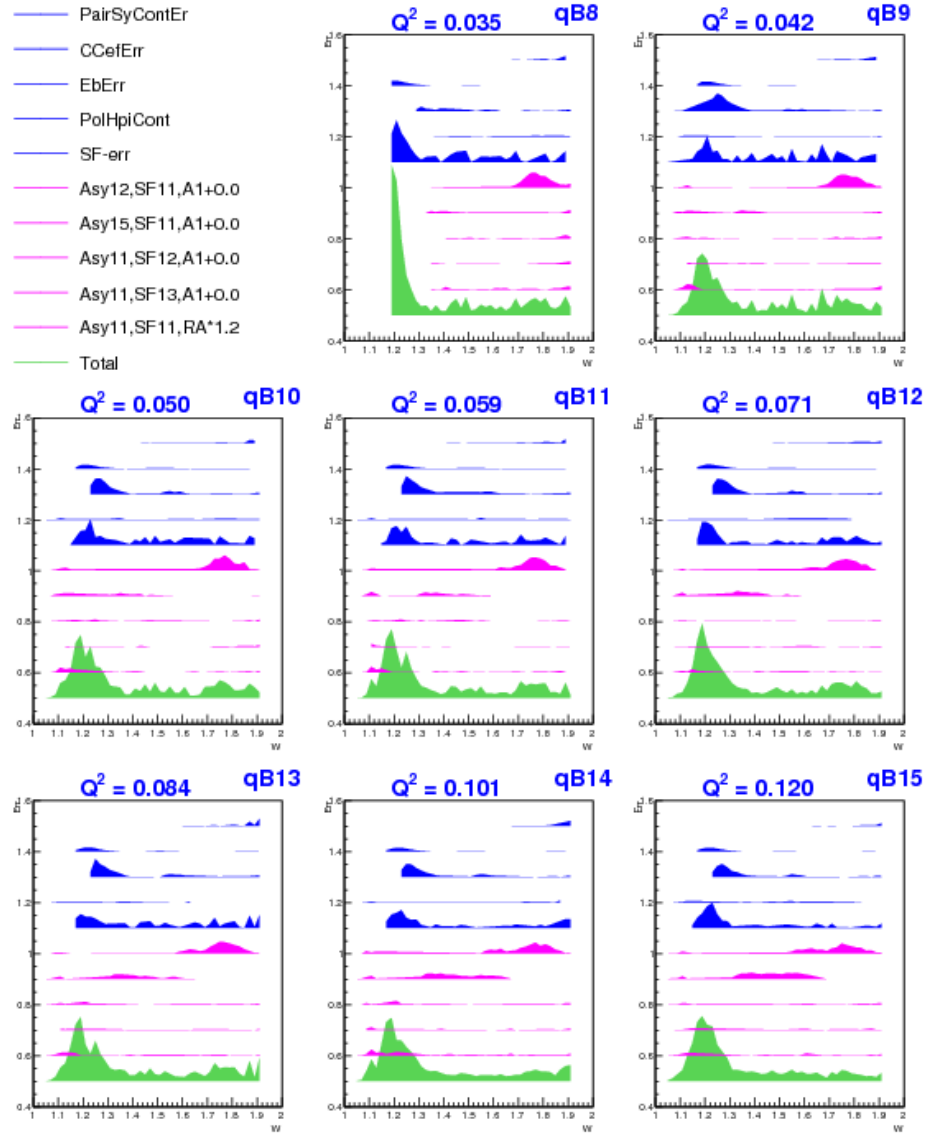


Figure 5.4: Plots similar to those shown in Fig. 5.2 but for 2.0 GeV, showing various components of systematic uncertainty on g_1 plotted against W in different Q^2 bins.

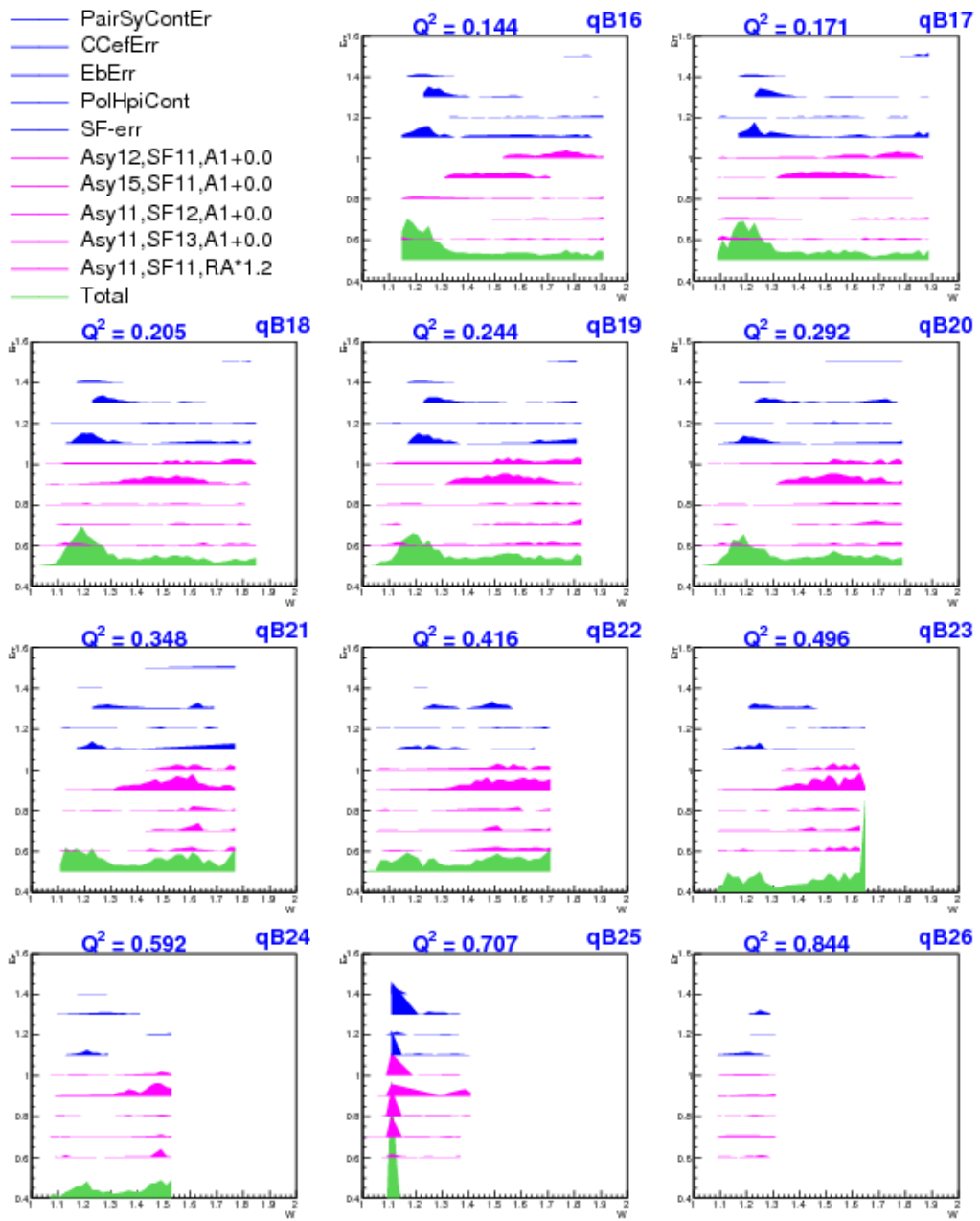


Figure 5.5: Systematic uncertainty components in remaining Q^2 bins (continuation of Fig. 5.4).

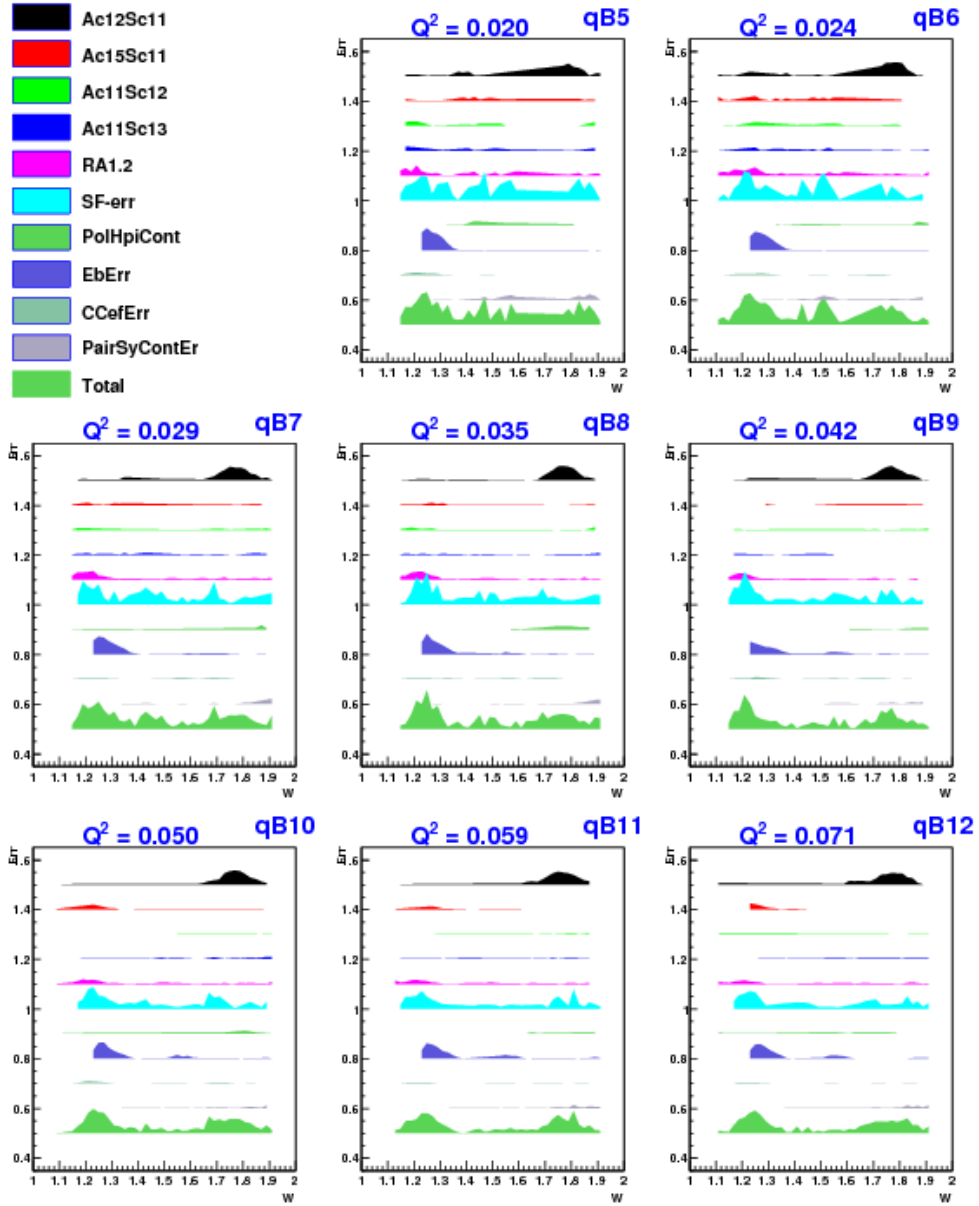


Figure 5.6: Breakdown of systematic uncertainties in g_1 (after combining data from the two energy data sets) in the first few Q^2 bins. See Fig. 5.1 for the description of the different systematic uncertainty components.

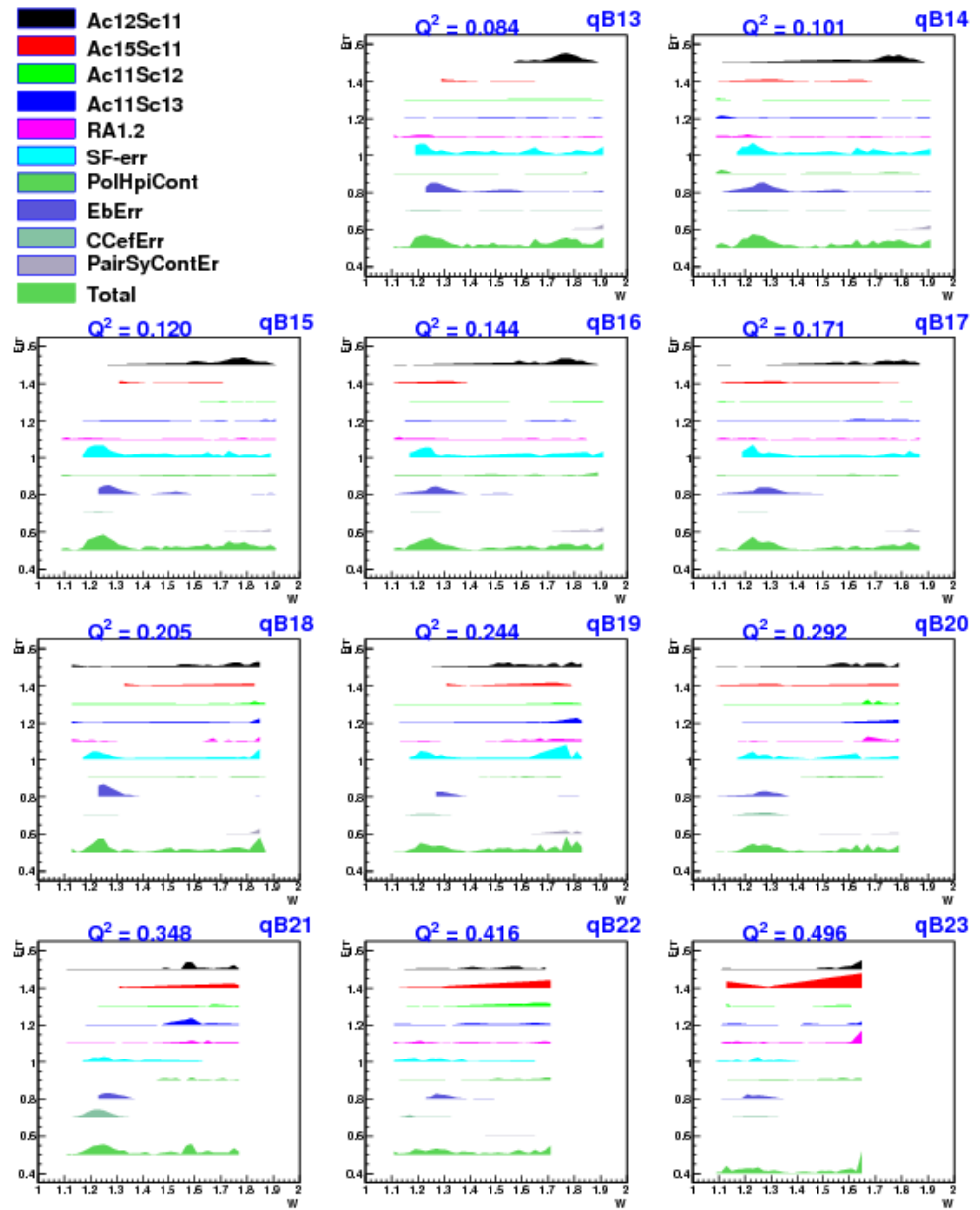


Figure 5.7: Plots as in Fig. 5.6 but in the remaining higher Q^2 bins.

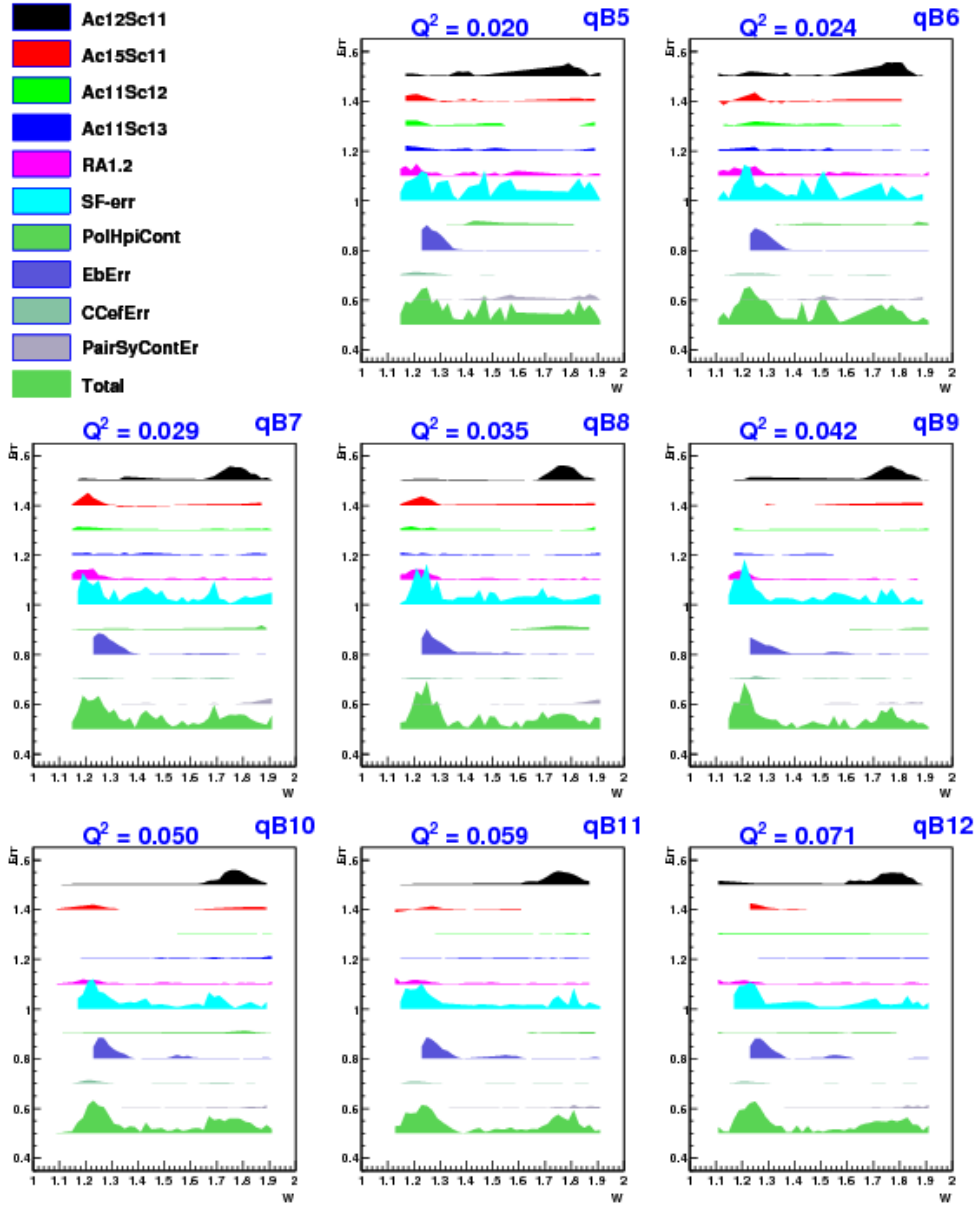


Figure 5.8: Breakdown of systematic uncertainties in $A_1 F_1$ (after combining data from the two energy data sets) in the first few Q^2 bins. See Fig. 5.1 for the description of the different systematic uncertainty components.

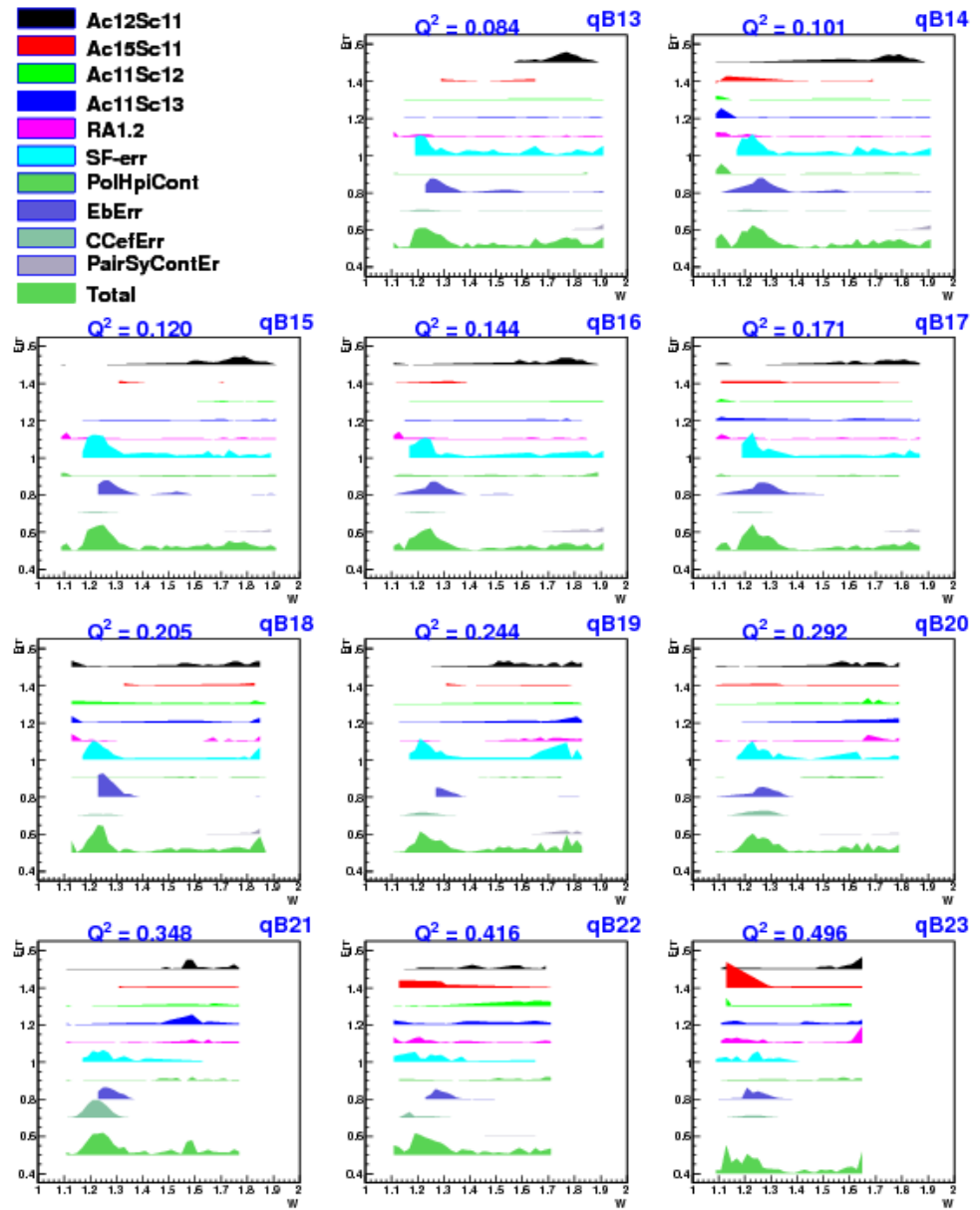


Figure 5.9: Plots as in Fig. 5.8 but in the remaining higher Q^2 bins.

1842 **Chapter 6**

1843 **Results**

1844 Two quantities - g_1 and $A_1 F_1$ and their uncertainties were extracted from the
1845 EG4 deuteron target data using the methods outlined in the previous chapter.
1846 This was done in each of 21 Q^2 bins (between about 0.02 and 0.7 GeV 2 in
1847 Q^2) and several W bins of size 20 MeV each. In the overlapping kinematic
1848 bins where both beam energy data sets contributed, the results were further
1849 combined individually to arrive at a single set of energy independent data
1850 points. Finally, within each Q^2 bin, the newly extracted g_1 and $A_1 F_1$ values
1851 were used to evaluate three different integrals - Γ_1^d , \bar{I}_{TT} , and γ_0^d . All of these
1852 results are presented in the sections below.

1853 **6.1 Extracted g_1 and $A_1 F_1$**

1854 Figures 6.1 and 6.2 show the extracted values of g_1 and their errors from
1855 two different beam energies (1.337 GeV and 1.989 GeV). It can be seen that
1856 the two energies give results that are in good agreement in the overlapping
1857 kinematic regions.

1858 These results from low Q^2 measurements clearly show the resonant struc-
1859 ture in the region $W \leq 2.0$. Especially, the Δ -resonance stands out through
1860 its strongly negative signal. In addition, in the second resonance region
1861 around $W=1.5$ GeV where $N^*(1520)$ and $N^*(1535)$ (also denoted by D_{11}
1862 and S_{13} respectively) overlap, we see a drastic transition of g_1 (or cross sec-
1863 tion) from strongly negative values (not well described by the model because
1864 it is unconstrained there due to the lack of experimental data) at low Q^2
1865 to clearly positive values at high Q^2 indicating that the dominance of the

1866 spin-flip helicity amplitude $A_{\frac{3}{2}}^T$ on cross section drastically diminishes with
1867 Q^2 and the non-flip amplitude $A_{\frac{1}{2}}^T$ becomes stronger¹. We have pushed the
1868 lower limit on Q^2 in the resonance region with reduced systematic and sta-
1869 tistical errors that will contribute greatly to the world data set. Our data
1870 will help MAID and other phenomenological models to better constrain their
1871 parameters enabling them to make better predictions in the future.

¹The four virtual photoabsorption cross sections σ_T , σ_L , σ_{LT} , and σ_{TT} , are related to the four structure functions F_1 , F_2 , g_1 and g_2 of the target and as a result, g_1 can be expressed as $g_1 = \frac{MK}{8\pi^2\alpha(1+\gamma^2)}(\sigma_{\frac{1}{2}}^T - \sigma_{\frac{3}{2}}^T + 2\gamma\sigma_{LT})$

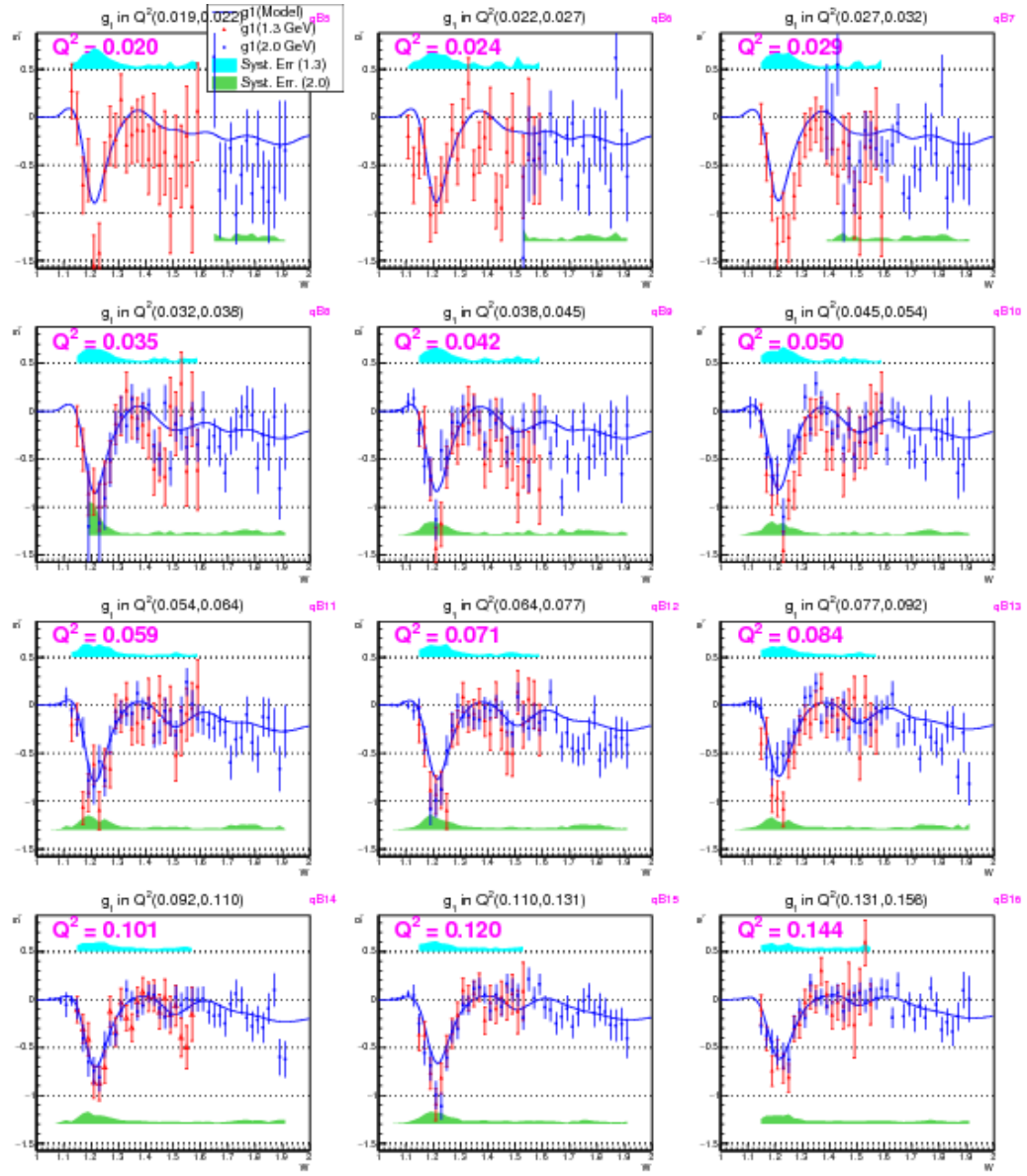


Figure 6.1: Extracted g_1 for deuteron (in the first 12 Q^2 bins) from the two different beam energy data sets. The statistical errors are indicated by error bars, while the systematic uncertainties are given by the bands (cyan, top: 1.3 GeV and green, bottom: 2 GeV).

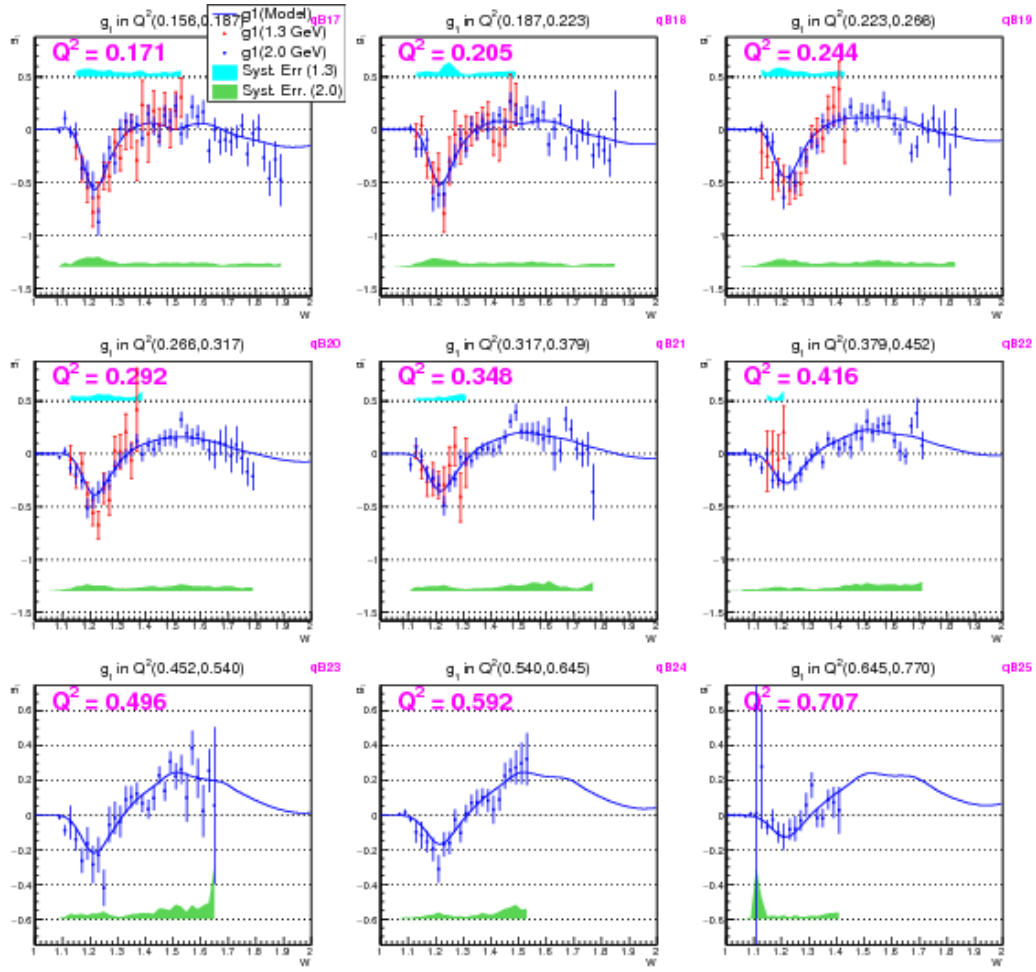


Figure 6.2: Extracted g_1 for deuteron (in the last 9 Q^2 bins (see Fig. 6.1 for the first 12 bins)) from the two different beam energy data sets.

Likewise, Figs. 6.3 and 6.4 shows the extracted values of $A_1 F_1$ and their errors from two different beam energies (1.3 GeV and 2.0 GeV). These values also show similar behavior as g_1 .

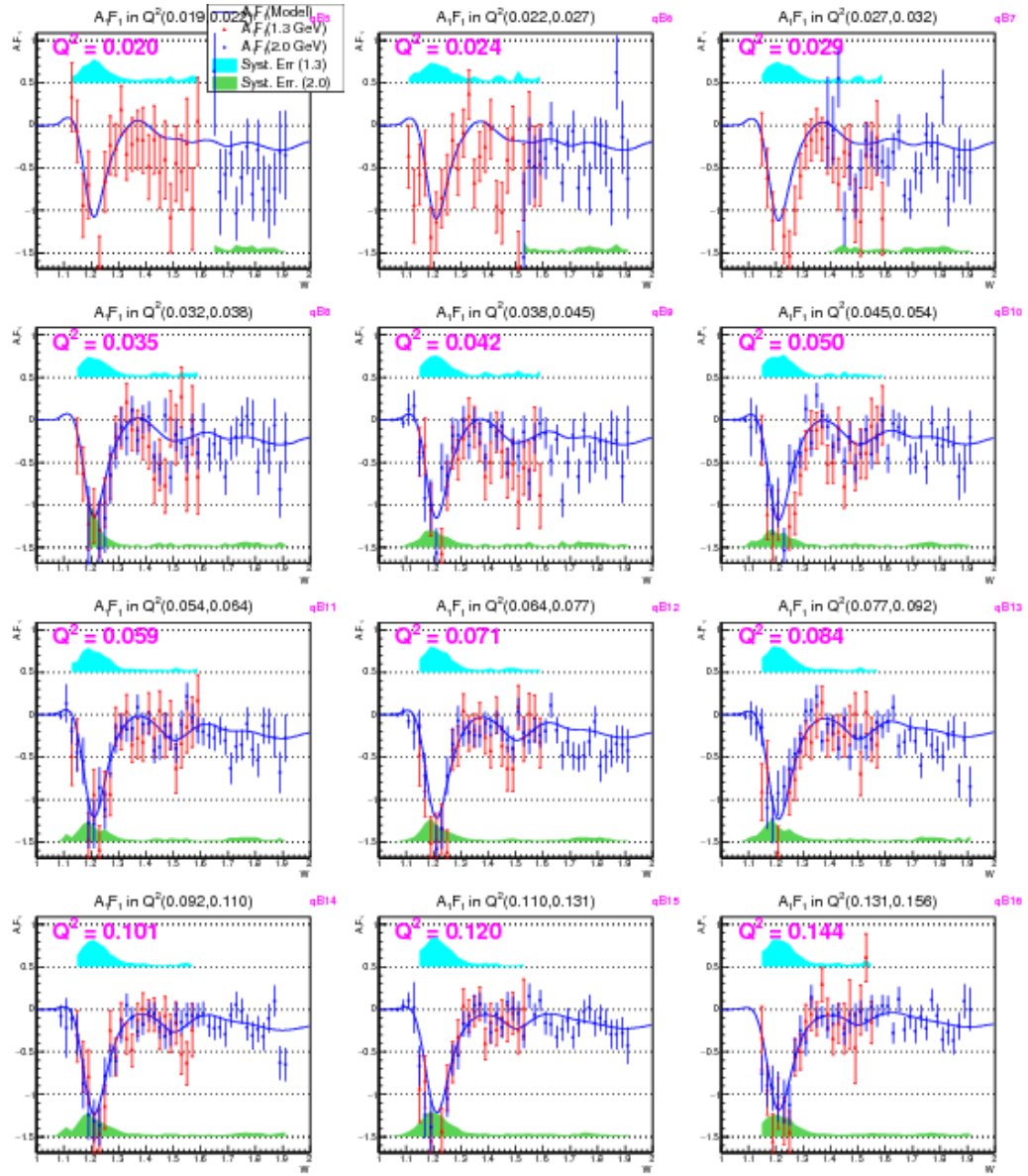


Figure 6.3: Extracted $A_1 F_1$ for deuteron (in the first 12 Q^2 bins) from the two different beam energy data sets. The statistical errors are indicated by error bars, while the systematic uncertainties are given by the bands (cyan, top: 1.3 GeV and green, bottom: 2 GeV).

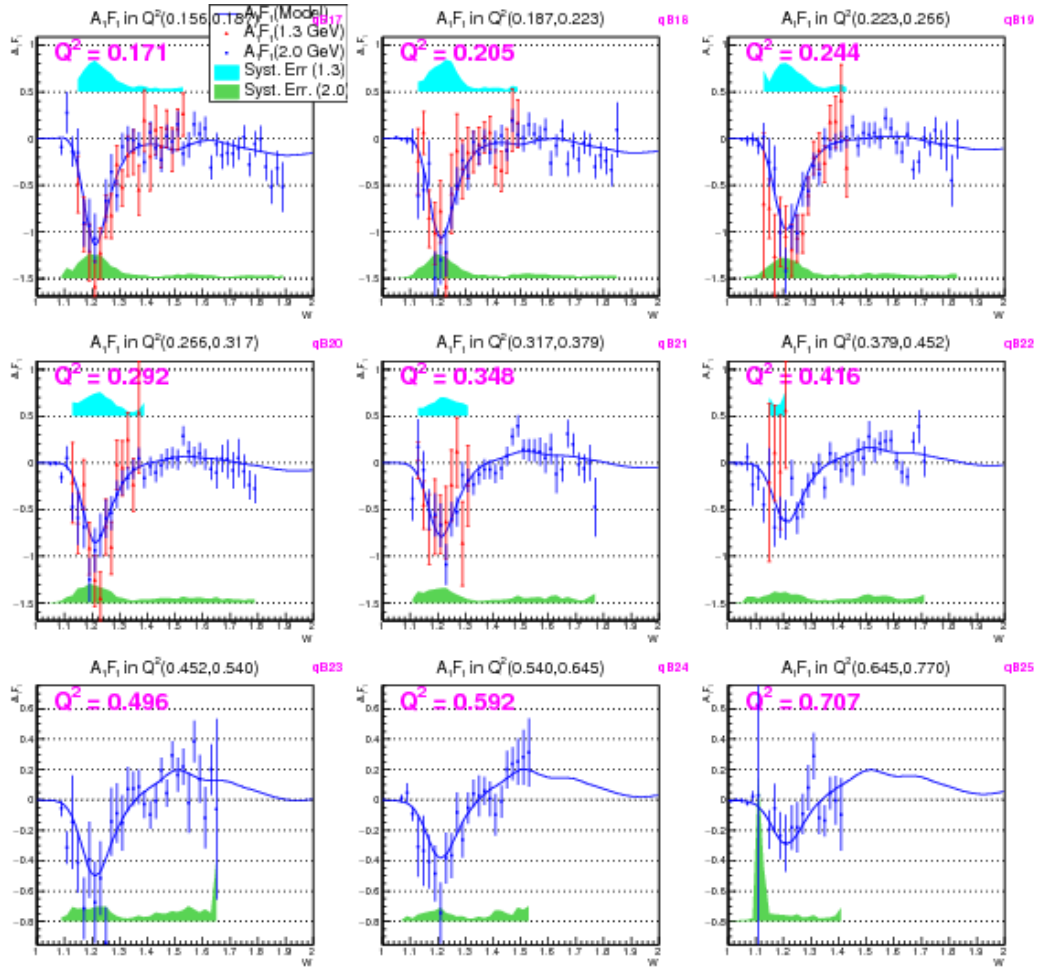


Figure 6.4: Extracted $A_1 F_1$ for deuteron (in the last 9 Q^2 bins (see Fig. 6.3 for the first 12 bins)) from the two different beam energy data sets..

1875 Figs. 6.5, 6.6, 6.7 and 6.8 show the values of g_1 and $A_1 F_1$ and their
 1876 errors after combining the corresponding results from the two different beam
 1877 energies as described in the previous chapter.

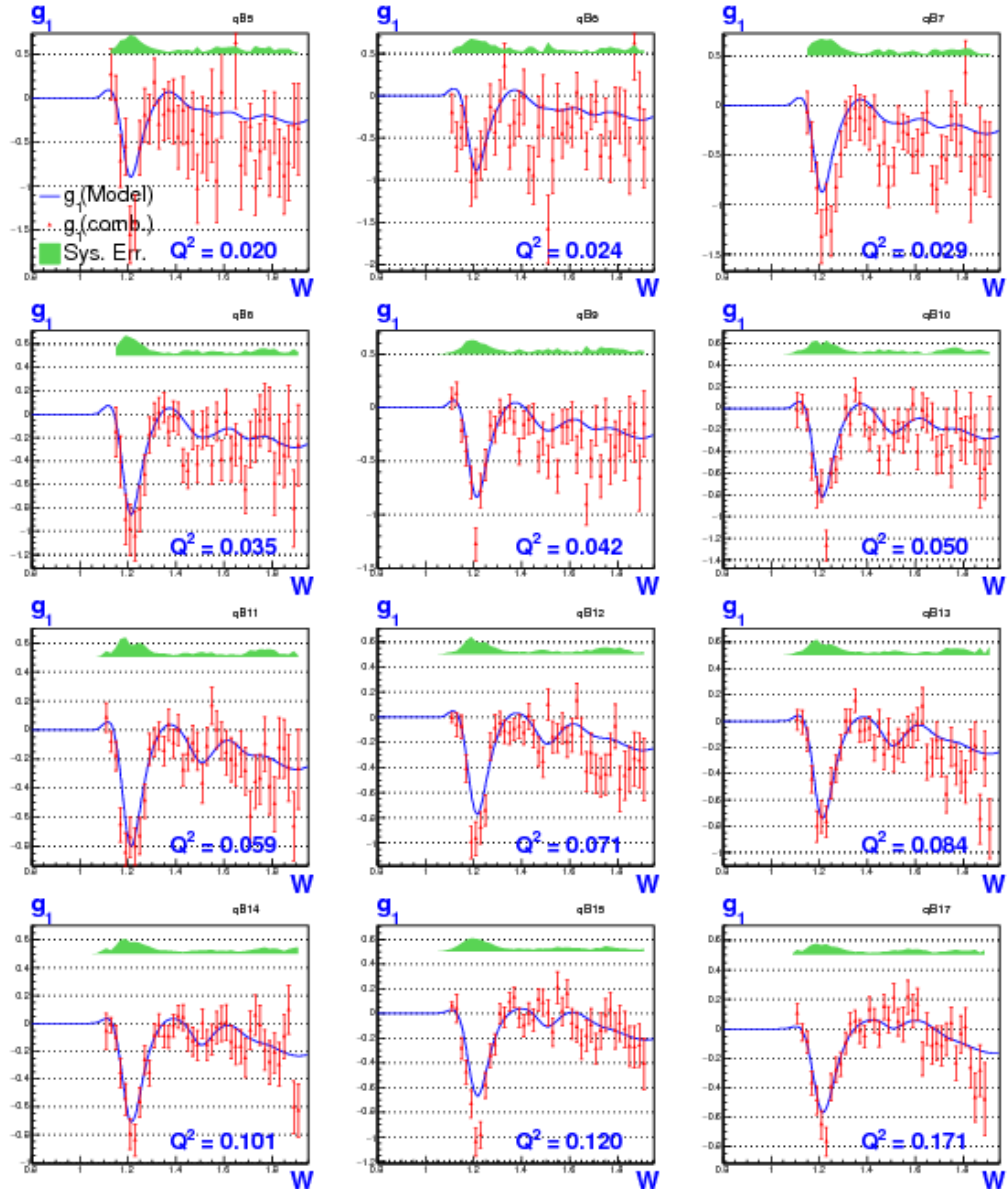


Figure 6.5: Extracted g_1 for deuteron after combining the results from the two beam energies (in the first 12 Q^2 bins). The red data points with error bars in each of the panels are the combined extracted results, the blue continuous line is the used model of g_1 and the green band represents the corresponding total systematic errors.

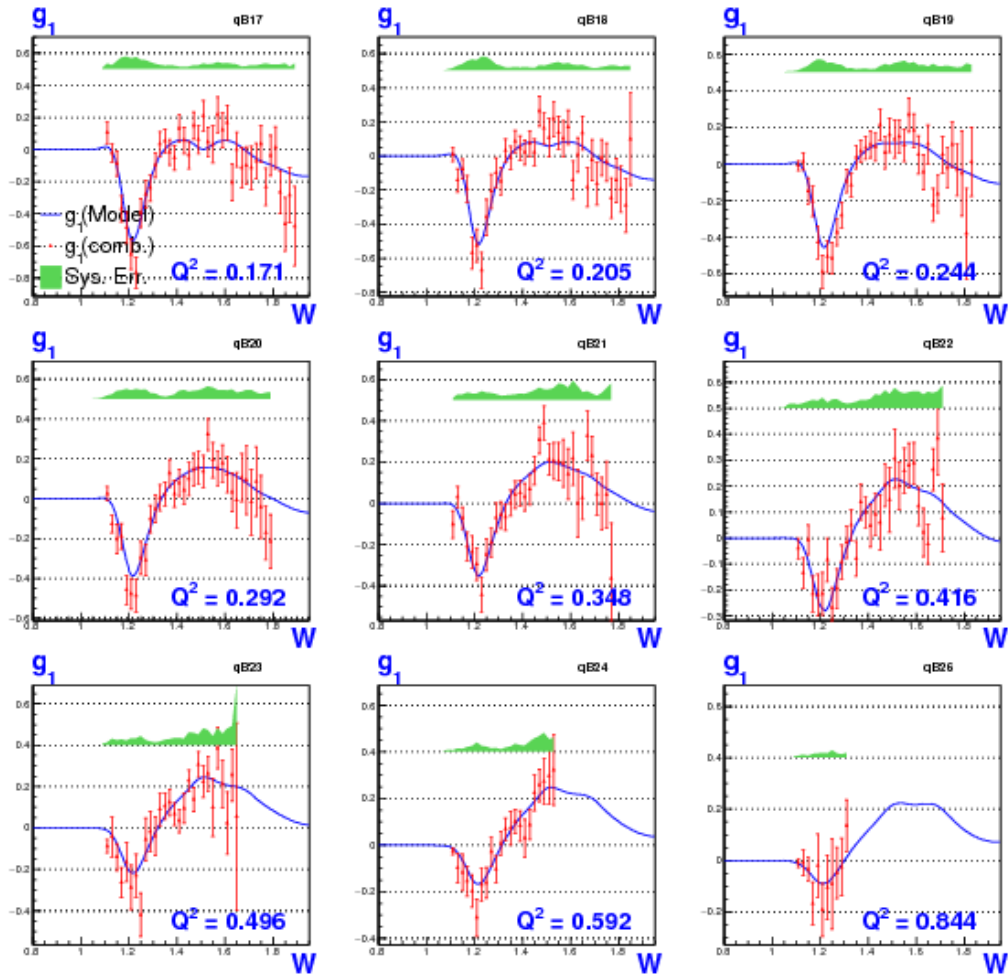


Figure 6.6: Similar plots as in Fig. 6.5 showing the combined results on g_1 in the next 9 Q^2 bins.

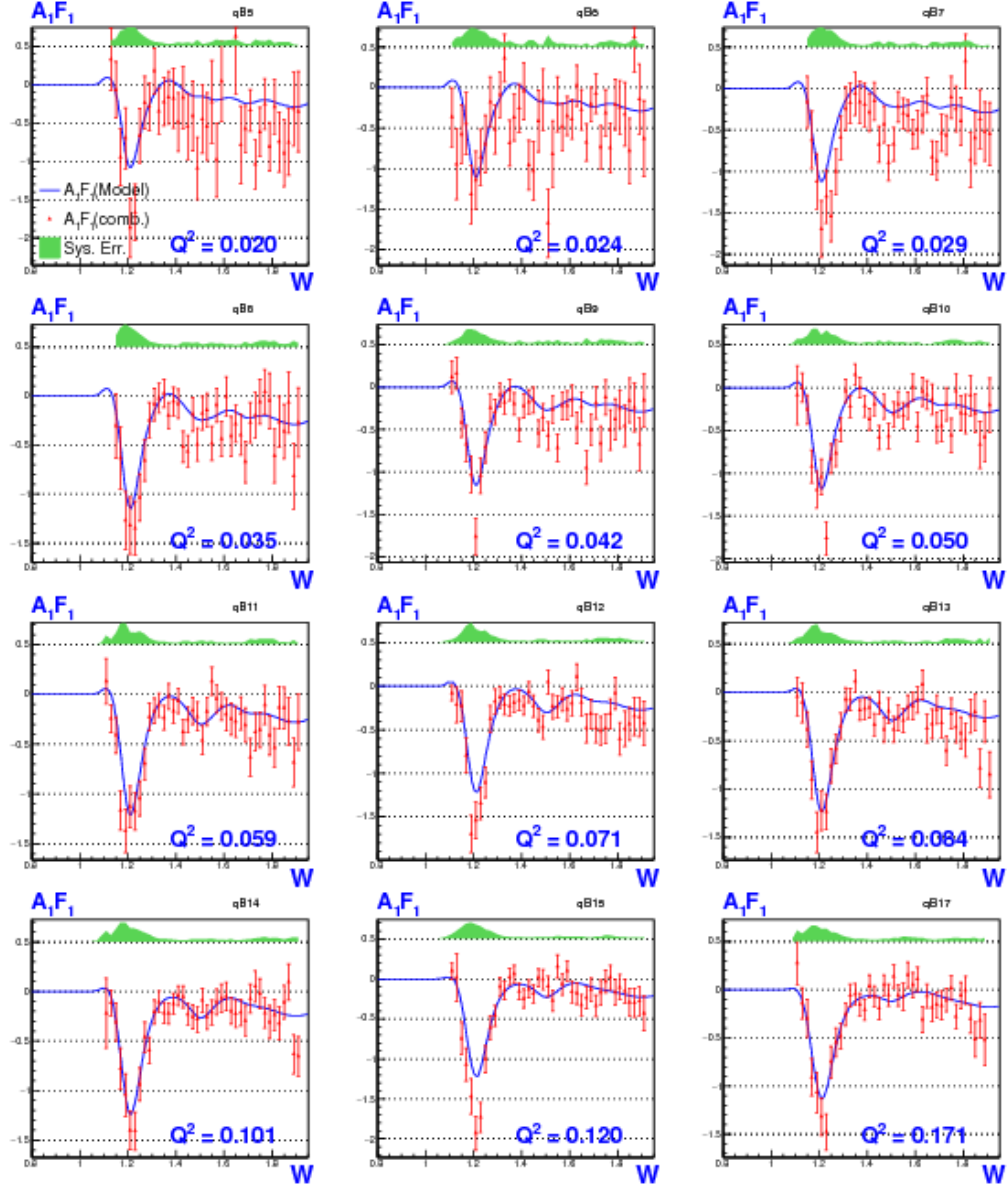


Figure 6.7: $A_1 F_1$ after combining the results from the two beam energies (in the first 12 Q^2 bins). The red data points with error bars in each of the panels are the combined extracted results, the blue continuous line is the used model of g_1 and the green band represents the corresponding total systematic errors.

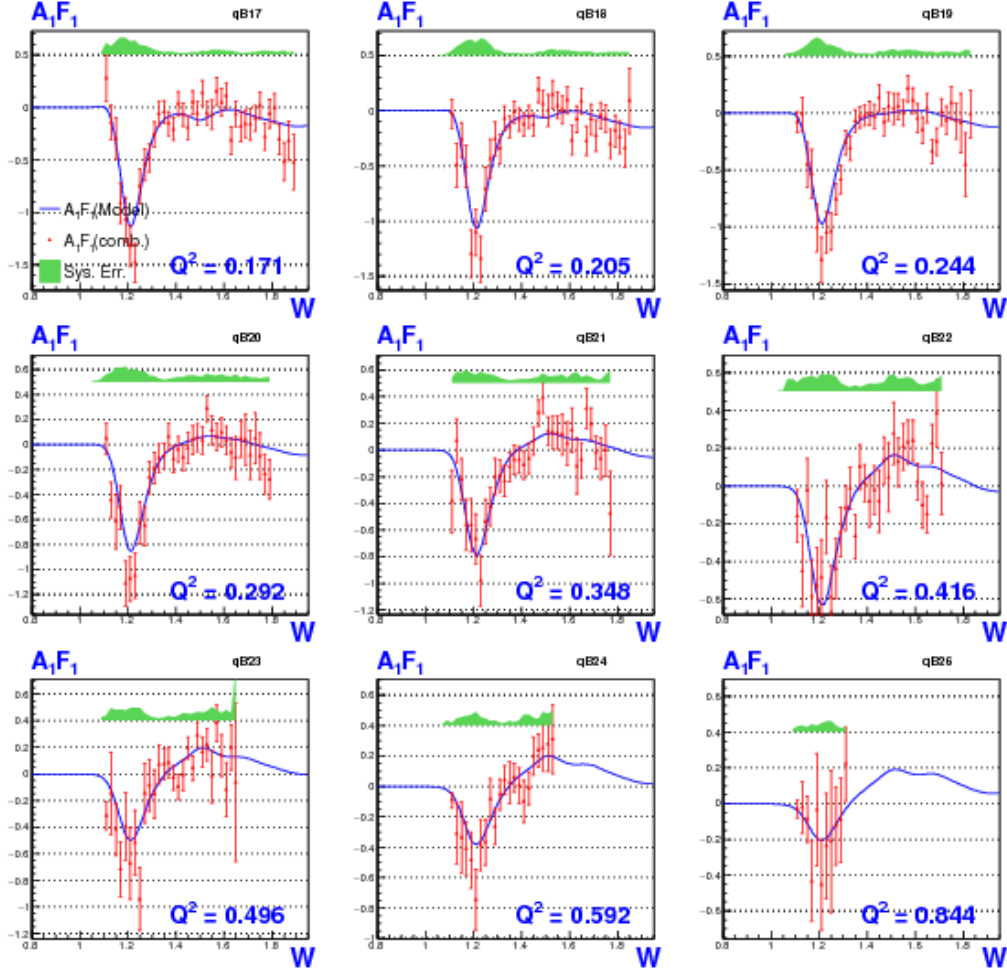


Figure 6.8: Similar plots as in Fig. 6.7 showing the combined results on g_1 in the next 9 Q^2 bins.

1878 **6.2 Moments of Deuteron Spin Structure func-**
 1879 **tions**

1880 Using the measured values of g_1 and A_1F_1 , three integrals were evaluated for
 1881 each of the Q^2 bins in which these data were measured. These integrals have
 1882 been calculated in two ways - using only the new EG4 measurements, and
 1883 adding model contributions to the data for regions not covered by our mea-

1884 surements. The integrals with the model contributions were calculated from
 1885 $x = 0.001$ to the onset of the resonance region (i.e. to the pion production
 1886 threshold of $W \approx 1.08$ GeV), dividing the sum into three parts for each Q^2
 1887 bin. For example, Γ_1 was evaluated by adding up the product $g_1 \Delta x$ over the
 1888 following three kinematic regions:

$$\Gamma_1(Q^2) = \int_{x=0.001}^{x(W_{data})} g_1(x, Q^2) dx \quad \text{model} \quad (6.1)$$

$$+ \int_{x(W_{data})}^{W=1.15} g_1(x, Q^2) dx \quad \text{data (or model for gaps)} \quad (6.2)$$

$$+ \int_{W=1.15}^{W=1.08} g_1(x, Q^2) dx \quad \text{model} \quad (6.3)$$

1889 where W_{data} indicates the upper edge of the last W bin in which the EG4
 1890 data is available in a given Q^2 bin (the W variable was divided into 70 bins
 1891 of size 20 MeV in the range $W=(0.7,2.1)$ GeV). The first part of the integral
 1892 as given by Eq. 6.1 is evaluated by using the model values of g_1 and using
 1893 Δx corresponding to a W bin of size 10.0 MeV. The ΔW is converted to Δx
 1894 by using $x = Q^2/(Q^2 + W^2 - M^2)$ to evaluate x at the two edges of each W
 1895 bin and taking the difference as follows:

$$\Delta x = x_{High} - x_{Low} = \frac{Q^2}{Q^2 + W_{High}^2 - M^2} - \frac{Q^2}{Q^2 + W_{Low}^2 - M^2} \quad (6.4)$$

1896 The second part given by Eq. 6.2 is evaluated similarly but using the EG4
 1897 results for g_1 if there is no measurement gap in between. If there is any gap,
 1898 the same method as in the first part is used to get a model contribution for the
 1899 gap and added to the data contribution. Lastly, the the third contribution
 1900 given by Eq. 6.2 again were evaluated from from model values (quasi-elastic
 1901 part turned off from the model in all of these cases) but with finer W bins
 1902 (1 MeV) because the integrals are very sensitive to the region near the Δ
 1903 resonance due to the fact that the structure functions show rapid changes
 1904 in this region. The reason to calculate the third integral using model values
 1905 rather than data values is to avoid having contributions in the integrals from
 1906 the quasi-elastic contamination.

1907 The statistical errors are evaluated by adding the statistical error con-
 1908 tribution in each W or x bin in quadrature. For example, if the integral is
 1909 evaluated in a Q^2 bin by calculating the sum $\left(\sum_{W \text{ bins}} g_1 \cdot \Delta x \right)$, then the cor-

1910 responding statistical error is evaluated by calculating $\sqrt{\sum_{W \text{ bins}} (\sigma g_1)^2 \cdot \Delta x}$.

1911 Because the model contribution is assumed to have no statistical uncertainties,
1912 the statistical errors in the integrals come solely from the propagation
1913 of the statistical error of the measured g_1 or $A_1 F_1$.

1914 The other two integrals and their errors are evaluated in the same manner,
1915 with g_1 replaced by their corresponding integrands and again calculating the
1916 three parts of the integrals separately.

1917 These integrals are then compared with the latest available predictions
1918 from different theories (mainly χ PT) and phenomenological calculations along
1919 with EG1b or DIS data whenever applicable.

1920 6.2.1 First moment of g_1 (Γ_1)

1921 The first integral of interest is the first moment of g_1 i.e., Γ_1 (see Eq. 1.10)
1922 , which was calculated for all Q^2 bins for which the new data are available.
1923 Figs. 6.9 and 6.10 show the two calculations (with and without model in-
1924 put) along with EG1b data and several χ PT and model predictions. One
1925 important observation here is that our measurements provide the only data
1926 points in the very low Q^2 region (i.e for $Q^2 < 0.05$ GeV 2) where χ PT is
1927 thought to be able to make rigorous calculations. Therefore, our data will
1928 provide important benchmarks for the future calculations in this kinematics.
1929 Particularly, the latest χ PT prediction by Bernard *et al.* [49] seems to agree
1930 remarkably well with data in the very low Q^2 region.

1931 While all other higher Q^2 predictions, except that of Ji *et al.*, seem to
1932 be within the uncertainties of our measurements, it can be seen that the
1933 phenomenological predictions of Soffer *et al.* compare slightly better with
1934 data than others (excluding, of course, the Bernard *et al.* prediction).

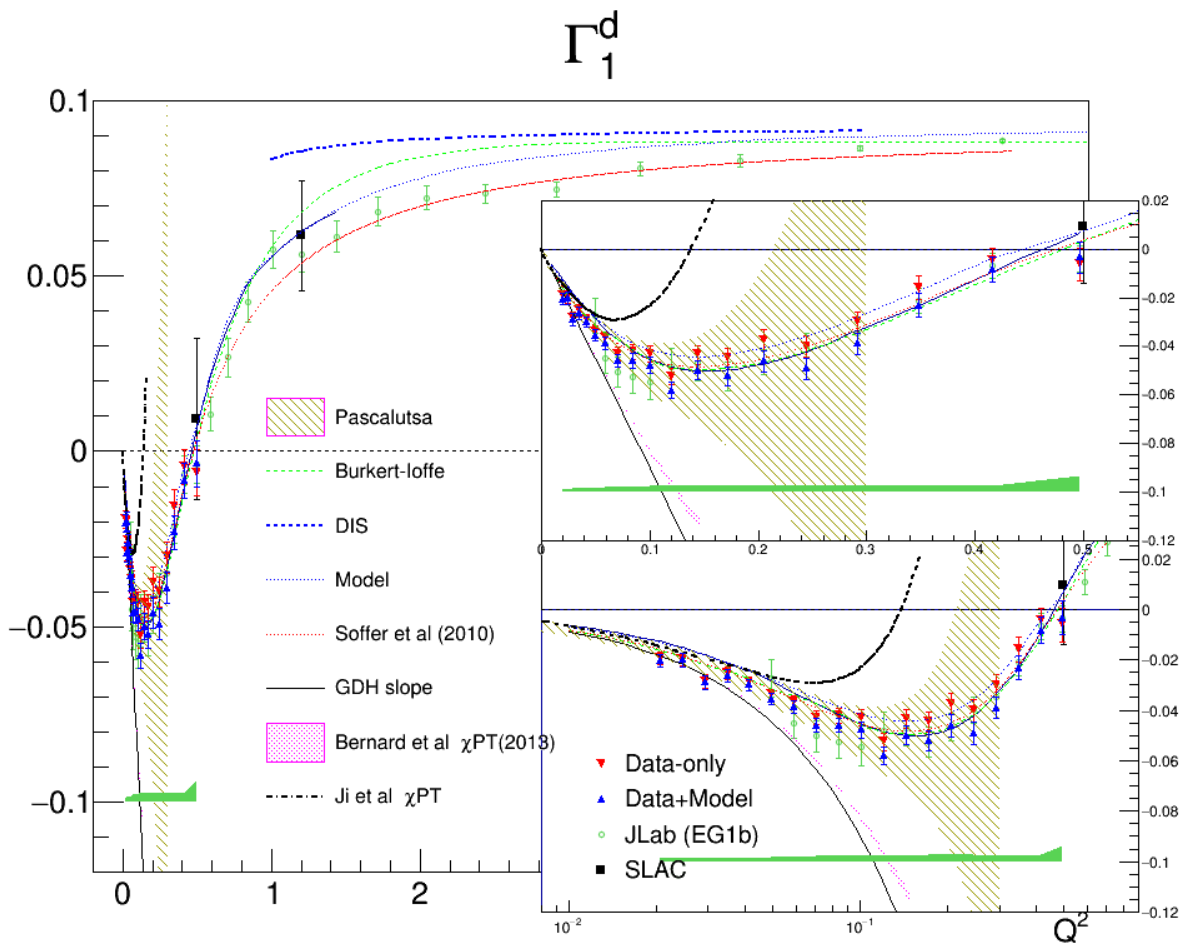


Figure 6.9: Extracted Γ_1 for deuteron compared with some of the past measurements and various theoretical predictions with a linear scale used for Q^2 .

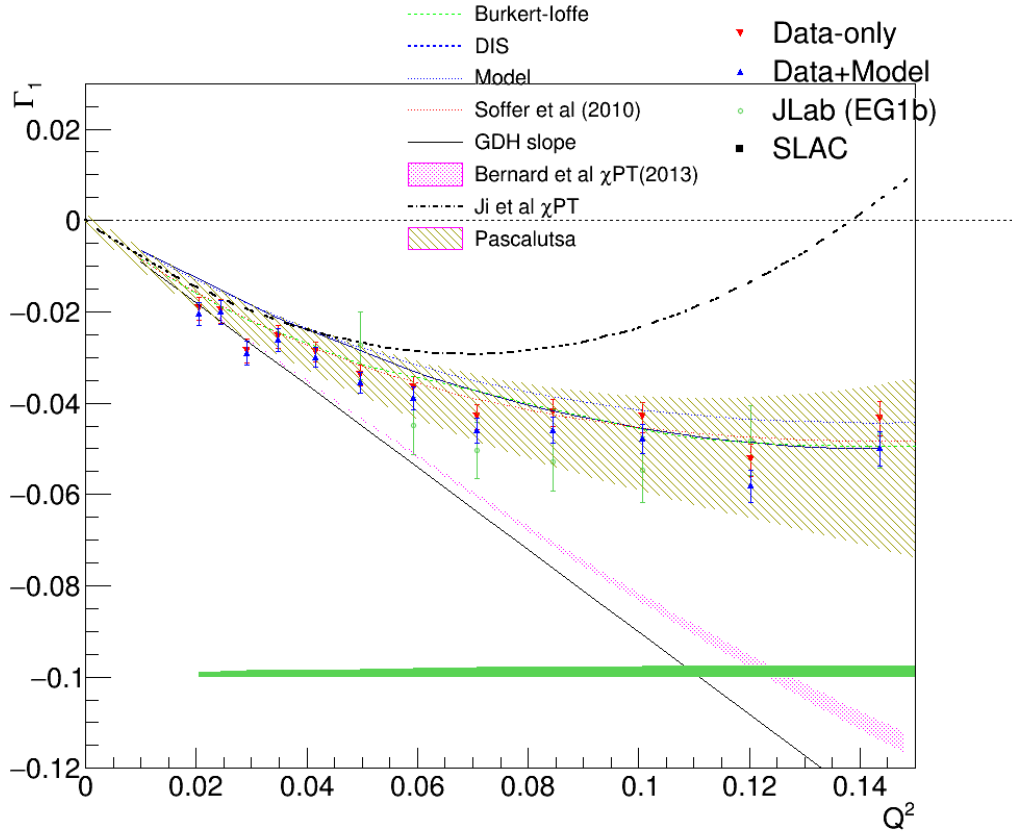


Figure 6.10: Extracted Γ_1 for deuteron compared with some of the past measurements and various theoretical predictions zooming in on the very low Q^2 region.

1935 6.2.2 The extended GDH integral \bar{I}_{TT}

1936 Using the measured values of $A_1 F_1$, the generalized GDH integral $\bar{I}_{TT} =$
 1937 $2M^2/Q^2 \int A_1 F_1(x, Q^2) dx$ was also calculated and compared (see Figs. 6.11
 1938 and 6.12) with the latest χ PT calculation from Bernard *et al.* [49]. We
 1939 can see that at the very low Q^2 , the χ PT prediction and the measurement
 1940 get very close. The χ PT methods determine the higher powers of Q^2 in the
 1941 Taylor expansion of the integral around the photon point $Q^2 = 0$, beyond the
 1942 prediction of the GDH sum rule which determines the lowest order term. Our
 1943 data seem indeed to converge towards the GDH sum rule at our lowest Q^2 .
 1944 However, only one or two higher order terms can be calculated confidently,
 1945 since higher orders require additional (unknown) constants. Therefore, χ PT

¹⁹⁴⁶ predictions do reasonably well at ultra-low Q^2 but cannot be expected to
¹⁹⁴⁷ work at the higher Q^2 , where the data show a turn-around and a transition
¹⁹⁴⁸ towards positive values.

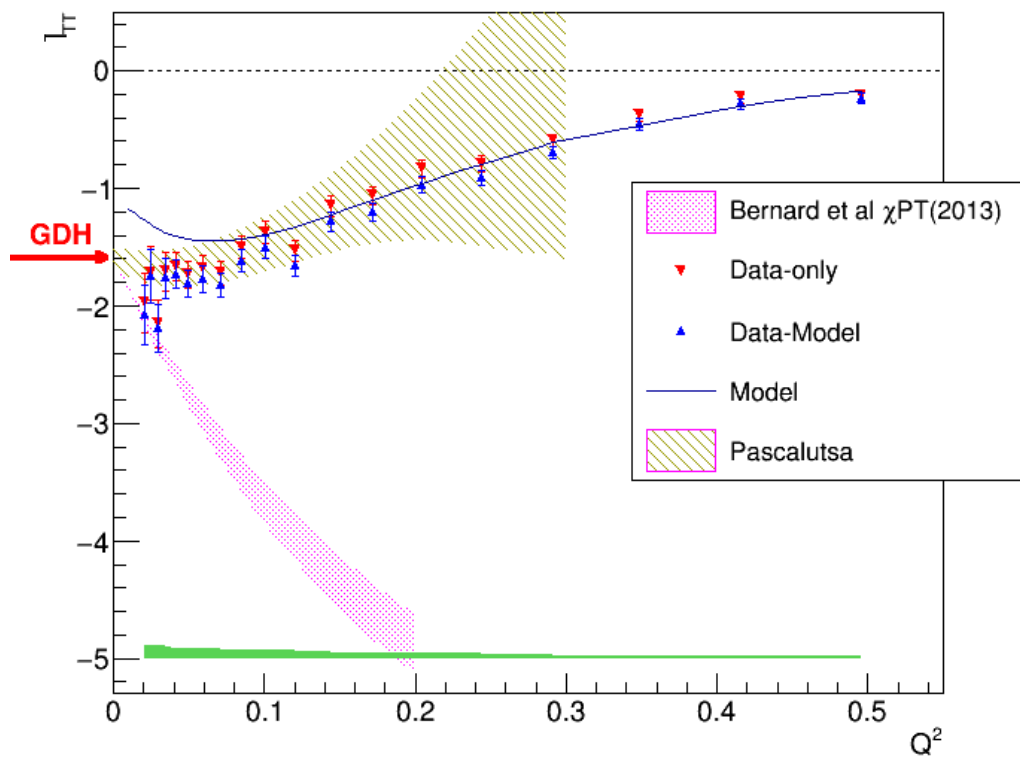


Figure 6.11: Extracted \bar{I}_{tt} for deuteron compared with the used model and a χ PT prediction with a linear scale used for Q^2 .

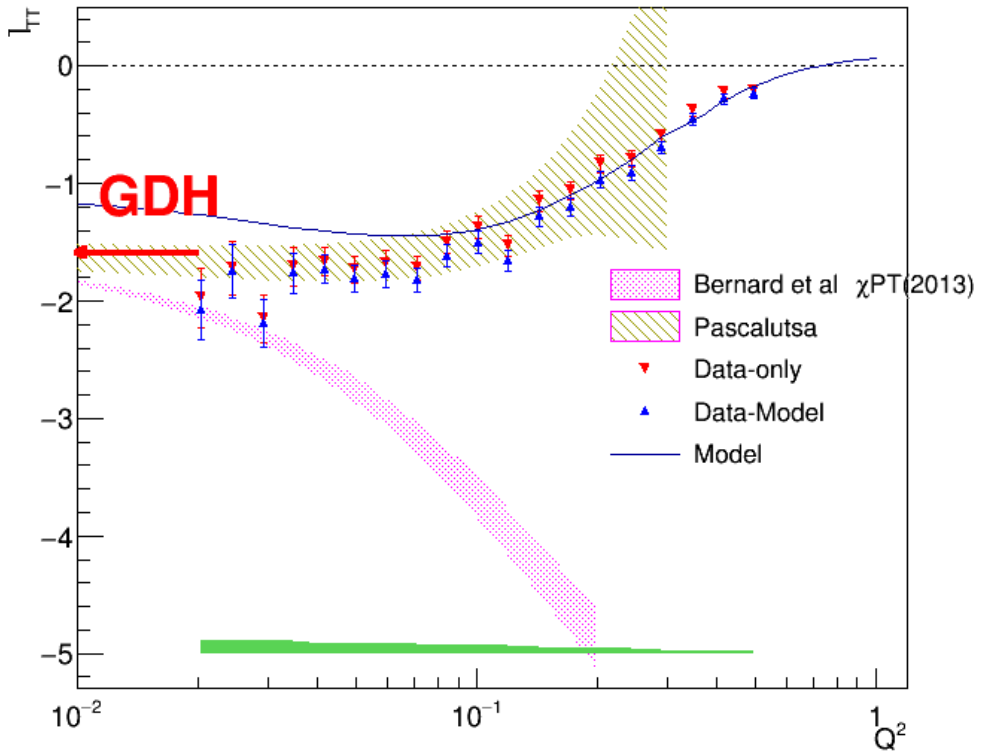


Figure 6.12: Extracted I_{tt} for deuteron compared with the model used in the simulation and two χ PT predictions with a logarithmic scale used for Q^2 .

1949 6.2.3 The Generalized Forward Spin Polarizability γ_0

1950 Finally, the generalized forward polarizability (as given by Eq. 1.16) for
 1951 the deuteron was also calculated using the measured values of $A_1 F_1$ and
 1952 then compared with various predictions as shown in Figs. 6.13 and 6.14.
 1953 The comparison shows that both χ PT calculations by Bernard *et al.* and
 1954 Kao *et al.* converge with data at the lowest Q^2 bins. However, the χ PT
 1955 calculations by Pascalutsa *et al.* seem to deviate greatly from both the
 1956 current measurement as well as the other χ PT calculations (particularly at
 1957 the very low Q^2 region, indicating that some ingredients might be missing
 1958 from the calculation model). Likewise, the MAID prediction also seems to be
 1959 somewhat off the current results.

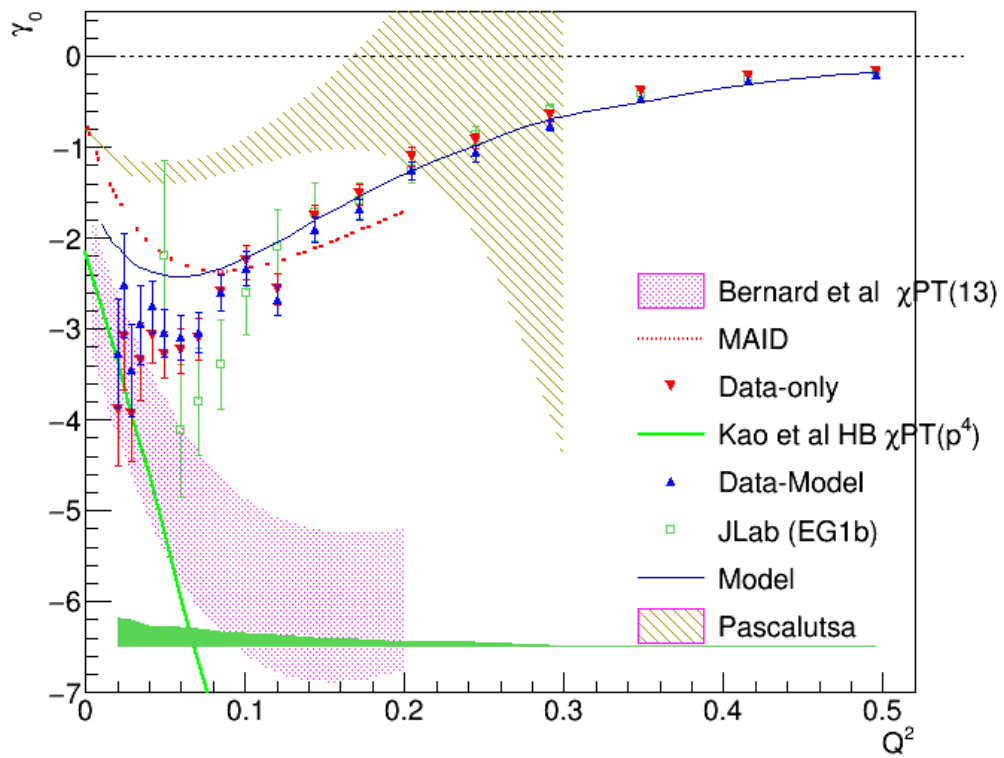


Figure 6.13: Extracted γ_0 for deuteron compared with some of the past measurements and various theoretical predictions with a linear scale used for Q^2 .

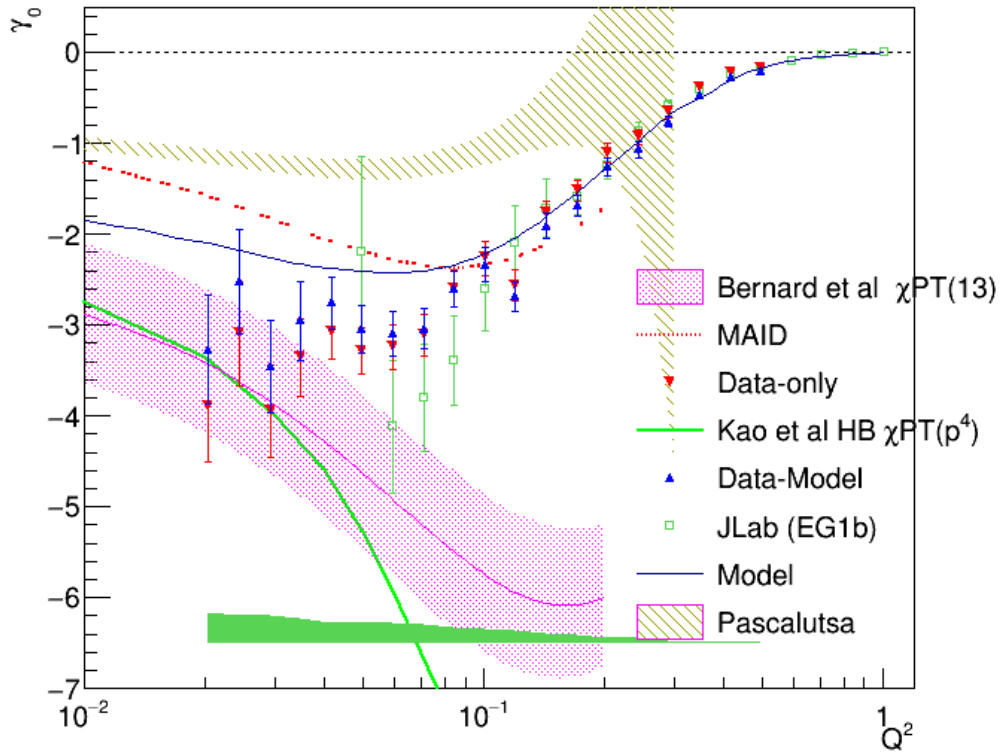


Figure 6.14: Extracted γ_0 for deuteron compared with some of the past measurements and various theoretical predictions with a logarithmic scale used for Q^2 .

¹⁹⁶⁰ **Chapter 7**

¹⁹⁶¹ **Conclusions**

¹⁹⁶²

¹⁹⁶³ The very low momentum transfer (Q^2) data from the EG4 experiment
¹⁹⁶⁴ have been analyzed for the helicity dependent inclusive cross section (difference)
¹⁹⁶⁵ for the scattering of longitudinally polarized electrons off longitudinally
¹⁹⁶⁶ polarized deuterons (from DNP polarized ND₃ target, using two beam en-
¹⁹⁶⁷ ergies 1.3 and 2.0 GeV). The analyzed data has the kinematic coverage of
¹⁹⁶⁸ ($0.02 \text{ GeV}^2 < Q^2 < 0.7 \text{ GeV}^2$) and ($1.08 \text{ GeV} < W < 2.0 \text{ GeV}$). Al-
¹⁹⁶⁹ though past measurements from EG1b go as low as 0.05 GeV^2 in Q^2 , the
¹⁹⁷⁰ new measurements have higher precision (due to higher statistics and bet-
¹⁹⁷¹ ter detection efficiency) in the overlapping region (particularly evident below
¹⁹⁷² $Q^2 = 0.2 \text{ GeV}^2$) in addition to new high precision data in the previously
¹⁹⁷³ unmeasured region below $Q^2 = 0.5 \text{ GeV}^2$.

¹⁹⁷⁴ The new deuteron data were used to extract the deuteron's spin struc-
¹⁹⁷⁵ ture function g_1 by comparing the experimental data with simulated data
¹⁹⁷⁶ produced by using a realistic cross section model for the deuteron under sim-
¹⁹⁷⁷ ilar kinematic conditions. The newly extracted data pushes the lower limit
¹⁹⁷⁸ on Q^2 in the resonance region with reduced systematic and statistical un-
¹⁹⁷⁹ certainties that will contribute greatly to the world data set. It is observed
¹⁹⁸⁰ that the data from two beam energies give results that are in good agreement
¹⁹⁸¹ wherever they overlap. The low Q^2 results clearly show resonance structure
¹⁹⁸² in the region $W \leq 2.0$ which smooths out as Q^2 becomes larger. In particular,
¹⁹⁸³ the Δ -resonance shows a strongly and consistently negative signal at all Q^2 ,
¹⁹⁸⁴ but the second resonance region (around $W=1.5 \text{ GeV}$) shows a rather rapid
¹⁹⁸⁵ transition of g_1 (or polarized cross section) from strongly negative values at
¹⁹⁸⁶ low Q^2 to clearly positive values at high Q^2 . This observation in the second

1987 resonance region is not well described by the model because the model is not
1988 constrained in the region due to the lack of experimental data up to now and
1989 indicates that the spin-flip helicity amplitude $A_{\frac{3}{2}}^T$ dominates the cross section
1990 at low Q^2 while the non-flip amplitude $A_{\frac{1}{2}}^T$ becomes stronger at higher Q^2 .

1991 The product $A_1 F_1$ of the virtual photon asymmetry A_1 and the unpo-
1992 larized structure function F_1 was also extracted from the same data and
1993 method. The extracted results on g_1 and $A_1 F_1$ were then used to evaluate
1994 three important moments - the first moment Γ_1^d of g_1 , the generalized GDH
1995 integral \bar{I}_{TT}^d and the generalized forward spin polarizability γ_0^d - in each of
1996 the Q^2 bins in which the new g_1 and $A_1 F_1$ have been extracted. The new low
1997 Q^2 measurements of the moments evaluated both with and without model
1998 inputs for the unmeasured kinematic regions were then compared with vari-
1999 ous χ PT calculations, phenomenological predictions and past measurements,
2000 particularly the EG1b or DIS data whenever applicable.

2001 The EG4 results provide the only data points in the very low Q^2 region
2002 ($Q^2 < 0.05 \text{ GeV}^2$) where χ PT is thought to be able to make rigorous calcu-
2003 lations. The high precision data will provide important benchmarks for the
2004 future calculations in this kinematics. In the case of the first moment Γ_1^d ,
2005 the EG4 results show remarkable agreement with the latest χ PT prediction
2006 by Bernard *et al.* [49] in the very low Q^2 region. The phenomenological
2007 predictions which have much larger Q^2 coverage also seem to agree within
2008 the uncertainties of our measurements, with the predictions of Soffer *et al.*
2009 showing slightly better comparison than others. Likewise, the very low Q^2
2010 results of the generalized GDH integral \bar{I}_{TT} are indeed observed to converge
2011 towards the GDH sum rule and thus getting very close to the χ PT predic-
2012 tions by Bernard *et al.* [49]. Finally, the generalized forward polarizability
2013 (γ_0^d) for the deuteron calculated from the EG4 data and the χ PT calculations
2014 by Bernard *et al.* and Kao *et al.* seem to converge at the lowest Q^2 bins.
2015 However, the χ PT based predictions from Pascalutsa *et al.* and the MAID
2016 prediction seems to be well off the current results for all three moments.

2017 The deuteron data in combination with the EG4 proton data taken under
2018 similar conditions (currently being analyzed by another collaborator) will be
2019 useful in extracting neutron quantities in the near future, which is valuable
2020 because of the unavailability of free neutron targets. Moreover, due to the
2021 complexities of the nuclear medium effects, neutron data from deuteron will
2022 be very important to enhance confidence in similar neutron results extracted
2023 from other nuclear targets - particularly ${}^3\text{He}$.

2024 The work presented in this analysis has improved our understanding of the
2025 field of the nucleon spin structure and contributed to more solid foundation
2026 for future advancements. The new data on spin structure functions and their
2027 moments will help various χ PT calculations and phenomenological models
2028 such as MAID to better constrain their parameters enabling them to make
2029 better predictions in the future. With the availability of the high precision
2030 data in the previously (largely) unmeasured region that has the potential to
2031 help constrain the theories and models, it is hoped that a unified description
2032 of spin structure functions over all kinematic regions will be possible in the
2033 future.

²⁰³⁴ **Bibliography**

- [1] K.V. Dharmawardane, S.E. Kuhn, P. Bosted, Y. Prok, G. Adams, P. Ambrozewicz, M. Anghinolfi, G. Asryan, H. Avakian, H. Bagdasaryan, N. Baillie, J.P. Ball, N.A. Baltzell, S. Barrow, V. Batourine, M. Battaglieri, K. Beard, I. Bedlinskiy, M. Bektasoglu, M. Bellis, N. Benmouna, A.S. Biselli, B.E. Bonner, S. Bouchigny, S. Boiarinov, R. Bradford, D. Branford, W.K. Brooks, S. Bltmann, V.D. Burkert, C. Butuceanu, J.R. Calarco, S.L. Careccia, D.S. Carman, B. Carnahan, A. Cazes, S. Chen, P.L. Cole, P. Collins, P. Coltharp, D. Cordes, P. Corvisiero, D. Crabb, H. Crannell, V. Crede, J.P. Cummings, R. De Masi, R. DeVita, E. De Sanctis, P.V. Degtyarenko, H. Denizli, L. Dennis, A. Deur, C. Djalali, G.E. Dodge, J. Donnelly, D. Doughty, P. Dragovitsch, M. Dugger, S. Dytman, O.P. Dzyubak, H. Egiyan, K.S. Egiyan, L. Elouadrhiri, P. Eugenio, R. Fatemi, G. Fedotov, R.J. Feuerbach, T.A. Forest, H. Funsten, M. Garon, G. Gavalian, G.P. Gilfoyle, K.L. Giovanetti, F.X. Girod, J.T. Goetz, E. Golovatch, A. Gonenc, R.W. Gothe, K.A. Griffioen, M. Guidal, M. Guillo, N. Guler, L. Guo, V. Gyurjyan, C. Hadjidakis, K. Hafidi, R.S. Hakobyan, J. Hardie, D. Heddle, F.W. Hersman, K. Hicks, I. Hleiqawi, M. Holtrop, M. Huertas, C.E. Hyde-Wright, Y. Ilieva, D.G. Ireland, B.S. Ishkhanov, E.L. Isupov, M.M. Ito, D. Jenkins, H.S. Jo, K. Joo, H.G. Juengst, C. Keith, J.D. Kellie, M. Khandaker, K.Y. Kim, K. Kim, W. Kim, A. Klein, F.J. Klein, M. Klusman, M. Kossov, L.H. Kramer, V. Kubarovskiy, J. Kuhn, S.V. Kuleshov, J. Lachniet, J.M. Laget, J. Langheinrich, D. Lawrence, Ji Li, A.C.S. Lima, K. Livingston, H. Lu, K. Lukashin, M. MacCormick, J.J. Manak, N. Markov, S. McAleer, B. McKinnon, J.W.C. McNabb, B.A. Mecking, M.D. Mestayer, C.A. Meyer, T. Mibe, K. Mikhailov, R. Minehart, M. Mirazita, R. Miskimen, V. Mokeev, L. Morand, S.A. Morrow, M. Moteabbed, J. Mueller, G.S. Mutchler, P. Nadel-Turonski, J. Napoli-

- 2063 tano, R. Nasseripour, S. Niccolai, G. Niculescu, I. Niculescu, B.B. Niczy-
 2064 poruk, M.R. Niroula, R.A. Niyazov, M. Nozar, G.V. O’Rielly, M. Os-
 2065 ipenko, A.I. Ostrovidov, K. Park, E. Pasyuk, C. Paterson, S.A. Philips,
 2066 J. Pierce, N. Pivnyuk, D. Poceanic, O. Pogorelko, E. Polli, S. Pozd-
 2067 niakov, B.M. Preedom, J.W. Price, D. Protopopescu, L.M. Qin, B.A.
 2068 Raue, G. Riccardi, G. Ricco, M. Ripani, B.G. Ritchie, F. Ronchetti,
 2069 G. Rosner, P. Rossi, D. Rowntree, P.D. Rubin, F. Sabati, C. Salgado,
 2070 J.P. Santoro, V. Sapunenko, R.A. Schumacher, V.S. Serov, Y.G. Shara-
 2071 bian, J. Shaw, N.V. Shvedunov, A.V. Skabelin, E.S. Smith, L.C. Smith,
 2072 D.I. Sober, A. Stavinsky, S.S. Stepanyan, S. Stepanyan, B.E. Stokes,
 2073 P. Stoler, I.I. Strakovsky, S. Strauch, R. Suleiman, M. Taiuti, S. Taylor,
 2074 D.J. Tedeschi, U. Thoma, R. Thompson, A. Tkabladze, S. Tkachenko,
 2075 L. Todor, C. Tur, M. Ungaro, M.F. Vineyard, A.V. Vlassov, L.B. We-
 2076 instein, D.P. Weygand, M. Williams, E. Wolin, M.H. Wood, A. Yeg-
 2077 neswaran, J. Yun, L. Zana, J. Zhang, B. Zhao, and Z. Zhao. Mea-
 2078 surement of the x- and -dependence of the asymmetry on the nucleon.
 2079 *Physics Letters B*, 641(1):11 – 17, 2006.
- 2080 [2] J. Ashman and other. A measurement of the spin asymmetry and de-
 2081 termination of the structure function g_1 in deep inelastic muon-proton
 2082 scattering. *Physics Letters B*, 206(2):364 – 370, 1988.
- 2083 [3] D.J. Gross and F. Wilczek. Ultraviolet behavior of non-abelian gauge
 2084 theories. *Phys. Rev. Lett.*, 30(26):1343–1346, 1973.
- 2085 [4] Kenneth G. Wilson. Confinement of quarks. *Phys. Rev. D*, 10:2445–
 2086 2459, Oct 1974.
- 2087 [5] J. P. Chen and others. The GDH Sum Rule and the Spin Structure of
 2088 ^3He and the Neutron using Nearly-Real Photons. JLab Hall A Proposal,
 2089 1997. PR97-110.
- 2090 [6] S. B. Gerasimov. *Yad. Fiz.*; 2:598, 1966.
- 2091 [7] S. D. Drell and A. C. Hearn. Exact sum rule for nucleon magnetic
 2092 moments. *Phys. Rev. Lett.*, 16:908–911, May 1966.
- 2093 [8] S.E. Kuhn, J.-P. Chen, and E. Leader. Spin Structure of the Nucleon -
 2094 Status and Recent Results. *Prog.Part.Nucl.Phys.*, 63:1–50, 2009.

- 2095 [9] H. Dutz et al. First measurement of the gerasimov-drell-hearn sum rule
 2096 for ${}^1\text{H}$ from 0.7 to 1.8 gev at elsa. *Phys. Rev. Lett.*, 91:192001, Nov 2003.
- 2097 [10] H. Dutz et al. Measurement of helicity-dependent photoabsorption
 2098 cross sections on the neutron from 815 to 1825 mev. *Phys. Rev. Lett.*,
 2099 94:162001, Apr 2005.
- 2100 [11] Dieter Drechsel and Lothar Tiator. The Gerasimov-Drell-Hearn sum rule
 2101 and the spin structure of the nucleon. *Ann.Rev.Nucl.Part.Sci.*, 54:69–
 2102 114, 2004.
- 2103 [12] S. Hoblit et al. Measurements of $hd(\gamma, \pi)$ and implications for the convergence
 2104 of the gerasimov-drell-hern integral. *Phys. Rev. Lett.*, 102:172002,
 2105 Apr 2009.
- 2106 [13] M. Anselmino, B.L. Ioffe, and E. Leader. On Possible Resolutions of the
 2107 Spin Crisis in the Parton Model. *Sov.J.Nucl.Phys.*, 49:136, 1989.
- 2108 [14] A. Deur et al. Measurement of the Gerasimov-Drell-Hearn Integral at
 2109 low Q^2 on the Neutron and Deuteron. CLAS Proposal, December 2006.
 2110 PR06-017.
- 2111 [15] Matthias Burkardt. The $g(2)$ Structure Function. *AIP Conf. Proc.*,
 2112 1155:26–34, 2009.
- 2113 [16] M. Anghinolfi and others. The GDH Sum Rule with Nearly-Real Photons
 2114 and the Proton g_1 Structure Function at Low Momentum Transfer.
 2115 CLAS Proposal, 2003. PR03-006.
- 2116 [17] D. Drechsel, B. Pasquini, and M. Vanderhaeghen. Dispersion relations
 2117 in real and virtual Compton scattering. *Phys. Rept.*, 378:99–205, 2003.
- 2118 [18] N. Guler, R. G. Fersch, S. E. Kuhn, P. Bosted, K. A. Griffioen, C. Keith,
 2119 R. Minehart, Y. Prok, K. P. Adhikari, D. Adikaram, M. J. Amaryan,
 2120 M. D. Anderson, S. Anefalos Pereira, H. Avakian, J. Ball, M. Battaglieri,
 2121 V. Batourine, I. Bedlinskiy, A. Biselli, W. J. Briscoe, W. K. Brooks,
 2122 S. Bültmann, V. D. Burkert, D. S. Carman, A. Celentano, S. Chandavar,
 2123 G. Charles, L. Colaneri, P. L. Cole, M. Contalbrigo, D. Crabb,
 2124 V. Crede, A. D’Angelo, N. Dashyan, A. Deur, C. Djalali, G. E. Dodge,
 2125 R. Dupre, A. El Alaoui, L. El Fassi, L. Elouadrhiri, P. Eugenio, G. Fedotov,
 2126 S. Fegan, A. Filippi, J. A. Fleming, T. A. Forest, B. Garillon,

- 2127 M. Garcon, N. Gevorgyan, G. P. Gilfoyle, K. L. Giovanetti, F. X. Girod,
 2128 J. T. Goetz, E. Golovatch, R. W. Gothe, M. Guidal, L. Guo, K. Hafidi,
 2129 H. Hakobyan, N. Harrison, M. Hattawy, K. Hicks, D. Ho, M. Holtrop,
 2130 S. M. Hughes, C. E. Hyde, D. G. Ireland, B. S. Ishkhanov, E. L. Isupov,
 2131 H. S. Jo, K. Joo, S. Joosten, D. Keller, M. Khandaker, A. Kim, W. Kim,
 2132 A. Klein, F. J. Klein, V. Kubarovskiy, S. V. Kuleshov, K. Livingston,
 2133 H. Y. Lu, M. Mayer, I. J. D. MacGregor, B. McKinnon, M. Mirazita,
 2134 V. Mokeev, R. A. Montgomery, A. Movsisyan, C. Munoz Camacho,
 2135 P. Nadel-Turonski, L. A. Net, I. Niculescu, M. Osipenko, A. I. Ostrovit
 2136 ov, K. Park, E. Pasyuk, S. Pisano, O. Pogorelko, J. W. Price, S. Pro
 2137 cureur, M. Ripani, A. Rizzo, G. Rosner, P. Rossi, P. Roy, F. Sabatié,
 2138 C. Salgado, D. Schott, R. A. Schumacher, E. Seder, A. Simonyan, Iu.
 2139 Skorodumina, D. Sokhan, N. Sparveris, I. I. Strakovsky, S. Strauch,
 2140 V. Sytnik, Ye Tian, S. Tkachenko, M. Ungaro, E. Voutier, N. K. Walford,
 2141 X. Wei, L. B. Weinstein, M. H. Wood, N. Zachariou, L. Zana, J. Zhang,
 2142 Z. W. Zhao, and I. Zonta. Precise determination of the deuteron spin
 2143 structure at low to moderate Q^2 with clas and extraction of the neutron
 2144 contribution. *Phys. Rev. C*, 92:055201, Nov 2015.
- 2145 [19] The eg4 wiki. https://clasweb.jlab.org/rungroups/eg4/wiki/index.php/Main_Page. [Online; accessed 22-Sep-2013].
 2146
- 2147 [20] N. Guler. *Spin Structure of the Deuteron*. PhD thesis, Old Dominion
 2148 University, December 2009.
- 2149 [21] M. Osipenko, A. Vlassov and M. Taiuti. A vxibus based trigger for the
 2150 clas detector at cebaf. Technical Report CLAS NOTE 2004-020, JLAB,
 2151 2004.
- 2152 [22] X. Zheng. CLAS EG4 Analysis Note - 'Double- and Target Spin Asym
 2153 metries in Pion Electro-production from Polarized NH₃ Targets'. 2015.
- 2154 [23] K.S. Egiyan. Determination of electron energy cut due to the clas ec
 2155 threshold. Technical Report CLAS-NOTE-1999-007, JLAB, 1999.
- 2156 [24] The eg4 collaboration. <http://clasweb.jlab.org/shift/eg4/>. [On
 2157 line; accessed 22-Sep-2013].
- 2158 [25] S. E. Kuhn. Private communications, 2013.
- 2159 [26] P. Bosted. Private communications, 2010.

- 2160 [27] Beam energies during the eg4 run. http://www.jlab.org/deurpam/e03006/eg4_energy.pdf. [Online; accessed 05-Jan-2017].
- 2161
- 2162 [28] P. Bosted. CLAS EG1-DVCS Technical Note 004 - 'Tracking from Drift
2163 Chambers to Target through Solenoid'. 2010.
- 2164 [29] P. Bosted and A. Kim. CLAS EG1-DVCS Technical Note 002 - 'Beam
2165 (x,y) and Target Center z from Raster ADCs'. 2014.
- 2166 [30] A. Klimenko and S. Kuhn . Momentum Corrections for E6. Technical
2167 Report CLAS-Note 2003-005, JLAB, 2003.
- 2168 [31] William R Leo. *Techniques for nuclear and particle physics experiments: a how-to approach*. Springer, 1994.
- 2169
- 2170 [32] R. G. Fersch. PhD thesis, January.
- 2171 [33] P. Bosted. Pair-symmetric and pion backgrounds for eg1b. Technical
2172 Report CLAS-NOTE-2004-005, JLAB, 2004.
- 2173 [34] S. P. Phillips. http://clasweb.jlab.org/rungroups/eg4/wiki/index.php/October_14%2C_2011. [Online; accessed 22-Sep-2013].
- 2174
- 2175 [35] Peter Bosted. Nh3 correction for nd3 target: Eg1-dvcs technical note
2176 17. Technical report, November 2011.
- 2177 [36] Suman Koirala. EG1-DVCS Part-C Target Contamination. Technical
2178 report, May 2012.
- 2179 [37] S.E. Kuhn and K. Adhikari. Data Analysis for EG4 - extraction of g_1
2180 from data. 2013.
- 2181 [38] K. Abe et al. Measurements of the proton and deuteron spin structure
2182 functions g_1 and g_2 . *Phys. Rev. D*, 58:112003, Oct 1998.
- 2183 [39] T.V. Kuchto and N.M. Shumeiko. Radiative effects in deep inelastic
2184 scattering of polarized leptons by polarized nucleons. *Nuclear Physics B*,
2185 219(2):412–436, 1983.
- 2186 [40] L. W. Mo and Y. S. Tsai. Radiative corrections to elastic and inelastic
2187 ep and up scattering. *Rev. Mod. Phys.*, 41:205–235, Jan 1969.

- 2188 [41] P.E. Bosted and M.E. Christy. Empirical fit to inelastic electron-
 2189 deuteron and electron-neutron resonance region transverse cross-
 2190 sections. *Phys. Rev.*, C77:065206, 2008.
- 2191 [42] R. G. Fersch et al. Precise Determination of Proton Spin Structure
 2192 Functions at Low to Moderate Q^2 with CLAS. To be published, October
 2193 2012.
- 2194 [43] N. Guler et al. Precise Determination of Deuteron and Neutron Spin
 2195 Structure Functions at Low to Moderate Q^2 with CLAS. To be pub-
 2196 lished, October 2013.
- 2197 [44] Yonatan Kahn, W. Melnitchouk, and Sergey A. Kulagin. New method
 2198 for extracting neutron structure functions from nuclear data. *Phys. Rev.*,
 2199 C79:035205, 2009.
- 2200 [45] M. Holtrop. GSIM: CLAS GEANT Simulation. http://nuclear.unh.edu/~maurik/gsim_info.shtml. [Online; accessed 22-Sep-2013].
- 2201 [46] Brooks, W. *CLAS - A large acceptance spectrometer for intermediate*
 2202 *energy electromagnetic nuclear physics*. Jun 1999.
- 2203 [47] B. Dey. *Differential cross section and polarization extractions for $\gamma p \rightarrow$*
 2204 *$K^+ \Sigma^0$ and $\gamma p \rightarrow \phi p$ using CLAS at Jefferson Lab, towards a partial wave*
 2205 *analysis in search of missing baryon resonances*. PhD thesis, Carnegie
 2206 Mellon University, July 2011.
- 2207 [48] J. Zhang. *Exclusive π^- Electro-production from the Neutron in the Res-*
 2208 *onance Region*. PhD thesis, Old Dominion University, May 2010.
- 2209 [49] Veronique Bernard, Evgeny Epelbaum, Hermann Krebs, and Ulf-G.
 2210 Meissner. New insights into the spin structure of the nucleon. *Phys.*
 2211 *Rev.*, D87:054032, 2013.

₂₂₁₃ **Appendix A**

₂₂₁₄ **FFREAD cards used by GSIM**

Table A.1: Some of the ffreac cards & their values which are used as GSIM input parameters.

Cards	Values
MAGTYPE	2
MAGSCALE	-0.5829 0.0 (for 1.337 GeV)
MAGSCALE	-0.3886 0.0 (for 1.993 GeV)
GEOM	'ALL'
NOMC	'EC' 'SC' 'CC' 'DC'
NOGEOM	'MINI' 'ST' 'TG2' 'TG' 'SOL'
NOGEOM	'PTG' 'FOIL'
NOMATE	'PTG' 'FOIL'
PTGIFIELD	1
TMGIFIELD	1
TMGIFIELDM	1
TMGFIELDM	51.0
TMGSCALE	0.979
PTGMAXRAD	300.0
MGPOS	0.0 0.0 -100.93
BAFF	3. 9. 165.3 9. 180.5 9. 195.8
RUNG	50556
AUTO	1
KINE	1